

Electronic Thesis and Dissertation Repository

9-20-2019 2:00 PM

A Heterogeneous Patient-Specific Biomechanical Model of the Lung for Tumor Motion Compensation and Effective Lung Radiation Therapy Planning

Parya Jafari
The University of Western Ontario

Supervisor
Samani, Abbas
The University of Western Ontario Joint Supervisor
Sadeghi-Naini, Ali
York University

Graduate Program in Biomedical Engineering

A thesis submitted in partial fulfillment of the requirements for the degree in Master of Science

© Parya Jafari 2019

Follow this and additional works at: <https://ir.lib.uwo.ca/etd>



Part of the [Biomechanical Engineering Commons](#), [Biomedical Commons](#), and the [Biomedical Engineering and Bioengineering Commons](#)

Recommended Citation

Jafari, Parya, "A Heterogeneous Patient-Specific Biomechanical Model of the Lung for Tumor Motion Compensation and Effective Lung Radiation Therapy Planning" (2019). *Electronic Thesis and Dissertation Repository*. 6636.

<https://ir.lib.uwo.ca/etd/6636>

This Dissertation/Thesis is brought to you for free and open access by Scholarship@Western. It has been accepted for inclusion in Electronic Thesis and Dissertation Repository by an authorized administrator of Scholarship@Western. For more information, please contact wlsadmin@uwo.ca.

Abstract

Radiation therapy is a main component of treatment for many lung cancer patients. However, the respiratory motion can cause inaccuracies in radiation delivery that can lead to treatment complications. In addition, the radiation-induced damage to healthy tissue limits the effectiveness of radiation treatment. Motion management methods have been developed to increase the accuracy of radiation delivery, and functional avoidance treatment planning has emerged to help reduce the chances of radiation-induced toxicity. In this work, we have developed biomechanical model-based techniques for tumor motion estimation, as well as lung functional imaging. The proposed biomechanical model accurately estimates lung and tumor motion/deformation by mimicking the physiology of respiration, while accounting for heterogeneous changes in the lung mechanics caused by COPD, a common lung cancer comorbidity. A biomechanics-based image registration algorithm is developed and is combined with an air segmentation algorithm to develop a 4DCT-based ventilation imaging technique, with potential applications in functional avoidance therapies.

Keywords

Four dimensional computed tomography (4DCT), Lung Cancer, Radiation Therapy, Biomechanical Modeling, Finite Element Modeling, Chronic Obstructive Pulmonary Disease, Functional Avoidance Planning, Ventilation Imaging, and Deformable Image Registration

Summary for Lay Audience

Lung cancer is the leading cause of cancer-related death in Canada. Radiation therapy is a main component of treatment for many lung cancer patients, in which high-energy beams are planned to target the tumor cells and destroy them.

Both the lung and the tumor can move and deform during the radiation therapy as the patient breathes. If not accounted for, the motion of the tumor can considerably reduce the effectiveness of treatment. An ideal solution is to develop a system that can track the tumor in real-time and guide the radiation delivery accordingly. This tracking system requires accurate estimation of the tumor's location and shape. Currently, four-dimensional computed tomography (4DCT) scans of the patients are used to plan the radiation delivery. We have developed a technique for estimating tumor motion/deformation by modeling the breathing mechanics using 4DCT scans. Our biomechanical model mimics lung physiology and is driven by the pressure and diaphragm motion present during a breathing cycle. Chronic obstructive pulmonary disease (COPD), is a progressive lung disease that commonly coexists with lung cancer and affects the lung mechanics in a heterogeneous manner. By incorporating these heterogeneous changes in the lung mechanics into our model, we achieved high accuracies for tumor motion/deformation estimation.

Radiation treatment planning aims at maximizing the tumor dose while minimizing the healthy lung tissue exposure to radiation. Considering the heterogeneity in the lung function present in cancer patients (due to COPD and/or smoking), the outcome of radiation therapy can be improved by planning the radiation beam to deliberately avoid the well-functioning regions in the lung and instead pass through the already poorly-functioning regions. This method of planning is called functional avoidance and requires regional information on lung function that is usually obtained using magnetic resonance (MR) or nuclear medicine imaging. We have developed a 4DCT-based technique for imaging the regional ventilation, as a surrogate for lung function. 4DCT is a cost effective and accessible alternative to the current modalities. Our ventilation imaging method utilizes our accurate lung biomechanical model to find the regional change in the air volume, i.e. ventilation. Results show good agreement with MR-based functional images.

Co-Authorship Statement

This thesis contains materials from two manuscripts that are currently under review.

Chapter 2 presents our manuscript entitled: “A Patient-Specific Heterogeneous Biomechanical Model of the Lung for Accurate Tumor Motion Estimation”, by Parya Jafari, Brian P. Yaremko, Grace Parraga, Douglas A. Hoover, Ali Sadeghi-Naini, and Abbas Samani. Brian Yaremko and Douglas Hoover provided manual segmentations used to validate semi-automatic segmentation algorithms developed and used in this study. Brian Yaremko, Grace Parraga and Douglas Hoover provided the raw data used in this study. Ali Sadeghi-Naini and Abbas Samani provided advice on the study design, interpretation of the results, and presentation of data. I helped design the experiments. I developed the lung biomechanical model, wrote the codes to generate results, interpreted the results, and wrote the manuscript under the supervision of Drs. Ali Sadeghi-Naini and Abbas Samani.

Chapter 3 presents our manuscript entitled: “4DCT Ventilation Imaging Using Biomechanical Model-based Deformable Registration”, by Parya Jafari, Douglas A. Hoover, Brian P Yaremko, Grace Parraga, Abbas Samani, and Ali Sadeghi-Naini. Douglas Hoover and Brian Yaremko provided manual segmentations used to validate semi-automatic segmentations employed in this study. Douglas Hoover, Brian Yaremko, and Grace Parraga provided the raw data used in this study. Ali Sadeghi-Naini and Abbas Samani provided advice on the study design, interpretation of the results, and presentation of data. I helped with the study design. I developed the biomechanical model-based registration algorithm and the 4DCT-based ventilation imaging technique, wrote the codes to generate results, interpreted the results, and wrote the manuscript under the supervision of Drs. Ali Sadeghi-Naini and Abbas Samani.

Acknowledgments

First and foremost, I want to seize this opportunity to thank my supervisors, Dr. Ali Sadeghi-Naini and Dr. Abbas Samani that provided me with support and guidance throughout my graduate studies. I am grateful for their dedication to helping me grow as a researcher and as a person. Working with Dr. Sadeghi and Dr. Samani, I learned how to set forth research goals, to be persistent, and to stay creative. During every meeting when we brainstormed ideas to tackle a new problem that I or any of our lab members had, Dr. Samani and Dr. Sadeghi nurtured our problem solving and communication skills. Dr. Sadeghi's bright and detail-oriented comments helped me take this project to the next level. He always encouraged me to do and want more and helped me to always stay on track. I am extremely grateful to have had the opportunity to work with Dr. Samani. He always believed in me and supported me through all the challenges I faced during this project with kindness and understanding. With his profound knowledge in the field, he patiently helped me with any questions I had. With his creativity in problem solving, Dr. Samani helped unleash my creative energy, making my Master's studies a joyful experience.

I would also like to thank the members of my advisory committee, Drs. Hanif Ladak and Douglas Hoover. They provided me with valuable insights into the project and helped me gain a more comprehensive knowledge in the area. I would like to thank my lab mates for their contribution to making our office a productive and at the same time lighthearted environment. I am greatly appreciative for all the time they spent to help me refine my presentation skills. A special thanks goes to Sergio Dempsey, for being open to a conversation whether it involved brainstorming, helping others with new insights, or simply arguing which one of us has the better solution.

Most importantly, I want to express my deepest gratitude to my kind and loving family. They have been a continuous source of inspiration and unconditional support since I can remember. Especially my parents, who always find ways to challenge me, encouraging me to work harder and become a better person. Mom and Dad, I am amazed by how you can always lift me up with your smiles. I could not have come this far if it wasn't for everything you have done for me.

Table of Contents

Abstract.....	ii
Summary for Lay Audience.....	iii
Co-Authorship Statement.....	iv
Acknowledgments.....	v
Table of Contents.....	vi
List of Tables.....	ix
List of Figures.....	x
List of Abbreviations.....	xiv
Chapter 1.....	1
1 « Introduction».....	1
1.1 « Lung Cancer ».....	1
1.1.1 Statistics.....	1
1.1.2 Comorbidities: Chronic Obstructive Pulmonary Disease.....	3
1.1.3 Lung Cancer and COPD.....	5
1.2 « Lung Cancer Treatment ».....	6
1.2.1 External Beam Radiation Therapy.....	6
1.3 «Motion Management Methods».....	12
1.3.1 Motion Encompassing.....	13
1.3.2 Gated Methods.....	13
1.3.3 Motion Limiting Methods.....	16
1.3.4 Real-time Tracking Methods.....	17
1.3.5 Tumor Tracking Workflow.....	19
1.3.6 Biomechanical model-based tumor motion/deformation estimation.....	20
1.4 «Functional Avoidance Treatment Planning».....	21

1.5 «4DCT Ventilation Imaging Methods»	23
1.6 «Image Segmentation».....	25
1.6.1 Region Growing Algorithm	26
1.7 «Image Registration»	26
1.8 «Theory of Elasticity».....	28
1.8.1 Linear Elasticity	34
1.8.2 Hyperelasticity	35
1.9 «Inverse Problem»	37
1.10«Research Objectives».....	38
1.11«Thesis Outline»	38
1.11.1 Chapter 2: A Patient-Specific Heterogeneous Biomechanical Model of the Lung for Accurate Tumor Motion Estimation	38
1.11.2 Chapter 3: 4DCT Ventilation Imaging Using Biomechanical Model-based Deformable Registration.....	39
1.11.3 Chapter 4: Discussion and Conclusion	40
«References».....	40
Chapter 2.....	52
2 « A Patient-Specific Heterogeneous Biomechanical Model of the Lung for Accurate Tumor Motion Estimation ».....	52
2.1 « Introduction ».....	52
2.2 « Materials and Methods ».....	56
2.2.1 Data Acquisition	56
2.2.2 Patient-specific Biomechanical Model	56
2.2.3 Optimization Framework	62
2.3 « Results ».....	65
2.3.1 Two-step Optimization Algorithm.....	65
2.3.2 Diaphragm FFD Registration Algorithm	65

2.3.3	Tumor motion/deformation estimation and Registration Accuracy	66
2.4	«Discussion»	70
	«References»	72
Chapter 3	79
3	«4DCT Ventilation Imaging Using Biomechanical Model-based Deformable Registration »	79
3.1	« Introduction ».....	79
3.2	« Materials and Methods ».....	82
3.2.1	Data Acquisition	83
3.2.2	Biomechanical Model-based DIR.....	85
3.2.3	Air Segmentation Algorithm.....	89
3.2.4	Correcting for Regional Volume Expansion.....	90
3.2.5	Generating the CTVI.....	91
3.2.6	Comparison of the CTVI with Hyperpolarized Gas MRI.....	91
3.3	« Results ».....	92
3.3.1	Biomechanical Model-based DIR Accuracy	92
3.3.2	CTVI and Qualitative Comparison with ³ He MRI	94
3.3.3	Quantitative Comparison with ³ He MRI.....	96
3.3.4	Discussion and Conclusions	96
	«References»	98
Chapter 4	106
4	« Conclusion and Future Work »	106
4.1	Chapter 2.....	106
4.2	Chapter 3.....	107
	«References»	108
Curriculum Vitae	112

List of Tables

Table 1-1 Summary of lung cancer staging guideline. Reproduced with permission (99). Copyright 2009, OUP Oxford.....	7
Table 1-2 Comparison of some characteristics of 3D-CRT and SBRT. Reproduced with permission (30). Copyright 2010, John Wiley and Sons.	10
Table 1-3 Respiratory-induced motion of the lung tumor and diaphragm in different directions. Reproduced with permission (3). Copyright 2006, John Wiley and Sons.	14
Table 2-1 Evaluation results for the Fourier representation of optimized pressure.....	65
Table 2-2 The extent of COPD phenotypes represented in their percentage volume (%V), and the percentage improvement in measures of tumor motion/deformation estimation for each case.....	67
Table 2-3 Average LRE for all patients before and after registration with homogeneous and heterogeneous models.....	69
Table 3-1 Target registration error between EE and EI scans using ~40 landmarks, before and after FE-based registration.....	93

List of Figures

Figure 1-1. Lung cancer annual incidence, annual deaths, and 5-year survival rate statistics (1).....	2
Figure 1-2. Relative incidence of different lung cancer types (9).	3
Figure 1-3. Emphysema. (a) Schematic comparing the alveoli structure in healthy and emphysematous tissues. The breakdown of the airway walls enlarges the alveoli and decreases the effective surface area for O ₂ and CO ₂ exchange. Reproduced with permission. Copyright 2019, Mayo Foundation for Medical Education and Research. (b) Regions affected by emphysema can be detected on CT scans as low attenuation areas (sample regions enclosed in red ellipses).....	4
Figure 1-4. The classification of airways to large and small airways based on branching and diameter. The acinar zone is where the gas exchange happens, and it starts from terminal bronchioles. Reproduced with permission (15). Copyright 2012, Taylor & Francis.	5
Figure 1-5. Schematic of the 3D conformal radiation therapy. Reproduced with permission (31). Copyright 2008, SNMMI.	9
Figure 1-6. 3D CRT vs. IMRT. (a) in 3D CRT, dose conformality is limited to the open/close aperture configuration, while (b) IMRT, offers higher dose conformality resulting in smaller margins and higher potential for less toxicity to OAR.	11
Figure 1-7. Motion encompassing. PTV includes the entire path of tumor's motion from expiration to inspiration, along with extra safety margins.....	13
Figure 1-8. Gated Radiation therapy. The motion of the tumor is smallest at certain windows of time (gates) during respiration. The radiation is applied only during these gates. Reproduced with permission (49). Copyright 2015, British Journal of Radiology.	15
Figure 1-9. Breath-hold methods. The respiratory motion amplitude decreases during the breath-hold span. The radiation is applied during this span to reduce uncertainties caused by	

tumor motion. Reproduced with permission (49). Copyright 2015, British Journal of Radiology.....	17
Figure 1-10. The biomechanics-based real-time tumor tracking workflow.	20
Figure 1-11. Flow chart of a general registration algorithm. A metric is used to compare the fixed image with the moving image after each time the moving transform is updated. The optimization stops when the metric or changes in the metric are smaller than a predefined limit. The virtual image is reconstructed after the optimization is completed. Adapted from The ITK Software Guide Book 2 Fourth Edition, by Johnson H.J., McCormick M.M., Ibáñez L., and the Insight Software Consortium.	28
Figure 1-13. A particle in the elastic geometry at its initial state (\mathbf{X}), displaced by $\mathbf{u}(\mathbf{X}, \mathbf{t})$ to its final state ($\mathbf{x}(\mathbf{X}, \mathbf{t})$).	30
Figure 1-14. The infinitesimal cube and the unit vectors normal to its surfaces, used for calculating internal traction.....	33
Figure 2-1. Examples of motion-induced artifacts in the dataset. The images show different types of artifacts as classified by Yamamoto et al. (a) Overlapping structure, (b) incomplete structure, and (c) duplicate structure.....	58
Figure 2-2. Axial view of slices from 4DCT data showing emphysema (green), SAD (yellow), and the tumor (red). Healthy lung parenchyma is represented by blue. (a) Patient #1, with extensive SAD, less emphysema. (b) Patient #2, with extensive SAD, less emphysema, very large tumor. (c) Patient #3, the tumor is located further from COPD-affected volumes. (d) Patient #4, very less SAD and no emphysema. (e) Patient #5, with extensive SAD and emphysema, tumor in proximity of affected areas.....	61
Figure 2-3. Flowchart showing the first optimization step. The 4DCT data is used to segment the lung and the tumor at phase EE (ϕ_{50}) and the target phase, for which the maximum pressure amplitude (\mathbf{P}_i) and the diaphragm registration correction factor (\mathbf{K}_{CF_i}) are optimized. The homogeneous finite element model is used in this step to deform the reference geometry to the target counterpart. The cost function \mathbf{f}_c regulates the updating of the parameters to ensure the best registration.	63

Figure 2-4. Difference image between diaphragm at EE (50%) and EI (0%), (a) before registration, (b) after registration using FFD image registration, (c) after registration using the optimized K_{CF} parameter applied to the deformation field. 66

Figure 2-5. Comparing the results of tumor motion/deformation estimation between homogeneous and heterogeneous models. (a) Average Dice similarity coefficient and (b) average Hausdorff distance (HD) between actual and simulated tumors over all target phases. 67

Figure 2-6. Actual tumor CoM motion magnitude and the simulated tumor CoM motion magnitude using homogeneous and heterogeneous models. 69

Figure 3-1. The proposed CTVI workflow. The peak-inspiration CT scans are registered using the biomechanics-based DIR. The air segmentation algorithm finds the partial volume of air in each scan after registration. The regional volume expansion is corrected for before the CTVI is calculated as the difference between air volumes in end-inhale and end-exhale voxels. 83

Figure 3-2. Models geometry. The top row figures (a-1, b-1, and c-1) show the lung finite element meshes for the three patients at the end-exhale phase. The bottom row figures (a-2, b-2, and c-2) show the deformed geometries of the same cases after FE analysis. The mesh elements are color-coded according to the magnitude of displacements in mm. 86

Figure 3-3. Finding initial thresholds for air segmentation. (a) The combined histogram of end-inhale and end-exhale histograms. The two initial thresholds divide the histogram to 3 regions, air only voxels, air combined with tissue voxels, and tissue only voxels. (b) The initial thresholds are found as points where the end-inhale and end-exhale histograms cross. 90

Figure 3-4. An example of the registration. (a) Moving image (EI), (b) target image (EE), (c) Resampled image (deformed EI image, to match EE), (d) difference image before registration, (e) difference image after registration using intensity-based DIR, and (f) the difference image after registration using biomechanical model-based DIR. 93

Figure 3-5. Comparison of the ^3He MR and CTVI, both overlaid on CT. Each row compares 3 coronal slices of one patient, (a) patient #1, (b) patient #2, and (c) patient #3..... 94

Figure 3-6. Comparing the breathing maneuver. Rows (a), (b), and (c) correspond to patients #1, #2, and #3, respectively. The first column shows a slice of the 3DCT, taken at the same inspiration volume as MR, second column shows the corresponding slice on 4DCT, acquired at tidal volume, and the third column is the absolute difference image of the two. 95

Figure 3-7. The Dice similarity coefficient between ^3He MR and CTVI for poorly ventilated and well-ventilated regions for the three patients. 96

List of Abbreviations

3D-CRT	Three-Dimensional Conformal Radiation Therapy
4DCT	4-Dimensional Computed Tomography
AP	Anterior-Posterior
BCs	Boundary Conditions
CBCT	Cone-Beam Computed Tomography
COPD	Chronic Obstructive Pulmonary Disease
CoM	Center of Mass
CT	Computed Tomography
CTV	Clinical Target Volume
CTVI	4DCT-Based Ventilation Imaging
DIR	Deformable Image Registration
EBRT	External Beam Radiation Therapy
EE	End-Exhale
EI	End-Inhale
FE	Finite Element
FFD	Free Form Deformation
FRC	Functional Residual Capacity
GTV	Gross Tumor Volume
Gy	Gray
HD	Hausdorff Distance
HU	Hounsfield Units
IMRT	Intensity Modulated Radiation Therapy
ITV	Internal Target Volume
LR	Left-Right
LRE	Landmarks Registration Error
MRI	Magnetic Resonance Imaging
NMI	Normalized Mutual Information
NSCLC	Non-Small Cell Lung Cancer

NTCP	Normal Tissue Control Probability
OAR	Organ at Risk
PET	Proton Emission Tomography
P_T	Transpulmonary Pressure
PTV	Planning Target Volume
RT	Radiation Therapy
SAD	Small Airways Disease
SBRT	Stereotactic Body Radiation Therapy
SCLC	Small Cell Lung Cancer
SI	Superior-Inferior
SPECT	Single-Proton Emission Computed Tomography
TCP	Tumor Control Probability
TPS	Thin-Plate Spline
VMAT	Volumetric Modulated Arc Therapy

Chapter 1

1 « Introduction »

Lung cancer remains the leading cause of cancer-related deaths among men and women in Canada (1). Effectiveness of radiation therapy, as a main component of lung cancer treatment in many patients, may be reduced by uncertainties caused by respiratory motion and damage to healthy tissues. Respiratory motion compensation methods have emerged as potential solution for the former (2,3), and functional avoidance techniques have been developed to alleviate the latter (4,5). In this thesis, we describe biomechanical model-based techniques for motion estimation and functional imaging to help improving the effectiveness of radiation therapy.

1.1 « Lung Cancer »

1.1.1 Statistics

Cancer is the leading cause of death in Canada, with approximately 1 in 2 men and 1 in 2.2 women expected to develop cancer in their lifetime (1). Lung and bronchus (referred to as lung for brevity), colorectal, breast, and prostate cancers are the most commonly diagnosed cancer types in Canada. They are responsible for about 50% of all cancer deaths in 2017 (Figure 1-1) (6). As shown in Figure 1-1, with incidence rates higher than all other cancer types, lung cancer kills more people than colorectal, breast, and prostate cancers combined (1). The World Health Organization estimates that lung cancer is the cause of 1.59 million deaths globally per year, with 71% of them caused by smoking (7). The 5-year survival rate of lung cancer is only 19% (Figure 1-1).

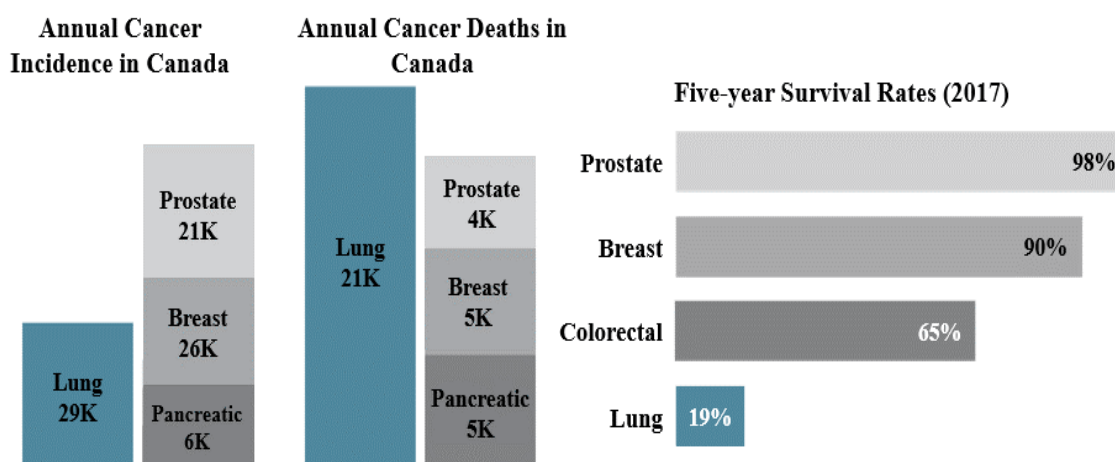


Figure 1-1. Lung cancer annual incidence, annual deaths, and 5-year survival rate statistics (1).

This rate is dependent on the type of the lung cancer (small cell lung cancer (SCLC) or non-small cell lung cancer (NSCLC)) and the stage at which it is detected (1). For example, estimates of five-year survival rates range from 1% to 10% across the substages of stage IV, and from 68% to 92% for the substages of stage I. Five-year survival estimates are lower for SCLC: 2% for stage IV and 31% for stage I (1). NSCLC accounts for more than 80% of lung cancer cases and has three major histologic subtypes that are categorized by the cell type from which the disease originates (8). 1) Adenocarcinoma starts in glandular cells, is usually located along the outer edges of the lung and is more common among women and non-smokers. 2) Squamous cell (or epidermoid) carcinoma starts from squamous cells, usually occurs in one of the main airways or in the central part of the lung and is strongly associated with smoking. 3) Large cell lung cancer is distinguished from SCLC by the large cancer cells size, and is often found in the periphery, and are more commonly diagnosed in men (8). Figure 1-2 shows the incidence of different lung cancer types (8,9).

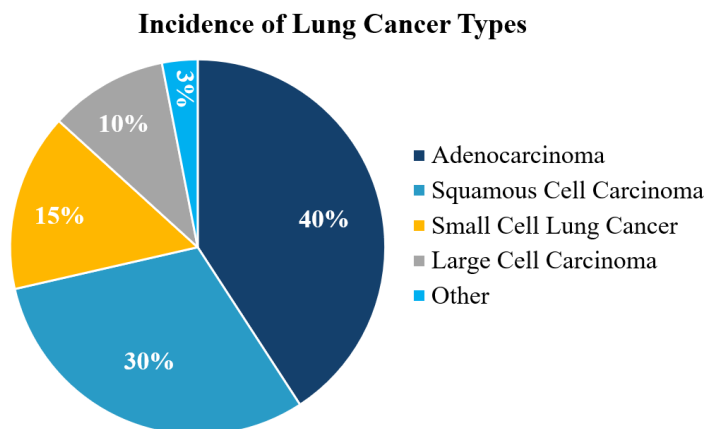


Figure 1-2. Relative incidence of different lung cancer types (9).

1.1.2 Comorbidities: Chronic Obstructive Pulmonary Disease

Chronic obstructive pulmonary disease (COPD), is a progressive lung disease that fatally deteriorates the lung function over time. COPD is the 4th most common cause of hospitalization among men and the 6th most common cause of hospitalization among women in Canada. COPD is the only chronic disease with increasing mortality and is estimated that it will be the 3rd leading cause of death worldwide by 2020 (10,11).

The damage to the lungs in COPD is caused by exogenous (caused by smoking) or endogenous oxidative stress, protease activity, autoantibody expression, and inflammatory cytokine release. These will cause several pulmonary manifestations, including alveoli wall damage (emphysema) and small airways disease (SAD), which will in turn cause air trapping and lung hyperinflation (12).

Emphysema is pathologically described as permanent destruction of the alveoli walls, resulting in abnormal permanent enlargement of the air spaces distal to the terminal bronchioles (Figure 1-3). The destruction of the alveoli walls results in a decrease in the surface area available for exchange of O₂ and CO₂ to and from the capillaries (Figure 1-3) (12). As shown in Figure 1-3 emphysema can be detected on computed tomography (CT) scans taken at full inspiration. The extent of emphysema can also be quantified using information derived from CT scan (13).

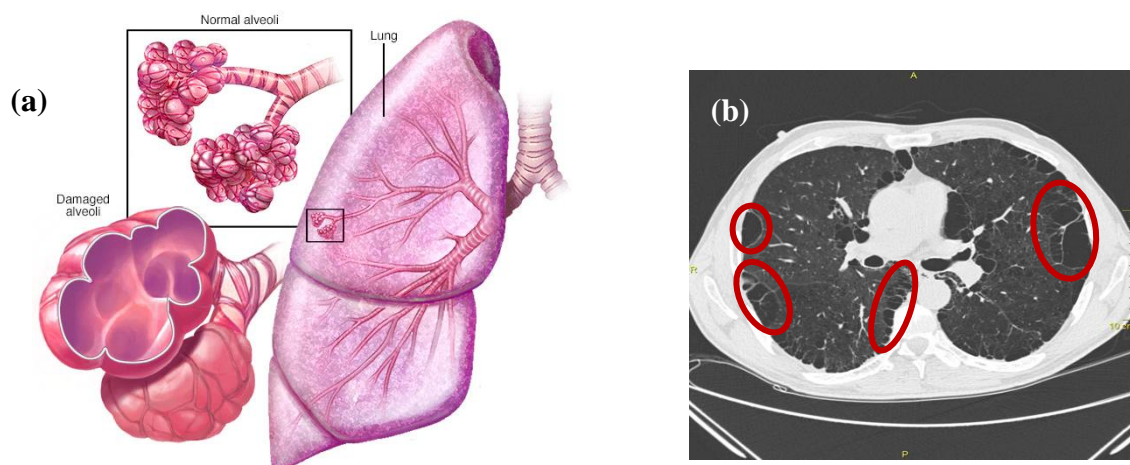


Figure 1-3. Emphysema. **(a)** Schematic comparing the alveoli structure in healthy and emphysematous tissues. The breakdown of the airway walls enlarges the alveoli and decreases the effective surface area for O_2 and CO_2 exchange. Reproduced with permission. Copyright 2019, Mayo Foundation for Medical Education and Research. **(b)** Regions affected by emphysema can be detected on CT scans as low attenuation areas (sample regions enclosed in red ellipses).

The patterns of emphysema observed in COPD are classified to centrilobular (airways destruction observed around the terminal bronchioles) and panlobular or panacinar (homogeneous airways destruction) (12,14).

The airways with internal diameter smaller than 2 mm that extend from the 8th generation airways to the alveoli are classified as “small airways” (Figure 1-4). The cross-sectional surface area of the small airways is far greater than that of the large airways; however, they are responsible for only about 10% of the total airways’ resistance. Therefore, conventional pulmonary function tests may fail to detect abnormalities even when extensive disease is present in the small airways. In COPD, SAD mostly involves remodeling of the small airways, along with an increase in airways smooth muscle, destruction of alveolar attachments, and airway wall fibrosis (12,15). Assessment of SAD is challenging. A number of invasive and non-invasive methods have been reported for diagnosis and assessment of SAD. The invasive methods are based on histological analysis on transbronchial biopsy samples or surgically resected specimens(16).

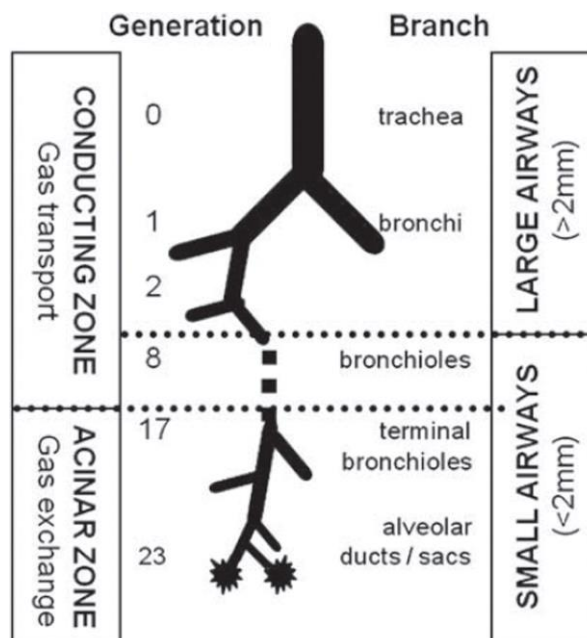


Figure 1-4. The classification of airways to large and small airways based on branching and diameter. The acinar zone is where the gas exchange happens, and it starts from terminal bronchioles. Reproduced with permission (15). Copyright 2012, Taylor & Francis.

The non-invasive methods are based on imaging or physiological assessments (15). Imaging is an attractive option for assessment of SAD, and COPD in general, especially in the case of lung cancer patients where imaging of the lungs is part of the routine care in most centers. Standard CT, high resolution CT, and hyperpolarized gas magnetic resonance imaging (MRI) are widely used for diagnosis, and assessment of disease progression and treatment response (16). Single-proton emission computed tomography (SPECT) and proton emission tomography (PET) can also be used for characterization of COPD, as they provide more insight into ventilation-perfusion relationships in the peripheral lung regions (17,18).

1.1.3 Lung Cancer and COPD

More than 65% of lung cancer patients also suffer from COPD (11,19). Beside the fact that smoking has proven to be a cause for both COPD and lung cancer, there is increasing evidence that links these two diseases beyond the one common etiology. Lung cancer is

up to 5 times more likely to affect smokers with COPD than smokers with normal lung function (20). A 2- to 6-fold higher risk of lung cancer in COPD patients have been reported to be regardless of smoking habits (21,22). Common mechanisms in COPD and lung cancer, such as premature aging in the lungs, common pathogenic factors, or genetic predispositions to either disease was explored as possible explanations for the high coexistence of lung cancer and COPD (21). COPD is known as an independent risk factor for lung cancer, respiratory-related complications, and postoperative recurrence of NSCLC (19). A number of previous studies have reported that coexisting COPD leads to poor prognosis for lung cancer (11,19).

1.2 « Lung Cancer Treatment »

The treatment strategy for lung cancer depends on factors such as the subtype and stage of the malignancy, histology, patient's age, comorbidities, and patient's preference. Comprehensive guidelines for diagnosis, staging, risk assessment, and treatment have been developed and are used in clinical practice for optimal outcome (23,24). Stage grouping of the malignant tumors according to the TNM guide is based on the extent of the primary tumor (denoted by T), regional lymph node metastasis (N), and distant metastasis (M) (Table 1-1). Treatment can be either or a combination of surgery, immunotherapy, chemotherapy, targeted therapy, and radiation therapy. Some treatment strategies are preferred over the others for different stages. A summary of recommended treatment strategies based on stage grouping and guidelines for diagnosis and pathology can be found in (23,24).

1.2.1 External Beam Radiation Therapy

External beam radiation therapy (EBRT) with curative intent is a main component in the current standard of care as primary or adjuvant treatment for early stage NSCLC and unresectable locally advanced NSCLC (23,25). In addition, radiation therapy is used for palliative purposes for alleviating bronchial obstruction or to relieve symptoms such as pain, cough, or bleeding (8,23,26).

In EBRT, high-energy particles or waves such as x-rays, protons, gamma rays, or electron beams are planned to target the tumor cells and damage their DNA. Radiation-induced damage to the DNA kills malignant cells or impairs their proliferation (8).

Table 1-1 Summary of lung cancer staging guideline. Adapted from (99).

Stage	TNM	5-year survival
IA	$T_1N_0M_0$	75%
IB	$T_2N_0M_0$	55%
IIA	$T_1N_1M_0$	40%
IIB	$T_2N_1M_0$ or $T_3N_0M_0$	40%
IIIA	$T_{1-2}N_2M_0$ or $T_3N_{1-2}M_0$	10-35%
IIIB	$T_4N_xM_0$ or $T_xN_3M_0$	5%
IV	$T_xN_xM_1$	<5%

*Where x denotes any possible staging value

T denotes tumor size

Tumors less than 3 cm in greatest dimension, surrounded by lung and without invasion into main bronchus

Tumor without any of: more than 3 cm in any dimension; invasion into main bronchus, more than 2 cm from carina; or obstructive pneumonitis, but not involving the entire lung

Tumor with any of: invasion into chest wall, diaphragm, mediastinal pleura or parietal pericardium; invasion into the main bronchus within 2 cm of carina, but not invading it; or obstructive pneumonitis of the entire lung

Tumor with any of: invasion into mediastinum, heart, large vessels, trachea, esophagus, vertebra, or carina; separate tumor nodules in the same lobe; or malignant pleural effusion

N denotes extent of regional Lymph Node spread

No spread

1-3. Increasing spread to nodes

M denotes distant Metastases

1. No metastatic disease
2. Distant metastases found (including pleural or pericardial effusion)

The amount of energy per unit mass that is deposited (or planned to be delivered) is measured as “dose” of radiation in Gray (Gy) (27). Radiation therapy generally ranges from static beams to multiple rotating beams all exploiting the concept of superposition to deposit the prescribed doses in the tumor volume while sparing surrounding normal tissue within the human body. The primary goal of radiotherapy is to maximize tumor control probability (TCP) while minimizing normal tissue complication probability (NTCP) (28). Therefore, the mitigation of high dose to organs at risk (OARs) and healthy tissue is crucial to the success of radiotherapy and avoiding negative radiation-related side effects. A treatment planning system is used for radiotherapy treatment planning, optimization and 3-dimensional dose calculation (29). For radiotherapy planning, a total prescribed dose is typically broken down into multiple treatment sessions or treatment fractions. Modern radiotherapy employs the use of 4-dimensional computed tomography (4DCT) imaging of the patient's body to target the tumor volume and guide the high-energy radiation beams (29). Within the CT dataset, a physician segments the gross tumor volume (GTV), based on his or her own clinical experiences, as well as clinical guidelines on disease specific characteristics such as pattern specific progression and staging. Two additional margins are added on top of the GTV to account for different types of uncertainty in radiation delivery. The first supplementary margin is added to create the clinical target volume (CTV), which accounts for uncertainty related to microscopic spread of disease that is not visible to the physician in the CT dataset. A second margin is subsequently added on top of the CTV to account for uncertainties that arise from both inter- and intra-fractional motion, resulting in the internal target volume (ITV). The planning target volume (PTV) encompasses the ITV and is larger by margins to account for set-up variations, geometric uncertainties, and machine tolerances (29, 33). Subsequently, OARs and critical structures are also segmented. OAR segmentations are necessary, as they serve as dose limiting structures during treatment plan optimization. They need to be spared for successful treatment with minimal toxicities to ensure suitable long-term quality of life for patients.

The radiation dose distribution and hence TCP and NTCP depend on the radiation therapy technology used. Modern radiation therapy techniques such as stereotactic body radiation therapy (SBRT) have been developed to provide better control over dose

distribution, compared to conventional techniques such as three-dimensional conformal radiation therapy (3D-CRT) (30). 3D-CRT uses multiple co-planar fields to maximize tumor dose coverage and minimize normal tissue exposure. In 3D-CRT, the prescribed dose is usually delivered over the course of four to eight weeks, in 20 to 40 daily fractions. The basic idea of CRT is based on tailoring the apertures of the beam to the shape of the PTV in 3D, while masking nearby OARs (**Error! Reference source not found.**) (31). A more complex beam configuration might be required when the PTV is close to an OAR, and to achieve an acceptable dose distribution a higher number of beams are often used. However, conventional 3D-CRT may fail in cases of concave-shaped target volumes and moving targets. In addition, in 3D-CRT, beam margins by which the tumor is expanded to account for tumor and organ motion, and the planning and setup inaccuracies are large (on the order of centimeters) (31).

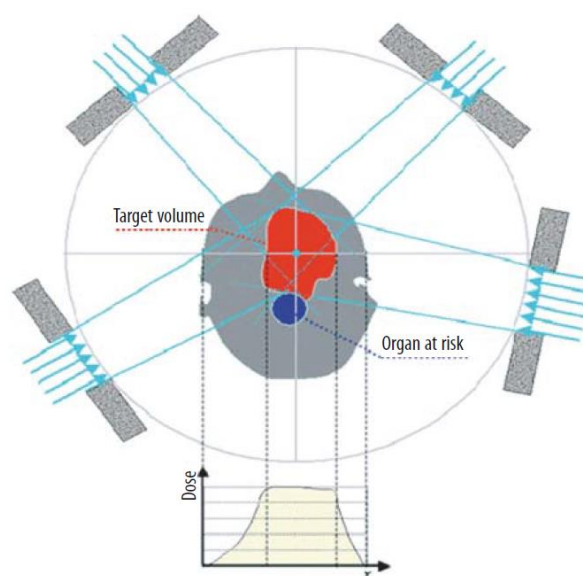


Figure 1-5. Schematic of the 3D conformal radiation therapy.

Reproduced with permission (31). Copyright 2008, SNMMI.

SBRT refers to an emerging radiotherapy procedure that has been reported to be highly effective in controlling early stage primary and oligometastatic cancers at locations throughout the abdominopelvic and thoracic cavities, and at spinal and paraspinal sites. In SBRT, the PTV contains a much smaller margin together with the target tumor, compared to when 3D-CRT is used. The major feature that separates SBRT from conventional radiation treatment is the possibility of delivering large doses in a few

fractions, which results in a high biologically effective dose (32,33). Conformation of the ablative dose to the target shape and rapid decrease in the dose outside the target is critical for minimizing the normal tissue toxicity and hence the safe delivery of the high dose. Therefore, effective use of SBRT requires a high level of confidence in the accuracy of the radiation delivery process. To achieve this accuracy, SBRT is characterized by target localization using imaging (e.g. 4DCT, MR), patient immobilization, sophisticated planning software, accurate treatment delivery technologies, and the ability to produce a steep dose gradient outside the target volume (33). In addition to these major features, there are other characteristics that distinguish SBRT from conventional radiation therapy (30) (Table 1-2). These include a general increase in the number of beams used for treatment, the frequent use of noncoplanar beam arrangements, and the use of inhomogeneous dose distributions techniques such as

Table 1-2 Comparison of some characteristics of 3D-CRT and SBRT. Reproduced with permission (30). Copyright 2010, John Wiley and Sons.

Characteristic	3D-CRT	SBRT
Dose/fraction	1.8-3 Gy	6-30 Gy
No. of fractions	10-30	1-5
Target definition	CTV/PTV (gross tumor + clinical extension), tumor may not have a sharp boundary	GTV/CTV/ITV/PTV (well-defined tumors, GTV = CTV)
Margin	Centimeters	Millimeters
Dosimetry monitoring	Indirect	Direct
Primary imaging modalities used for treatment planning	CT	Multimodality: CT/MR/PET-CT
Maintenance of high spatial targeting accuracy	Moderately enforced (moderate patient position control and monitoring)	Strictly enforced (sufficient immobilization and high frequency position monitoring through integrated image guidance)
Need for respiratory motion management	Moderate – Must be at least considered	Highest
Interaction with systemic therapies	Yes	Yes
Staff training	Highest	Highest + special SBRT training

intensity modulated radiation therapy (IMRT) and volumetric modulated arc therapy (VMAT) (30). IMRT utilizes forward or inverse radiation treatment planning to determine and deliver the necessary dose distribution through the use of multileaf collimators (Figure 1-6) (34). VMAT is a more advanced type of IMRT that decreases the delivery time by applying the dose in a single gantry arc and improves the dose conformity by using the full 360° range of gantry rotation (35).

Accurate delivery of ablative radiation is challenging for extracranial lesions due to inter- and intra-fraction tumor and organs motion. Respiration-induced motions of the target and OAR renders the treatment delivery even more challenging for lung tumors (33). This motion can cause inaccuracies and uncertainties in radiation therapy, and artifacts in imaging of the thoracic tumors resulting in higher probabilities of treatment complications such as irradiating normal tissue (increase in NTCP) and undesirable dose distribution in target tumor (decline in TCP) (36,37). Therefore, motion compensation methods are highly essential for safe delivery of large fractions of radiation therapy. Section 1.3 describes current motion management methods as well as an overview of the real-time tumor tracking workflow previously proposed by our group.

Current methods of radiation therapy treatment planning assume a homogeneous

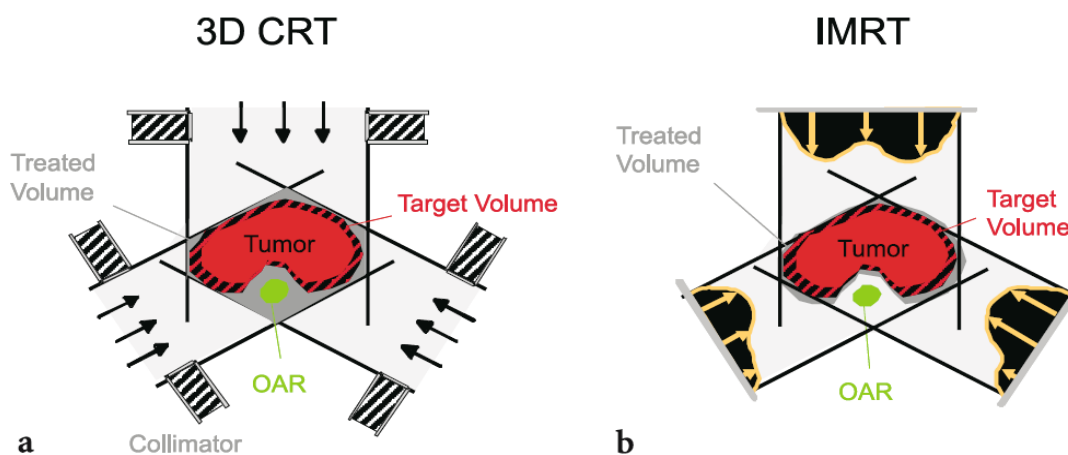


Figure 1-6. 3D CRT vs. IMRT. (a) in 3D CRT, dose conformity is limited to the open/close aperture configuration, while (b) IMRT, offers higher dose conformity resulting in smaller margins and higher potential for less toxicity to OAR. Reproduced with permission (100). Copyright 2006, Springer-Verlag Berlin Heidelberg.

distribution of lung function (38). However, as mentioned in section 1.1.2, pulmonary abnormalities such as COPD and asthma commonly coexist with lung cancer, leading to pulmonary function heterogeneity. To limit high radiation dose delivery to healthy tissue, functional avoidance treatment planning has been proposed (5,38,39). This method preferentially spares the functional lung tissue from radiation dose during treatment planning. Section 1.4 provides more information on functional avoidance planning, the current functional imaging methods and an overview of our proposed ventilation imaging technique that can be used for functional avoidance planning.

1.3 «Motion Management Methods»

Accounting for inter- and intra-fraction motions of the target and OAR are critical for the safe delivery of radiation dose. The location of the target and OAR may be different from their location at the radiation treatment planning and simulation. Accurate positioning of the target lesion in the isocenter of the radiation therapy machine requires that the body geometry during the treatment session is almost identical to the body geometry during treatment planning simulation. In addition, it is required to suppress or, if possible, eliminate the voluntary motion of the body during treatment (33). Henrik Blomgren and Ingmar Lax designed a body frame to minimize the inter-fraction motion. This body frame allows comfortable repositioning of the patient's body relative to the frame. The frame is equipped with fiducial markers that determine the coordinates system relative to the frame geometry, and hence enable an accurate localization of the body relative to the simulator and the treatment accelerator (40). Vacuum systems have also been developed for enforcing patient immobilization and are used in some centers (33). Although the body frames or the vacuum systems largely resolves the inter-fraction motion issues, the intra-fraction motion and deformation of the lungs and the tumor caused by respiration can significantly increase the uncertainties in radiation treatment and compromise its accuracy and effectiveness. To account for respiratory motion, several motion compensation methods have been proposed.

1.3.1 Motion Encompassing

In motion encompassing treatment planning, the PTV includes the target volume at end-exhalation phase, or GTV (obtained from treatment planning 4DCT), along with a large margin that encompasses the entire path of the tumor motion/deformation (Figure 1-7) (41). In this method, the PTV which is irradiated with high dose radiation is larger than

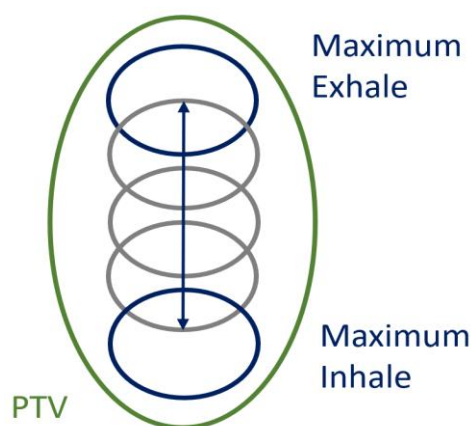


Figure 1-7. Motion encompassing. PTV includes the entire path of tumor's motion from expiration to inspiration, along with extra safety margins.

the GTV and may include a significant volume of the healthy lung tissue (42). This may lead to higher chances of radiation-induced toxicities and higher NTCP. The motion encompassing method can only be used when the amplitude of the target motion is less than 5mm, because otherwise the potential damage extent to the healthy tissue is deemed unacceptable (3). Several studies have investigated the amplitude of the motion of the tumor in different directions (43–46), and a few others studied the range of motion during diaphragm contraction (47,48). According to Table 1-3, on average the range of lung tumor motion/deformation is larger than 5 mm (3). Therefore, other motion compensation methods with better accuracy for sparing of normal tissue are required.

1.3.2 Gated Methods

Gated radiation therapy methods for lung cancer are developed based on the assumption that during the respiratory cycle there is a particular span of time where the amplitude of the respiratory motion is small (Figure 1-8). To decrease the treatment field margins (for PTV), in gated procedures, the radiation beam is only applied during the portion of the

breathing cycle with the smallest target motion (the gating phase). The gating phase of the breathing cycle has to be identified and verified positionally for each patient and the beam has to be switched on and off accordingly during the treatment session (49). Real-time information on the breathing cycle is required for this method to enable synchronizing the on and off turning of the beam. Breathing monitoring devices for

Table 1-3 Respiratory-induced motion of the lung tumor and diaphragm in different directions. Reproduced with permission (3). Copyright 2006, John Wiley and Sons.

Study	Site	Direction	Average (min - max) (mm)	Modality
Stevens et al. (43)	Tumor	SI	4.5(0-22.0)	CT
Shimizu et al. (44)	Tumor	AP	6.4(2.0-24.0)	CT
Plathow et al. (45)	Tumor	SI	9.5(4.5-16.4)	MRI
		AP	6.1(2.5-9.8)	
		LR	6.0(2.8-9.8)	
Seppenwoolde et al. (46)	Tumor	SI	5.8(0-24.6)	Fluoroscopy
		AP	2.5(0-8.2)	
		LR	1.5(0-2.8)	
Giraud et al. (47)	Diaphragm	SI	35.0(3.0-95)	CT
Davies et al. (48)	Diaphragm	SI	12.0(7.0-28.0)	Ultrasound

SI: Superior-inferior, AP: Anterior-posterior; LR: Left-right

respiratory gating most often rely on surrogates for the actual motion of the target, such as an external optical skin marker or a pressure sensor.

The variability and irregularity of breathing patterns results in a lack of predictability of breathing motion. Therefore, as shown by Korreman et al. (50), image guidance is of utmost importance for respiratory gated treatments. The correspondence between the breathing motion recorded from the external surrogate and the breathing motion of the target can change, not only from fraction to fraction but also within each treatment fraction. Therefore, when external surrogates are used for motion monitoring, the correspondence between the motion of the surrogate and target motion needs to be

updated and verified regularly. Otherwise, the target may not receive the effective dose while the normal tissue receives toxic radiation (49).

Several imaging techniques can be used during radiation therapy and for treatment planning of gated procedures. During treatment, radiographic and fluoroscopic kV imaging are now standard for new machines. Imaging equipment can either be mounted

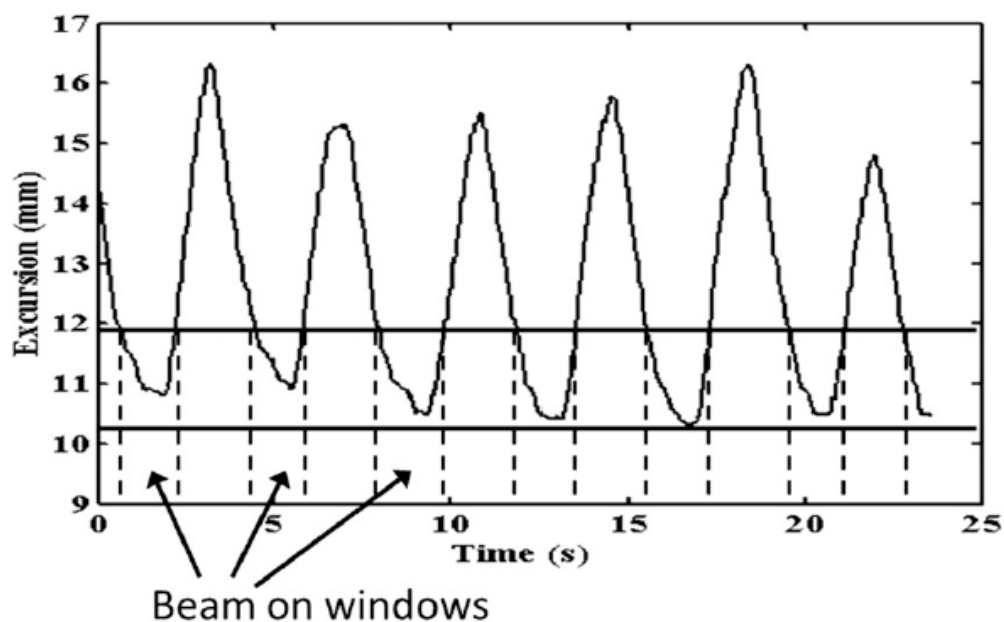


Figure 1-8. Gated Radiation therapy. The motion of the tumor is smallest at certain windows of time (gates) during respiration. The radiation is applied only during these gates. Reproduced with permission (49). Copyright 2015, British Journal of Radiology.

on the linear accelerator gantry, which is mostly orthogonal to the treatment beam, or can be independently mounted on the ceiling or floor of the treatment room, orthogonally. Two orthogonal imaging setups can be combined to provide semi-3D information. Imaging units mounted on the gantry can also be used for cone-beam CT imaging. Because the acquisition time of cone-beam CT (CBCT) is long compared to the breathing cycle, the target position image may appear blurred in the image. 4D CBCT has also been developed that acquires phase-resolved CBCT(49,51).

Respiratory gated methods do not completely abolish the need for margins when assigning the PTV. Breathing motion patterns are not stable (especially among lung

cancer patients), and hence not completely reproducible in the spatial domain. If not accounted for, irregularities in the breathing cycle can render the gated procedures unreliable. Therefore, treatment margins are required to account for the uncertainties caused by the residual motion. The uncertainties (and hence the margins) can be reduced by combining the gated procedures with motion limiting methods. This increases the chance of delivering the dose to the target as prescribed by the treatment plan (33,52). Although the modern gated methods can improve the confidence in the accuracy required for an effective SBRT, they come with shortcomings. The gated sessions inevitably take longer and this increase in the treatment time can cause inconvenience for the patient that can lead to body dislocation relative to the treatment frame, and hence a decrease in the accuracy of treatment delivery. In addition, longer treatment times can have potential radiobiological consequences caused by the decreased average dose ratio during treatment (33).

1.3.3 Motion Limiting Methods

Motion limiting methods aim at controlling the respiratory motion amplitude by limiting the breathing volume. Abdominal compression devices can be used along with the body frames during SBRT to decrease the respiration-induced tumor motion and hence the treatment margins. These devices, however, can cause discomfort or even anxiety for some patients, that may lead to an increased variability in tumor motion. In addition, the abdominal compression does not eliminate the tumor motion, and this method is not practical for obese patients (53).

Breath-hold techniques attempt to eliminate respiratory motion either voluntarily or by using occlusion valves. The holding of the breath allows for a temporary immobilization of the target tumor when the radiation is planned to be applied. Figure 1-9 illustrates typical respiratory motion amplitude variation as a function of time where this motion limiting method is utilized. Patients must be trained on the required breathing maneuver for both treatment planning CT and radiation therapy session. The patients are required to hold their breath for 10-20 seconds in each iteration. While relatively effective for target immobilization, breath-hold techniques are not very commonly used because most lung

cancer patients have poor pulmonary function and cannot undergo breath-hold procedures (54).

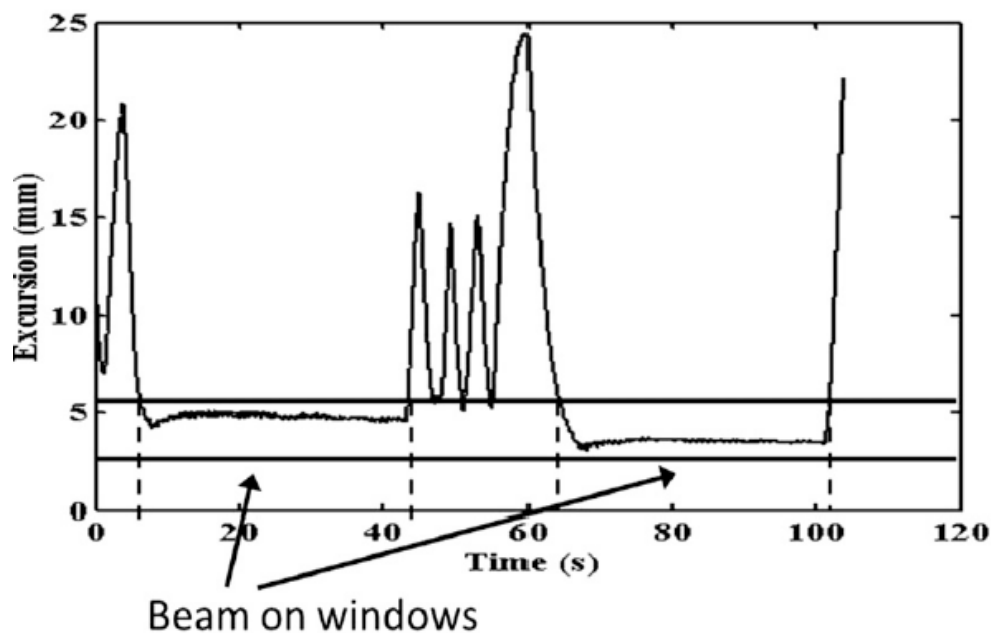


Figure 1-9. Breath-hold methods. The respiratory motion amplitude decreases during the breath-hold span. The radiation is applied during this span to reduce uncertainties caused by tumor motion. Reproduced with permission (49). Copyright 2015, British Journal of Radiology.

1.3.4 Real-time Tracking Methods

Real-time tumor tracking has been proposed as an alternative motion management technique in which the radiation beam dynamically follows the target throughout the treatment. A real-time tumor tracking system ideally follows the motion and deformation of the tumor during the entire respiratory cycle, allowing a continuous radiation treatment. There are certain requirements that need to be met for achieving a radiation therapy system with real-time tracking as the motion management technique, including (but not limited to): 1) an accurate estimation of the tumor location and geometry in real-time, 2) in advance prediction of the tumor motion/deformation to account for the delays, 3) an adaptive radiation dose planning system, and 4) a beam alignment system (55,56).

Although imaging techniques are available for use during treatment, for high precision tumor tracking purposes in real-time, markers implanted in the tumor have been proposed to increase visibility. This technique has been developed by SynchronyTM Respiratory Tracking system (Accuray, Sunnyvale, CA). In this system, gold fiducials are implanted inside the tumor and their motion is monitored by a pair of orthogonal X-ray images. In addition to the image data, a correlation model used as a location predictor is developed with an optical monitoring system tracking light emitting markers placed on a vest worn by the patient. The correlation model compensates for the time delay between data acquisition and the repositioning of the accelerator. The accelerator is robotically controlled and allows for non-isocentric beam delivery within a solid angle of over 2π . The position of the external markers is continuously monitored while the X-ray imaging of the internal fiducials is performed every 3–5 beams (a flexible parameter). Apart from accuracy, another major advantage of this method is that the patient breathes freely during the treatment (57). Tracking the tumor without the need for simultaneous imaging by implantation of radiofrequency beacons has also been reported, e.g. using the Calypso system (58). Similar to other tracking systems that are based on implanted fiducials, with these tracking systems, the translational movement of the tumor can be captured and compensated for, while the rotation and deformation is not accounted for. As a result, treatment margins of up to 5 mm may be required depending on the case (33,59). Recent studies indicate that, during respiration, the size of the target tumor can vary by up to 62% (60). As such, an effective tumor tracking method should be able to estimate the tumor deformations as well as translation and deformation. In addition, marker implantation is an invasive procedure and can be associated with side effects. Risks of pneumothorax for percutaneous implantation is reported to be as high as 30%, with 10% of the cases requiring intervention (61,62). To avoid marker implantation, an improved tracking method, X-sight Lung (Accuray, Sunnyvale, CA) has been developed that can dynamically track tumor motion based on the radiograph images for certain lung cases (in some centers, about 30% of patients). Concurrent X-ray imaging and radiation therapy, however, has raised some concerns about the additional imaging dose (33).

1.3.5 Tumor Tracking Workflow

A real-time tumor tracking workflow has been previously proposed by our group (63). This tumor tracking scheme will not require simultaneous imaging during the treatment, can also estimate motion and deformation of the tumor, and will only use external markers. In addition, this method is potentially less sensitive to irregularities in the breathing pattern. An overview of this method is shown in Figure 1-10. During the pre-treatment step, an optical tracking system is incorporated into the treatment planning 4DCT acquisition. A tumor motion and deformation estimation algorithm based on an accurate patient-specific biomechanical model of the lung is developed using the treatment planning 4DCT data. The chest surface motion data is acquired simultaneously with the treatment planning 4DCT using optical tracking of the external markers. The chest surface motion data can be correlated to the tumor motion/deformation obtained from the finite element (FE) model.

The information from chest motion data is considered as input parameters while the parameters of the biomechanical model (in a compact form) will be used as the output for training a predictive model (e.g. an artificial neural network). After training the predictive model, a relationship is established between the chest surface motion data and the parameters of the FE model that directly provides the tumor motion/deformation. For more detailed information on the proposed real-time tracking workflow, see (63).

The accuracy of the biomechanical model used in this method is critical to the successful development of the real-time tracking. The second chapter of this thesis explains development of an accurate biomechanical model for tumor motion and deformation estimation.

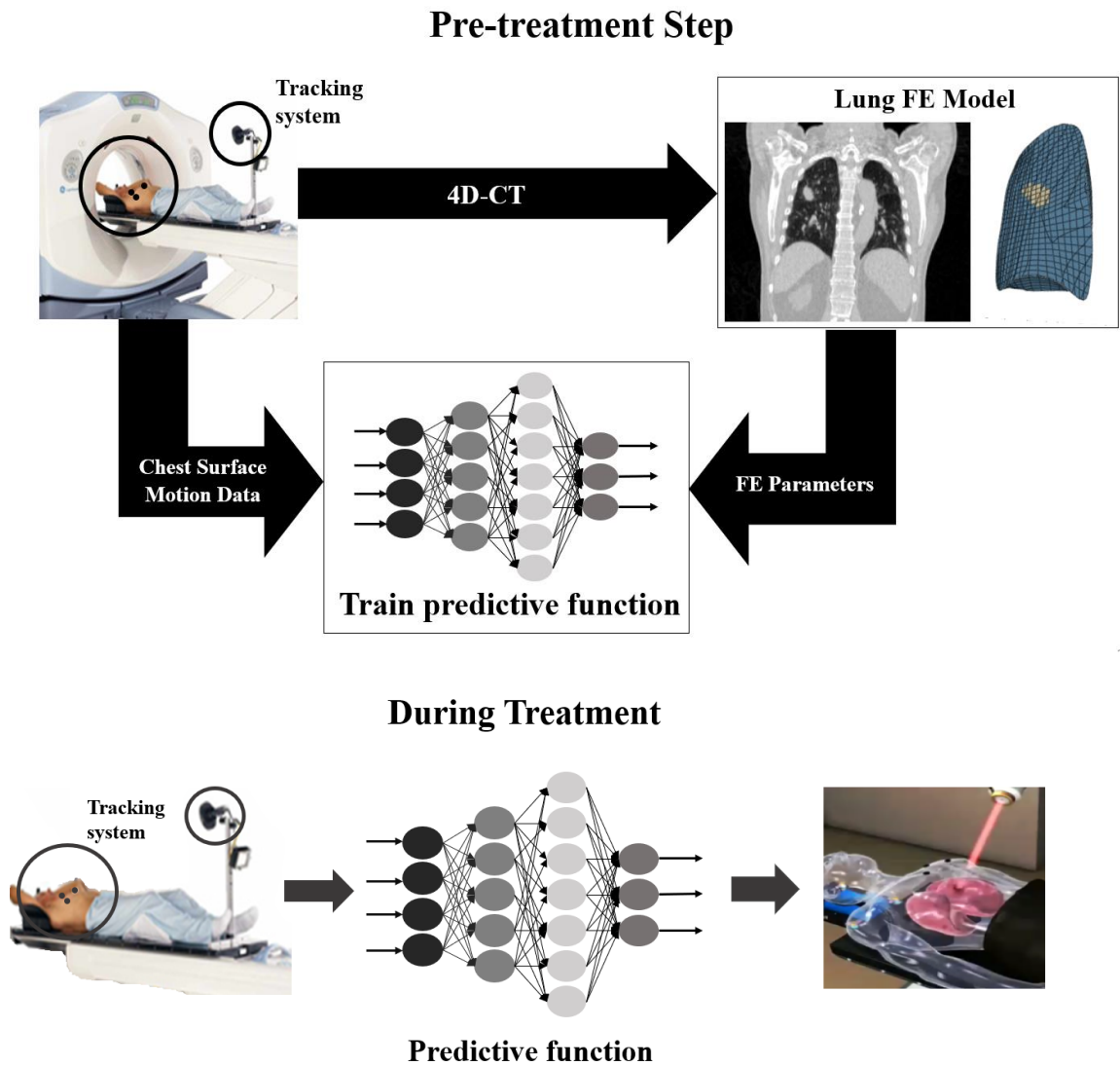


Figure 1-10. The biomechanics-based real-time tumor tracking workflow.

1.3.6 Biomechanical model-based tumor motion/deformation estimation

Lung motion/deformation estimation using information from 4DCT scans has been widely studied for different applications including tumor motion tracking. Although intensity-based deformable image registration (DIR) methods have been employed to find the motion/deformation fields of the lungs and the tumor for dose calculation and treatment planning purposes, their application in real-time tumor tracking is limited to a few studies (56,64–66). In addition, intensity-based DIR methods are solely based on

4DCT image data, and they do not take into account the physical properties or physiological mechanisms involved in breathing. Therefore, they are prone to errors associated with non-uniqueness of the resulting displacement field, and registration errors in areas with low image contrast. Handling the sliding motion of the lungs can also be challenging for motion estimation using intensity-based DIR methods. Biomechanical models can be adapted to address these limitations; they are widely used alone or in combination with intensity-based methods. In contrast to intensity-based DIR, biomechanics-based computational models encompass certain aspects of breathing dynamics rendering this approach more robust and realistic. Patient-specific lung biomechanical models that use the thoracic image data to extract the lung's geometry and boundary conditions have previously been proposed. Several studies investigated the effects of model parameters, including tissue mechanical properties (67–69), and boundary conditions (70) on modeling accuracy. Recently, hybrid hierarchical approaches have been proposed, in which finite element (FE)-based models are used in conjunction with intensity-based DIR methods to predict deformation field of the lung in a respiratory cycle, and to register lung CT image pairs. For example, Han L. et al., proposed a hybrid biomechanical model-based DIR for lung peak CT pairs, and showed that the resulting deformation field can more realistically describe the underlying physiology to improve the registration accuracy compared to the intensity-based DIR algorithm (71).

In chapter 2, we describe a heterogeneous biomechanical model of the lung for accurate estimation of the tumor motion and deformation. This biomechanical model takes into account the heterogeneity in the mechanical behavior of the lung tissue that is caused by co-existing COPD phenotypes.

1.4 «Functional Avoidance Treatment Planning»

As mentioned in section 1.2.1, EBRT is the main method of treatment for many lung cancer patients. However, EBRT is associated with increased risk of radiation-induced toxicities such as radiation pneumonitis or radiation fibrosis. Radiation pneumonitis with clinical symptoms occurs in 30-40% of lung cancer patients after receiving concurrent

chemoradiotherapy and can have an adverse impact on their quality of life. This adverse effect sometimes results in oxygen dependence and is fatal in severe cases (25).

Current radiation therapy treatment planning methods used in many centers assume that the lung function is homogeneous, and do not take into account regional differences in pulmonary function. Therefore, the goal in treatment planning is to minimize the radiation dose to the total lung volume. However, as mentioned in section 1.1.3, many lung cancer patients suffer from comorbidities such as COPD, which affect the regional distribution of lung function. Functional avoidance-based treatment planning has emerged as a new treatment planning approach, aiming to overcome the limitations caused by the assumption of homogeneous function (25). Ideally, the radiation therapy dose should be planned based on minimizing the radiation dose to the well-functioning volumes of the lung while favoring radiation deposition in the lower functioning volumes.

Regional information on lung function is a requirement for functional avoidance planning. Over the last decade, functional imaging maps have been investigated for lung cancer treatment planning. Positron emission tomography (PET) and single-photon emission computed tomography (SPECT) scans can be used to obtain functional information in terms of ventilation and perfusion (72,73). Some researchers have used PET or SPECT for functional avoidance planning and assessment of the radiation treatment response (39,74). Nuclear medicine imaging approaches have a relatively low resolution compared to other imaging modalities. Hyperpolarized ^3He MR imaging can provide information on regional ventilation, and hyperpolarized ^{129}Xe MRI can be used to obtain information on ventilation, perfusion, or gas exchange (75–77). Although hyperpolarized gas MRI has enough temporal resolution for ventilation imaging, it is relatively costly and require tracer gases and additional equipment. Xe-enhanced CT can be used to provide direct assessment of ventilation distribution (78). Xe (Xenon) gas is also relatively costly and requires associated hardware to control the delivery. In addition, this method is limited to axial coverage of about 12-15cm, which may not be sufficient for thoracic imaging. Using any of the abovementioned modalities for a functional imaging would also require an extra step of multi-modal image registration with the

radiation therapy treatment planning CT scans that may introduce errors in lung function mapping.

4DCT-based ventilation imaging (CTVI) has recently emerged as a cost-effective and accessible alternative for functional avoidance planning. The CTVI can be considered as “free information” for functional avoidance planning because 4DCT scans are part of the routine care for lung cancer patients in many centers. Therefore, acquiring CTVI only involves additional computational steps, e.g. image processing and analysis.

CTVI-based functional avoidance planning is currently investigated in a number of clinical trials (79–81). Attempts have been made to validate different CTVI techniques against a wide range of clinical and experimental modalities for ventilation imaging, including ^{99m}Tc -labelled diethylenetriamine pentaacetate (DTPA) V-SPECT (82), ^{68}Ga (Galligas) PET (83), ^3He MRI (84), ^{129}Xe MRI (85), ^{81m}Kr (86) and Technegas V-SPECT (87).

1.5 «4DCT Ventilation Imaging Methods»

Different approaches have been proposed for CTVI where most of them rely on a deformable image registration (DIR) algorithm, combined with a ventilation metric. Some groups used off-the-shelf DIR algorithms while others utilized in-house DIR methods. The accuracy of the DIR algorithm is critical to the accuracy of the generated CTVI, however, there has not been a consensus on which algorithm should be used. For a comprehensive review on different DIR algorithms that have been used for CTVI, see (88). As for the ventilation metric, current CTVI methods are generally classified as either Hounsfield units (HU)-based or Jacobian-based algorithms. A few studies have investigated the combination of the two (88). In the HU-based approaches, the change in the amount of air in the voxels is considered the surrogate for ventilation. Simon et al. proposed a relationship between manually registered CT values in Hounsfield units (HU), $\text{HU}_{\text{inhale}}$ and $\text{HU}_{\text{exhale}}$, and the regional volume change. They assume that the fraction of air in a CT region is given by:

$$F_{\text{air}} = -\frac{\text{HU}}{1000}, \quad (1)$$

where HU is the image intensity of each voxel (89). The fractional change in air content within a specified volume is then given by:

$$\frac{\Delta V}{V_{ex}} = \frac{(F_2 - F_1)}{F_1(1 - F_2)}, \quad (2)$$

where ΔV is the local volume change due to inspiration, V_{ex} is the volume of air within the exhale CT volume of interest, F_1 is the fraction of air in the exhale CT volume of interest and F_2 is the corresponding fraction of air in the inhale CT volume of interest. If we consider the initial exhale volume as a discretized CT voxel, and assume that a three-dimensional vector transformation exists to map the set of inhale lung CT voxels into the exhale image domain, one can derive the following expression for local ventilation in terms of registered CT numbers corresponding to inhalation and exhalation breathing states:

$$\frac{\Delta V}{V_{ex}} = 1000 \frac{(\bar{H}_{inhale}^{VOI} - HU_{exhale})}{HU_{exhale}(1000 + \bar{H}_{inhale}^{VOI})}, \quad (3)$$

where \bar{H}_{inhale}^{VOI} is the average of all the HU corresponding to the set of inhale voxels that map into the exhale voxel under consideration (90).

Concerns due to physiological violation of the ventilation model given by this equation, as well as uncertainty resulting from image noise, data acquisition and image reconstruction artifacts have led others to investigate alternative methods for quantifying lung function that are independent of the image CT values. Regional volume can be measured using the Jacobian of the DIR deformation field, $\Phi(\vec{x})$, alone (91,92). The Jacobian is defined as the determinant:

$$J_{\Phi}(\vec{x}) = \det \begin{bmatrix} 1 + \frac{\partial \Phi_1(\vec{x})}{\partial x_1} & \frac{\partial \Phi_1(\vec{x})}{\partial x_2} & \frac{\partial \Phi_1(\vec{x})}{\partial x_3} \\ \frac{\partial \Phi_2(\vec{x})}{\partial x_1} & 1 + \frac{\partial \Phi_2(\vec{x})}{\partial x_2} & \frac{\partial \Phi_2(\vec{x})}{\partial x_3} \\ \frac{\partial \Phi_3(\vec{x})}{\partial x_1} & \frac{\partial \Phi_3(\vec{x})}{\partial x_2} & 1 + \frac{\partial \Phi_3(\vec{x})}{\partial x_3} \end{bmatrix}$$

which calculates the differential expansion (or contraction) at position \vec{x} in the image. Consider $B_{\vec{x}}$ as a small box around \vec{x} in the exhale image such that $\Phi(B_{\vec{x}})$ is the corresponding deformed box in the inhale image. The Jacobian determinant of the deformation $\Phi(\vec{x})$ at \vec{x} is

$$J_{\Phi}(\vec{x}) = \frac{vol(\Phi(B_{\vec{x}}))}{vol(B_{\vec{x}})}, \quad (4)$$

where $vol(B_{\vec{x}})$ is the volume of the small box centered at \vec{x} and $vol(\Phi(B_{\vec{x}}))$ is the volume of the corresponding deformed box. Note that the fractional change in volume equals the Jacobian determinant of the deformation field at that location. The Jacobian calculation is independent of the CT values and only depends on the DIR transformation Φ .

In Chapter 3 we describe our proposed CTVI method that combines a biomechanical model-based DIR with an accurate air segmentation algorithm. The proposed CTVI method has qualitatively and quantitatively been compared against the patients' hyperpolarized ^3He MR.

Next sections (1.6 to 1.9) present the theoretical background required for developing the proposed methods for tumor motion/deformation estimation using the lung biomechanical model, and the proposed 4DCT ventilation imaging technique.

1.6 «Image Segmentation»

Image segmentation is defined as partitioning a two-dimensional (2D) or 3D image into multiple classes. Each class is called a segment and includes voxels that share a property, hence belong to that class. Image segmentation has various applications in the field of computer vision, including object recognition, image database look-up, or image compression. In medical image analysis, image segmentation is usually used to outline an object or organ of interest manually or automatically. For example, before a tumor is analyzed in a CT image, it must be detected and isolated from the rest of the image. This task is performed using image segmentation. Segmentation of medical images also allows comparison of object/organ of interest between different datasets or modalities and

monitoring changes in the object/organ of interest (e.g. in treatment response assessment). It also enables extracting useful quantitative information from images.

1.6.1 Region Growing Algorithm

Region growing is an iterative algorithm used for image segmentation that has a similar concept to clustering algorithms such as k-means clustering (93). Initially, one or more points (seeds) are assigned in each of the segments either manually or automatically. In each iteration, the pixels around a seed point are examined and determined whether each pixel belongs to the segmentation class (segment). If yes, this pixel is added to the seeds of that segment. The choice of criterion by which a pixel is allocated to a segment has an impact on the final result of segmentation. For example, one criterion is to choose a pixel as a member if its grayscale value is close to the average grayscale values of the region. The definition of “closeness” can also influence the results. In many applications, closeness is defined as a distance smaller than 1-3 times the standard deviation of the pixels’ intensity values in the region. This process continues until all the pixels in the image are allocated to one and only one of the growing regions (93).

1.7 «Image Registration»

Image registration is defined as the process of aligning two or more images taken from the same scene under different conditions, e.g. images taken from a landscape from slightly different angles or viewpoints, CT images taken from a tumor before and after the course of treatment, the MR and the CT taken from a patient’s brain, etc. Image registration involves designating one of the images as the fixed (reference) image, while the other image is assigned as the moving image. The geometric transformations and/or local displacement fields are applied to the moving image so that it aligns with the fixed image (94,95). Usually, image registration is performed as a preliminary step to prepare the images for another image processing algorithm. For example, the CT images acquired from the patient’s lung at end-exhalation phase is registered to the image of the same patient’s lung at end-inhalation phase to extract and quantify certain pathophysiological conditions (96).

Based on the process that was involved between the acquisition of the two images, a combination of different transformations might be required to register the images. The transformation can be rigid (translation and rotation), affine (rigid + scaling and shearing), or deformable registration (2-3 degrees of freedom for each pixel). Figure 1-11 shows the flowchart of a registration algorithm. There are essential components to any image registration algorithm (97). A metric is used to compare the closeness of the moving and the fixed image after a transformation. Proper choice of the metric can have a significant impact on the performance and the results of the registration. Commonly used metrics include: mean squared errors, normalized cross correlation, and normalized mutual information. The latter is the best choice for multi-modality image registration (e.g. between MR and CT). An optimizer is required to find the minimum (or maximum, based on the choice of metric) of the metric that will result in the best alignment of the two images. Choosing the proper optimizer and its parameters (e.g. step size, relaxation factor, etc.) can be very important for performance of the registration algorithm. The interpolators are used for calculating the pixels grayscale values after transformation. When the image is transformed, the pixels may land on non-integer locations (i.e. not on the fixed image grid). Therefore, an interpolator is required to reconstruct the transformed image.

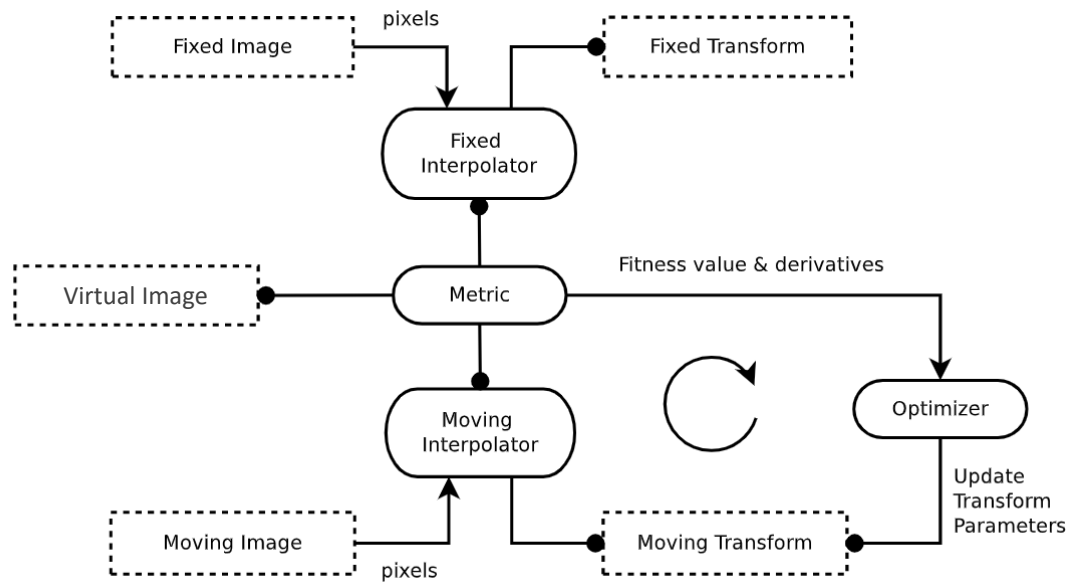


Figure 1-11. Flow chart of a general registration algorithm. A metric is used to compare the fixed image with the moving image after each time the moving transform is updated. The optimization stops when the metric or changes in the metric are smaller than a predefined limit. The virtual image is reconstructed after the optimization is completed. Adapted from The ITK Software Guide Book 2 Fourth Edition, by Johnson H.J., McCormick M.M., Ibáñez L., and the Insight Software Consortium.

1.8 «Theory of Elasticity»

Elasticity is a property of solid materials to regain their original shape after an external force is removed. Theory of elasticity describes the mechanical behavior (i.e. deformation and failure) of the elastic materials under the application of external force. Continuum mechanics deals with the mechanical behavior of materials that can be considered as a continuous mass rather than discrete parts or particles and is therefore based on the continuum hypothesis: “*matter is continuously distributed, and regardless of how small volume elements the matter is subdivided into, every element will contain matter. The matter may have a finite number of discontinuous surfaces, for instance fracture surfaces or yield surfaces, but material curves that do not intersect such surfaces, retain their continuity during the motion and deformation of the matter*” (98).

A continuum is characterized by a mass dm , contained in an elementary volume $d\tau = \frac{dm}{\rho}$. ρ is referred to as the mass density. A material continuum occupying a volume v with a surface o (initial state), will reach a new equilibrium state with the volume V and the surface O (final state). The position of the material particle is defined in a Cartesian coordinate as (the summation over the dummy index s is omitted for brevity):

$$\mathbf{X} = a_1 \mathbf{i}_1 + a_2 \mathbf{i}_2 + a_3 \mathbf{i}_3 = a_s \mathbf{i}_s, \quad (5)$$

where \mathbf{i}_s is the base unit vector of the coordinate axes. Similarly, the final state of the material particle is:

$$\mathbf{x} = x_1 \mathbf{i}_1 + x_2 \mathbf{i}_2 + x_3 \mathbf{i}_3 = x_s \mathbf{i}_s. \quad (6)$$

The displacement vector moving the material particle from the initial state to the final state is:

$$\mathbf{u}(\mathbf{X}, t) = \mathbf{x}(\mathbf{X}, t) - \mathbf{X}, \quad (7)$$

which can be written as:

$$\mathbf{u}(\mathbf{X}, t) = u_1 \mathbf{i}_1 + u_2 \mathbf{i}_2 + u_3 \mathbf{i}_3 = u_s \mathbf{i}_s, \quad (8)$$

and therefore:

$$u_s = x_s - a_s. \quad (9)$$

See Figure 1-12.

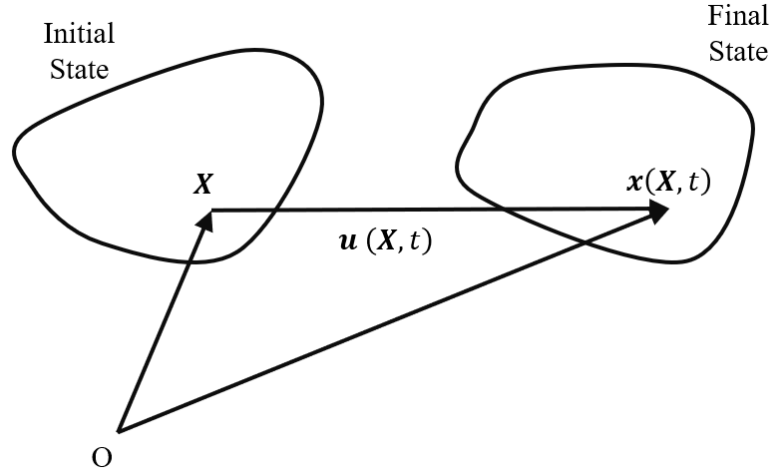


Figure 1-12. A particle in the elastic geometry at its initial state (\mathbf{X}), displaced by $\mathbf{u}(\mathbf{X}, t)$ to its final state ($\mathbf{x}(\mathbf{X}, t)$).

The displacements, i.e. the projections of the displacement vector (i.e. u_s), are functions of the initial position of the material particle (a_s), and hence the dependence of \mathbf{u} on \mathbf{X} in Eq. 7. For the equation to have a unique solution, the Jacobian (Eq. 10) must not vanish in the closed domain $v + o$.

$$J(a_1, a_2, a_3) = \left| \frac{\partial x_s}{\partial a_k} \right| = \left| \delta_{sk} + \frac{\partial u_s}{\partial a_k} \right| = \begin{vmatrix} 1 + \frac{\partial u_1}{\partial a_1} & \frac{\partial u_1}{\partial a_2} & \frac{\partial u_1}{\partial a_3} \\ \frac{\partial u_2}{\partial a_1} & 1 + \frac{\partial u_2}{\partial a_2} & \frac{\partial u_2}{\partial a_3} \\ \frac{\partial u_3}{\partial a_1} & \frac{\partial u_3}{\partial a_2} & 1 + \frac{\partial u_3}{\partial a_3} \end{vmatrix}. \quad (10)$$

The Jacobian (J) is the deformation gradient tensor, also denoted by \mathbf{F} . \mathbf{F} can be re-written as:

$$\mathbf{F} = \mathbf{I} + \nabla \mathbf{u}, \quad (11)$$

where $\nabla \mathbf{u}$ is the displacement gradient, and \mathbf{I} is the identity tensor. The following equation is derived from Eq. 7 and Eq. 11 using differential calculus principles:

$$d\mathbf{x} = d\mathbf{X} + (\nabla \mathbf{u})d\mathbf{X} = \mathbf{F}d\mathbf{X}, \quad (12)$$

where $d\mathbf{x}$ and $d\mathbf{X}$ are the distance between two infinitesimally close points in the final and initial volumes. Therefore, the square of the linear elements (i.e. the inner product of the distance $d\mathbf{x}$ with itself) in the final volumes becomes:

$$ds^2 = d\mathbf{x} \cdot d\mathbf{x} = d\mathbf{X}\mathbf{F}^T\mathbf{F}d\mathbf{X}. \quad (13)$$

We substitute $\mathbf{C} = \mathbf{F}^T\mathbf{F}$, and obtain

$$ds^2 = d\mathbf{X}\mathbf{C}d\mathbf{X}, \quad (14)$$

where \mathbf{C} is called the right Cauchy-Green deformation tensor. In distance-preserving transformations (e.g. rigid body motion), $ds^2 = d\mathbf{X} \cdot d\mathbf{X}$ and therefore $\mathbf{C} = \mathbf{I}$. Substituting Eq. 11 in Eq. 13 we can find the relationship between the right Cauchy-Green deformation tensor and the displacement gradient:

$$\mathbf{C} = (\mathbf{I} + \nabla\mathbf{u})^T(\mathbf{I} + \nabla\mathbf{u}) = \mathbf{I} + \nabla\mathbf{u} + (\nabla\mathbf{u})^T + (\nabla\mathbf{u})^T(\nabla\mathbf{u}). \quad (15)$$

\mathbf{E} is the Green-Lagrange strain tensor and is calculated from the displacement as:

$$\mathbf{E} = \frac{1}{2}[\nabla\mathbf{u} + (\nabla\mathbf{u})^T + (\nabla\mathbf{u})^T(\nabla\mathbf{u})]. \quad (16)$$

Therefore:

$$\mathbf{C} = \mathbf{I} + 2\mathbf{E}. \quad (17)$$

To obtain the Green-Lagrange strain tensor from the deformation gradient tensor \mathbf{F} , we can use $\mathbf{C} = \mathbf{F}^T\mathbf{F}$ and Eq. 17:

$$\mathbf{E} = \frac{1}{2}[\mathbf{F}^T\mathbf{F} - \mathbf{I}]. \quad (18)$$

The advantage of using this formulation to calculate the Green-Lagrange strain tensor is that it uses the reference body configuration instead of the deformed (final) state.

To obtain the strain values in all directions at each point from displacements, we start with the simple case and assume that the displacements (and their partial derivatives) are

small. In this case, in Eq. 16 the higher order term $(\nabla \mathbf{u})^T(\nabla \mathbf{u})$ becomes negligible, and we can simplify the strain tensor to the infinitesimal strain tensor:

$$\boldsymbol{\varepsilon} = \frac{1}{2}[\nabla \mathbf{u} + (\nabla \mathbf{u})^T]. \quad (19)$$

Now the strain values can be obtained from displacements in the Cartesian coordinate as:

$$\varepsilon_{ij} = \frac{1}{2} \left(\frac{\partial u_i}{\partial X_j} + \frac{\partial u_j}{\partial X_i} \right). \quad (20)$$

This formulation can be used to calculate strains from displacement when the deformation of the elastic material under the external force is infinitesimal, and no intrinsically nonlinear elastic behavior is expected from the material.

In cases where the material undergoes large deformations, we can no longer ignore the higher order terms in the calculation of the strain tensor. The strain components can therefore be calculated as:

$$E_{ij} = \frac{1}{2} \left(\frac{\partial u_i}{\partial X_j} + \frac{\partial u_j}{\partial X_i} \right) + \frac{1}{2} \frac{\partial u_m}{\partial X_i} \frac{\partial u_m}{\partial X_j}, m = 1,2,3. \quad (21)$$

To formulate the mechanical behavior of the material under external forces, the relationship between the stress tensor and the strain tensor should be described. In this regard, the internal traction vector \mathbf{t} of a force \mathbf{F} that acts on a plane is defined as:

$$\mathbf{t} = \frac{d\mathbf{F}}{dA} \quad (22)$$

where dA is a very small differential area on the plane where the force $d\mathbf{F}$ is applied. The vector \mathbf{t} can be expressed in terms of components of true (Cauchy) stress. For each component of \mathbf{t} normal to each face of the infinitesimal cube ($\mathbf{t}_{N_1}, \mathbf{t}_{N_2}, \mathbf{t}_{N_3}$) (Figure 1-13), the corresponding stress components are used:

$$\begin{cases} \mathbf{t}_{N_1} = \sigma_{11}\mathbf{N}_1 + \sigma_{12}\mathbf{N}_2 + \sigma_{13}\mathbf{N}_3 \\ \mathbf{t}_{N_2} = \sigma_{21}\mathbf{N}_1 + \sigma_{22}\mathbf{N}_2 + \sigma_{23}\mathbf{N}_3, \\ \mathbf{t}_{N_3} = \sigma_{31}\mathbf{N}_1 + \sigma_{32}\mathbf{N}_2 + \sigma_{33}\mathbf{N}_3 \end{cases} \quad (23)$$

Or in a compact form:

$$\mathbf{t}_{N_i} = \sigma_{ij}\mathbf{N}_j, i \in \{1,2,3\} \text{ and } j \in \{1,2,3\}. \quad (24)$$

In these equations, \mathbf{N}_j is the unit vector normal to the corresponding face of the infinitesimal cube (Figure 1-13).

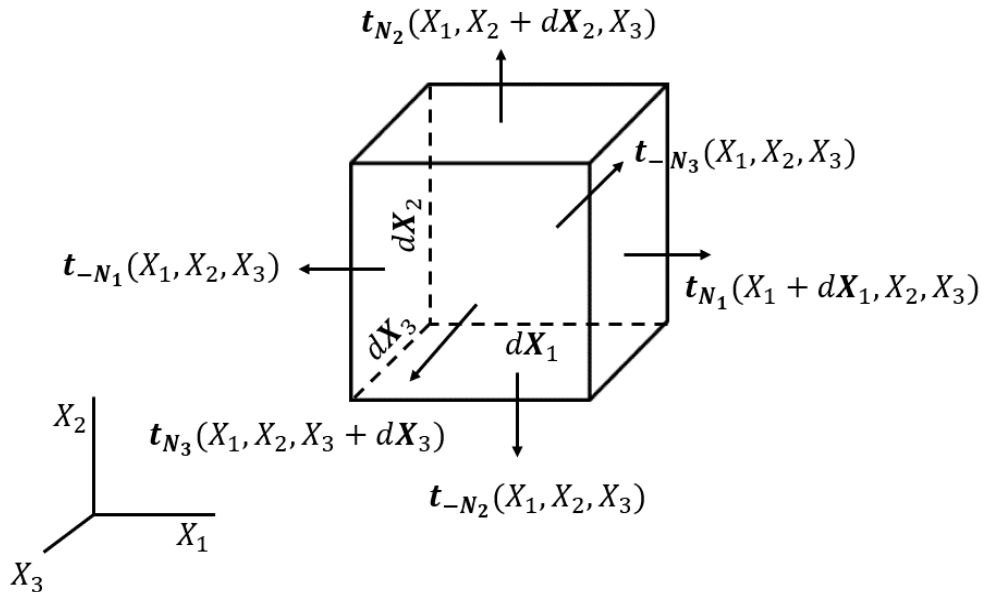


Figure 1-13. The infinitesimal cube and the unit vectors normal to its surfaces, used for calculating internal traction.

Having the relationship between the internal traction vector for each particle (cube as in Figure 1-13) and the components of the Cauchy stress, we can write the equilibrium of force for the cube, that is the infinitesimal volume of the continuum material. Newton's second law must be satisfied for the infinitesimal cube, hence the following equation shows the equilibrium per unit volume of the cube:

$$\frac{\partial \mathbf{t}_{N_1}}{\partial x_1} + \frac{\partial \mathbf{t}_{N_2}}{\partial x_2} + \frac{\partial \mathbf{t}_{N_3}}{\partial x_3} + \rho \mathbf{B} = \rho \mathbf{a}, \quad (25)$$

$$\text{or : } \frac{\partial \mathbf{t}_{N_j}}{\partial x_j} + \rho B_j N_j = \rho a_j N_j, \quad j \in \{1,2,3\}, \quad (26)$$

Where \mathbf{B} is the body force per unit mass through the continuum. We use the Cauchy stress representation of \mathbf{t}_{N_j} , and we can write the equilibrium equation as follows:

$$\frac{\partial \sigma_{ij}}{\partial x_j} + \rho B_i = \rho a_i, \quad i \in \{1,2,3\} \text{ and } j \in \{1,2,3\}. \quad (27)$$

The above equation in the tensor form is:

$$\text{div } \boldsymbol{\sigma} + \rho \mathbf{B} = \rho \mathbf{a}. \quad (28)$$

The above equation is called the Cauchy's equation of motion that describes the deformation of the continuum body.

To find the mechanical behavior of an elastic material under external forces, we need information about the mechanical properties of the material, e.g. its stiffness and incompressibility that define its active deformation pattern due to specific loading conditions. Typically, the intrinsic mechanical behavior of the material is represented by a relationship between the generated stresses and the strains in the continuum body. This relationship is known as a constitutive law.

1.8.1 Linear Elasticity

The constitutive law for linear elastic materials is given by the Hook's law. Hook's law defines the relationship between the components of Cauchy stress (σ_{ij}), and the components of the strain tensor (ε_{kl}) for continuum material particles as:

$$\sigma_{ij} = C_{ijkl} \varepsilon_{kl}, \quad (29)$$

where C is known as the elasticity tensor and is of order 4. The elasticity tensor has $3^4 = 81$ entries, however, 21 of which are enough to fully characterize the elastic behavior of the material. When the material is isotropic and linear elastic, Hook's law is simplified to (in tensor form):

$$\boldsymbol{\sigma} = \lambda \varepsilon_{kk} \mathbf{I} + 2\mu \boldsymbol{\varepsilon}, \quad (30)$$

where λ and μ are Lamé's constants. The Lamé's constants are defined in terms of the stiffness (Young's modulus, E) and the incompressibility (Poisson's ratio, ν):

$$\lambda = \frac{\nu E}{(1 + \nu)(1 - 2\nu)}, \quad \mu = \frac{E}{2(1 + \nu)}. \quad (31)$$

Equations 29 and 30 can fully describe the mechanical behavior of an isotropic linear elastic material under external forces.

1.8.2 Hyperelasticity

Many of the materials do not exhibit linear elastic response under external loading conditions. The nonlinear behavior of materials can be attributed to either or a combination of two mechanisms: intrinsic nonlinearity, and geometric nonlinearity. Hyperelasticity is used to explain the mechanical behavior of materials involving both mechanisms. Intrinsic nonlinearity, as the name suggests, is due to intrinsic mechanical properties that are defined by the properties of the material constituents. Materials with intrinsic nonlinearity are described by a nonlinear relationship between the Cauchy stresses and the strain tensor components under loading. Geometric nonlinearity arises from the change in the mechanical response caused by a force equilibrium alteration resulting from change in the material geometry. The change in the material geometry typically occurs when the material undergoes large deformations (strains $> 5\%$) due to external loading, and results in a redistribution of forces within the material.

In hyperelastic materials, the mechanical behavior is characterized in terms of a *strain energy function*, because hyperelastic materials may store deformation work as elastic energy (strain energy). The strain energy function is therefore defined in the deformation

gradients (F) space, as energy per unit volume. The constitutive law of the material is derived according to the strain energy function, and for that purpose we can write the equation that relates the Cauchy stress tensor ($\boldsymbol{\sigma}$) to the density energy function ($U(\mathbf{F})$) and the deformation gradient tensor (\mathbf{F}) and its determinant (J):

$$\boldsymbol{\sigma} = J^{-1} \mathbf{F} \frac{dU(\mathbf{F})}{d\mathbf{F}}. \quad (32)$$

When the hyperelastic material is isotropic, the determinant of deformation gradient is one, and the above equation in this case becomes:

$$\boldsymbol{\sigma} = -p\mathbf{I} + \mathbf{F} \frac{dU(\mathbf{F})}{d\mathbf{F}}, \quad (33)$$

where p is an indeterminate Lagrange multiplier. The constitutive law for the isotropic hyperelastic materials can be derived from the above equation in terms of the strain energy function as:

$$\boldsymbol{\sigma} = 2J^{-1} \left[I_3 \frac{\partial U}{\partial I_3} \mathbf{I} + \left(\frac{\partial U}{\partial I_1} + I_1 \frac{\partial U}{\partial I_2} \right) \mathbf{B} - \frac{\partial U}{\partial I_2} \mathbf{B}^2 \right], \quad (34)$$

where \mathbf{B} (not to be confused with B in Eq. 25) is the left Cauchy-Green deformation tensor, defined in terms of the deformation gradient tensor as:

$$\mathbf{B} = \mathbf{F}\mathbf{F}^T. \quad (35)$$

The strain energy function (U) is a function of I_1 , I_2 , and I_3 , i.e. the strain invariants of the Cauchy-Green deformation tensors:

$$I_1 = \text{tr}(\mathbf{B}) = \lambda_1^2 + \lambda_2^2 + \lambda_3^2 \quad (36)$$

$$I_2 = 0.5 \left[(\text{tr}(\mathbf{B}))^2 - \text{tr}(\mathbf{B}^2) \right] = \lambda_1^2 \lambda_2^2 + \lambda_1^2 \lambda_3^2 + \lambda_2^2 \lambda_3^2 \quad (37)$$

$$I_3 = \det(\mathbf{B}) = J^2 = \lambda_1^2 \lambda_2^2 \lambda_3^2. \quad (38)$$

In the above equations, λ_i , $i \in \{1,2,3\}$, are the principal stretches.

Using Eq. 34, the constitutive law for a material can be derived for a given strain energy function. There are several different hyperelastic models that are represented by different strain energy functions. These different hyperelastic models are used to characterize the various mechanical behaviors of nonlinear elastic materials. In ABAQUS (the finite element solver that we used in this project), several hyperelastic forms are implemented, including: Arruda-Boyce, Marlow, Mooney-Rivlin, Neo-Hookean, Ogden, polynomial, reduced polynomial, Van der Waals, and Yeoh. The appropriate strain energy form for a material must be chosen based on mechanical test data. In this project, the Yeoh hyperelastic form was chosen to model the mechanical behavior of the lung tissue under deformation. The Yeoh strain energy function is described as:

$$U = \sum_{i=1}^3 \left(C_{i0} (I_1 - 3)^i + \frac{1}{D_i} (J - 1)^{2i} \right), \quad (39)$$

where C_{10} , C_{20} , and C_{30} are the hyperelastic parameters and D_1 , D_2 , and D_3 are the incompressibility coefficients. From the strain energy function and Eqs. 34 to 38, the stress-strain relationship can be obtained for the Yeoh hyperelastic form.

1.9 «Inverse Problem»

Using the complete description of a system from the governing physical theories, we can make predictions of the outcome of measurements. Predicting the measurement results of a system is known as the *forward problem*. On the other hand, using the results of measurements of a system to infer the values of parameters that describe the system is referred to as *inverse problem*. Unlike the forward problem, the inverse problem does not typically have a unique solution. In this work, to develop the biomechanical model of the lung based on the information from 4DCT, we have designed and implemented an inverse problem formulation. The parameters of the lung biomechanical model (the forward model) are found based on the information from 4DCT (results of measurements). For more detailed information on the inverse problem, see Section 2.2.3.

1.10 «Research Objectives»

The work presented in this thesis is mainly focused on two objectives:

1. Development of an accurate lung biomechanical model for tumor motion and deformation estimation by incorporating pathology-induced heterogeneity.
2. Development of a 4DCT-based ventilation imaging technique using a biomechanical model-based image registration and an accurate air segmentation algorithm, as well as validation of the proposed ventilation imaging technique using hyperpolarized ^3He MR.

1.11 «Thesis Outline»

This thesis is organized to include four chapters. The current chapter is dedicated to introduction and background, while the following two chapters describe the details of the work towards achieving the two main objectives mentioned in the above section, followed by the final chapter which is dedicated to summary and concluding remarks.

1.11.1 Chapter 2: A Patient-Specific Heterogeneous Biomechanical Model of the Lung for Accurate Tumor Motion Estimation

In this chapter, we describe details of the work towards achieving the first objective of the thesis. A patient-specific lung biomechanical model is developed from 4DCT scans. This lung biomechanical model is patho-physiologically realistic as it incorporates the heterogeneity in the lung tissue mechanics caused by co-existing chronic obstructive pulmonary disease (COPD). Advanced image processing methodologies such as semi-automated segmentation of the lung images, free-form deformation image registration algorithm, semi-automated boundary conditions extraction, and COPD phenotypes quantification algorithm were designed and implemented and/or employed to extract the information from 4DCT scans, required to build the biomechanical model. An inverse problem formulation was designed and employed to obtain the parameters of the biomechanical model, e.g. the coefficients determining the amplitude of the pressure that inflates the lungs, and the mechanical properties of the lung tissue affected by COPD phenotypes. The lung biomechanical model is used to estimate the motion and

deformation of the tumor. The simulation results were compared against the actual location and shape of the tumor extracted from 4DCT using measures of similarity and distance. The high accuracy of the model for tumor motion and deformation estimation indicates successful achievement of the first objective of the thesis.

1.11.2 Chapter 3: 4DCT Ventilation Imaging Using Biomechanical Model-based Deformable Registration

In this chapter, we explain the details of the work towards achieving the second objective of the thesis. We developed a 4DCT-based ventilation imaging technique using a novel method that utilizes a biomechanical model-based DIR along with an accurate air segmentation algorithm. 4DCT scans of patients diagnosed with NSCLC and planned for RT were used to build patient-specific biomechanical models of the lungs. In this model, the lung geometry used for finite element (FE) meshing was acquired from segmenting the CT volume at end-exhalation. Loading was defined in terms of the transpulmonary pressure expanding the lungs. Boundary conditions consisted of the diaphragm motion and anatomical fixed points for each patient. The pressure amplitude and mechanical properties of various tissue volumes of the lung were found through an optimization algorithm designed to maximize the accuracy of the biomechanical model. The biomechanical model was used to deformably register the end-exhale scans to the end-inhale ones. The biomechanical model-based DIR tracks air motion in the lung. The air segmentation algorithm, previously developed in our lab and enhanced in this work, found subject-specific thresholds for the inhalation and exhalation CT scans. This air segmentation algorithm also accounts for the partial volume effect, hence providing accurate estimations of the air volume inside the voxels. Having the air motion from DIR, and the air volume in each voxel, we can calculate the ventilation. To have a more accurate estimate of ventilation, we also took into account the regional volume expansion due to the inflow of air. We used the change in the volume of the mesh elements during finite element analysis to obtain the volume expansion at voxel level. The final 4DCT ventilation images were qualitatively and quantitatively compared against ^3He MR images for validation.

1.11.3 Chapter 4: Discussion and Conclusion

In the final chapter, we summarize the findings of the thesis, and discuss the limitations of the proposed algorithms. We also discuss possible future directions and suggestions for further studies. This section lastly concludes this dissertation.

«References»

1. CCSAC. Canadian Cancer Statistics: A 2018 special report on cancer incidence by stage. Can Cancer Soc. 2018;
2. Abdul Ghani MNH, Ng WL. Management of respiratory motion for lung radiotherapy: a review. J Xiangya Med. 2018;
3. Keall PJ, Mageras GS, Balter JM, Emery RS, Forster KM, Jiang SB, et al. The management of respiratory motion in radiation oncology report of AAPM Task Group 76. Medical Physics. 2006.
4. Yaremko BP, Guerrero TM, Noyola-Martinez J, Guerra R, Lege DG, Nguyen LT, et al. Reduction of Normal Lung Irradiation in Locally Advanced Non-Small-Cell Lung Cancer Patients, Using Ventilation Images for Functional Avoidance. Int J Radiat Oncol Biol Phys. 2007;
5. Yamamoto T, Kabus S, Von Berg J, Lorenz C, Keall PJ. Impact of four-dimensional computed tomography pulmonary ventilation imaging-based functional avoidance for lung cancer radiotherapy. Int J Radiat Oncol Biol Phys. 2011;
6. Canadian Cancer Statistics Advisory Committee. Canadian Cancer Statistics Special topic: Pancreatic cancer. Can Cancer Stat. 2017;
7. World Health Organization. Latest global cancer data: Cancer burden rises to 18.1 million new cases and 9.6 million deaths in 2018. Int Agency Res cancer. 2018;

8. Zappa C, Mousa SA. Non-small cell lung cancer: current treatment and future advances. *Transl Lung Cancer Res.* 2016;
9. Dela Cruz CS, Tanoue LT, Matthay RA. Lung Cancer: Epidemiology, Etiology, and Prevention. *Clinics in Chest Medicine.* 2011.
10. Report from the Canadian Chronic Disease Surveillance System: Asthma and Chronic Obstructive Pulmonary Disease (COPD) in Canada, 2018. 2018.
11. Durham AL, Adcock IM. The relationship between COPD and lung cancer. *Lung Cancer.* 2015.
12. Barnes PJ, Shapiro SD, Pauwels RA. Chronic obstructive pulmonary disease: Molecular and cellular mechanisms. *European Respiratory Journal.* 2003.
13. Galbán CJ, Han MK, Boes JL, Chughtai KA, Meyer CR, Johnson TD, et al. Computed tomography-based biomarker provides unique signature for diagnosis of COPD phenotypes and disease progression. *Nat Med.* 2012;
14. Celli BR, MacNee W, Agusti A, Anzueto A, Berg B, Buist AS, et al. Standards for the diagnosis and treatment of patients with COPD: A summary of the ATS/ERS position paper. *European Respiratory Journal.* 2004.
15. Usmani OS, Barnes PJ. Assessing and treating small airways disease in asthma and chronic obstructive pulmonary disease. *Ann Med.* 2012;
16. Shaw RJ, Djukanovic R, Tashkin DP, Millar AB, Du Bois RM, Corris PA. The role of small airways in lung disease. *Respiratory Medicine.* 2002.
17. Washko GR. The role and potential of imaging in COPD. *Medical Clinics of North America.* 2012.
18. Washko GR. Diagnostic imaging in COPD. *Seminars in Respiratory and Critical Care Medicine.* 2010.
19. Wang W, Dou S, Dong W, Xie M, Cui L, Zheng C, et al. Impact of COPD on

- prognosis of lung cancer: From a perspective on disease heterogeneity. *Int J COPD*. 2018;
20. Raviv S, Hawkins KA, DeCamp MM, Kalhan R. Lung cancer in chronic obstructive pulmonary disease: Enhancing surgical options and outcomes. *American Journal of Respiratory and Critical Care Medicine*. 2011.
 21. Wang W, Xie M, Dou S, Cui L, Zheng C, Xiao W. The link between chronic obstructive pulmonary disease phenotypes and histological subtypes of lung cancer: A case–control study. *Int J COPD*. 2018;
 22. Martínez-García MÁ, Soler-Catalunã JJ, Sanz YD, Serra PC, Lerma MA, Vicente JB, et al. Factors associated with bronchiectasis in patients with COPD. *Chest*. 2011;
 23. Postmus PE, Kerr KM, Oudkerk M, Senan S, Waller DA, Vansteenkiste J, et al. Early and locally advanced non-small-cell lung cancer (NSCLC): ESMO Clinical Practice Guidelines for diagnosis, treatment and follow-up. *Ann Oncol*. 2017;
 24. Novello S, Barlesi F, Califano R, Cufer T, Ekman S, Levra MG, et al. Metastatic non-small-cell lung cancer: ESMO Clinical Practice Guidelines for diagnosis, treatment and follow-up. *Ann Oncol*. 2016;
 25. Hoover DA, Capaldi DPI, Sheikh K, Palma DA, Rodrigues GB, Dar AR, et al. Functional lung avoidance for individualized radiotherapy (FLAIR): Study protocol for a randomized, double-blind clinical trial. *BMC Cancer*. 2014;
 26. Konski A, Feigenberg S, Chow E. Palliative radiation therapy. *Semin Oncol* [Internet]. 2005 Apr 1 [cited 2019 Aug 14];32(2):156–64. Available from: <https://www.sciencedirect.com/science/article/abs/pii/S0093775404005706>
 27. Hoskin PJ. Radiotherapy in practice: external beam therapy. *Radiotherapy in practice*. 2012.
 28. Lyman JT. Complication Probability as Assessed from Dose-Volume Histograms.

- Radiat Res Suppl. 2006;
29. Keall P. 4-Dimensional Computed Tomography Imaging and Treatment Planning. Semin Radiat Oncol. 2004;
 30. Benedict SH, Yenice KM, Followill D, Galvin JM, Hinson W, Kavanagh B, et al. Stereotactic body radiation therapy: The report of AAPM Task Group 101. Medical Physics. 2010.
 31. Schlegel W, Bortfeld T, Grosu A-L, Pan T, Luo D. New Technologies in Radiation Oncology. J Nucl Med. 2008;
 32. Widder J, Postmus D, Ubbels JF, Wiegman EM, Langendijk JA. Survival and quality of life after stereotactic or 3D-conformal radiotherapy for inoperable early-stage lung cancer. Int J Radiat Oncol Biol Phys. 2011;
 33. Gaya A, Mahadevan A. Stereotactic body radiotherapy: A Practical Guide. Seminars in Oncology. 2014.
 34. Spirou S V., Chui CS. A gradient inverse planning algorithm with dose-volume constraints. Medical Physics. 1998.
 35. Otto K. Volumetric modulated arc therapy: IMRT in a single gantry arc. Med Phys. 2008;
 36. Li G, Citrin D, Camphausen K, Mueller B, Burman C, Mychalczak B, et al. Advances in 4D medical imaging and 4D radiation therapy. Technology in Cancer Research and Treatment. 2008.
 37. Keall PJ, Kini VR, Vedam SS, Mohan R. Potential radiotherapy improvements with respiratory gating. Australas Phys Eng Sci Med. 2002;
 38. Shioyama Y, Jang SY, Liu HH, Guerrero T, Wang X, Gayed IW, et al. Preserving Functional Lung Using Perfusion Imaging and Intensity-Modulated Radiation Therapy for Advanced-Stage Non-Small Cell Lung Cancer. Int J Radiat Oncol

Biol Phys. 2007;

39. Lavrenkov K, Christian JA, Partridge M, Niotsikou E, Cook G, Parker M, et al. A potential to reduce pulmonary toxicity: The use of perfusion SPECT with IMRT for functional lung avoidance in radiotherapy of non-small cell lung cancer. *Radiother Oncol.* 2007;83(2):156–62.
40. Lax I, Blomgren H, Näslund I, Svanström R. Stereotactic radiotherapy of malignancies in the abdomen: Methodological aspects. *Acta Oncol (Madr).* 1994;
41. Glide-Hurst CK, Chetty IJ. Improving radiotherapy planning, delivery accuracy, and normal tissue sparing using cutting edge technologies. *Journal of Thoracic Disease.* 2014.
42. Yoganathan S, Maria Das K, Agarwal A, Kumar S. Magnitude, impact, and management of respiration-induced target motion in radiotherapy treatment: A comprehensive review. *J Med Phys.* 2017;
43. Stevens CW, Munden RF, Forster KM, Kelly JF, Liao Z, Starkschall G, et al. Respiratory-driven lung tumor motion is independent of tumor size, tumor location, and pulmonary function. *Int J Radiat Oncol Biol Phys.* 2001;
44. Shimizu S, Shirato H, Ogura S, Akita-Dosaka H, Kitamura K, Nishioka T, et al. Detection of lung tumor movement in real-time tumor-tracking radiotherapy. *Int J Radiat Oncol Biol Phys.* 2001;
45. Plathow C, Ley S, Fink C, Puderbach M, Hosch W, Schmähl A, et al. Analysis of intrathoracic tumor mobility during whole breathing cycle by dynamic MRI. *Int J Radiat Oncol Biol Phys.* 2004;
46. Seppenwoolde Y, Shirato H, Kitamura K, Shimizu S, Van Herk M, Lebesque J V., et al. Precise and real-time measurement of 3D tumor motion in lung due to breathing and heartbeat, measured during radiotherapy. *Int J Radiat Oncol Biol Phys.* 2002;

47. Davies SC, Hill AL, Holmes RB, Halliwell M, Jackson PC. Ultrasound quantitation of respiratory organ motion in the upper abdomen. *Br J Radiol.* 1994;
48. Giraud P, De Rycke Y, Dubray B, Helfre S, Voican D, Guo L, et al. Conformal radiotherapy (CRT) planning for lung cancer: Analysis of intrathoracic organ motion during extreme phases of breathing. *Int J Radiat Oncol Biol Phys.* 2001;
49. Korreman SS. Image-guided radiotherapy and motion management in lung cancer. *British Journal of Radiology.* 2015.
50. Korreman SS, Juhler-Nøttrup T, Boyer AL. Respiratory gated beam delivery cannot facilitate margin reduction, unless combined with respiratory correlated image guidance. *Radiother Oncol.* 2008;
51. Chang JY, Dong L, Liu H, Starkschall G, Balter P, Mohan R, et al. Image-guided radiation therapy for non-small cell lung cancer. *J Thorac Oncol.* 2008;
52. Borst GR, Sonke JJ, Den Hollander S, Betgen A, Remeijer P, Van Giersbergen A, et al. Clinical results of image-guided deep inspiration breath hold breast irradiation. *Int J Radiat Oncol Biol Phys.* 2010;
53. Bouilhol G, Ayadi M, Rit S, Thengumpallil S, Schaerer J, Vandemeulebroucke J, et al. Is abdominal compression useful in lung stereotactic body radiation therapy? A 4DCT and dosimetric lobe-dependent study. *Phys Medica.* 2013;
54. Boda-Heggemann J, Knopf AC, Simeonova-Chergou A, Wertz H, Stieler F, Jahnke A, et al. Deep Inspiration Breath Hold - Based Radiation Therapy: A Clinical Review. *International Journal of Radiation Oncology Biology Physics.* 2016.
55. Murphy MJ. Adaptive motion compensation in radiotherapy. *Adaptive Motion Compensation in Radiotherapy.* 2011.
56. Ge Y, O'Brien RT, Shieh CC, Booth JT, Keall PJ. Toward the development of intrafraction tumor deformation tracking using a dynamic multi-leaf collimator.

- Med Phys. 2014;
57. Kilby W, Dooley JR, Kuduvalli G, Sayeh S, Maurer CR. The CyberKnife® robotic radiosurgery system in 2010. *Technology in Cancer Research and Treatment*. 2010.
 58. Shah AP, Kupelian PA, Waghorn BJ, Willoughby TR, Rineer JM, Mañon RR, et al. Real-time tumor tracking in the lung using an electromagnetic tracking system. *Int J Radiat Oncol Biol Phys*. 2013;
 59. Lu XQ, Shanmugham LN, Mahadevan A, Nedeia E, Stevenson MA, Kaplan I, et al. Organ Deformation and Dose Coverage in Robotic Respiratory-Tracking Radiotherapy. *Int J Radiat Oncol Biol Phys*. 2008;
 60. Jurkovic IA, Papanikolaou N, Stathakis S, Li Y, Patel A, Vincent J, et al. Assessment of Lung Tumour Motion and Volume Size Dependencies Using Various Evaluation Measures. *J Med Imaging Radiat Sci*. 2016;
 61. Patel A, Khalsa B, Lord B, Sandrasegaran K, Lall C. Planting the seeds of success: CT-guided gold seed fiducial marker placement to guide robotic radiosurgery. *Journal of Medical Imaging and Radiation Oncology*. 2013.
 62. Trumm CG, Häußler SM, Muacevic A, Stahl R, Stintzing S, Paprottka PM, et al. CT fluoroscopy-guided percutaneous fiducial marker placement for cyberknife stereotactic radiosurgery: Technical results and complications in 222 consecutive procedures. *J Vasc Interv Radiol*. 2014;
 63. Karami, E., Gaede, S., Lee, T. Y., Samani, A. A machine learning approach for biomechanics-based tracking of lung tumor during external beam radiation therapy. *Medical Imaging 2018: Image-Guided Procedures, Robotic Interventions, and Modeling* (Vol. 10576, p. 105761C).
 64. li R, Jia X, Lewis J, gu X, Folkerts M, Men C, et al. WE-C-204B-05: Real-Time Volumetric Image Reconstruction and 3D Tumor Localization Based on a Single X-Ray Projection Image during Lung Cancer Radiotherapy. In: *Medical Physics*.

2010.

65. Li R, Lewis JH, Jia X, Gu X, Folkerts M, Men C, et al. 3D tumor localization through real-time volumetric x-ray imaging for lung cancer radiotherapy. *Med Phys*. 2011;
66. Wang J, gu X. TH-C-103-02: Simultaneous Motion Estimation and Image Reconstruction (SMEIR) for 4D Cone-Beam CT. In: *Medical Physics*. 2013.
67. Al-Mayah A, Moseley J, Velec M, Hunter S, Brock K. Deformable image registration of heterogeneous human lung incorporating the bronchial tree. *Med Phys*. 2010;
68. Al-Mayah A, Moseley J, Velec M, Brock K. Effect of friction and material compressibility on deformable modeling of human lung. In: *Lecture Notes in Computer Science (including subseries Lecture Notes in Artificial Intelligence and Lecture Notes in Bioinformatics)*. 2008.
69. Shirzadi Z, Sadeghi-Naini A, Samani A. Toward in vivo lung's tissue incompressibility characterization for tumor motion modeling in radiation therapy. *Med Phys*. 2013;40(5):051902.
70. Al-Mayah A, Moseley J, Velec M, Brock KK. Sliding characteristic and material compressibility of human lung: Parametric study and verification. *Med Phys*. 2009;
71. Han L, Dong H, McClelland JR, Han L, Hawkes DJ, Barratt DC. A hybrid patient-specific biomechanical model based image registration method for the motion estimation of lungs. *Med Image Anal*. 2017;
72. Lee HJ, Zeng J, Vesselle HJ, Patel SA, Rengan R, Bowen SR. Correlation of Functional Lung Heterogeneity and Dosimetry to Radiation Pneumonitis using Perfusion SPECT/CT and FDG PET/CT Imaging. *Int J Radiat Oncol [Internet]*. 2018 Nov 15 [cited 2019 Jun 12];102(4):1255–64. Available from: <https://www.sciencedirect.com/science/article/pii/S0360301618309039>

73. Wellman TJ, Winkler T, Costa EL V., Musch G, Harris RS, Venegas JG, et al. Measurement of Regional Specific Lung Volume Change Using Respiratory-Gated PET of Inhaled ¹³N-Nitrogen. *J Nucl Med.* 2010;
74. Siva S, Thomas R, Callahan J, Hardcastle N, Pham D, Kron T, et al. High-resolution pulmonary ventilation and perfusion PET/CT allows for functionally adapted intensity modulated radiotherapy in lung cancer. *Radiother Oncol.* 2015;
75. Mugler JP, Altes TA. Hyperpolarized ¹²⁹Xe MRI of the human lung. *Journal of Magnetic Resonance Imaging.* 2013.
76. Fain SB, Korosec FR, Holmes JH, O'halloran R, Sorkness RL, Grist TM. Functional Lung Imaging Using Hyperpolarized Gas MRI. *J Magn Reson Imaging* [Internet]. 2007 [cited 2019 Jun 6];25:910–23. Available from: www.interscience.wiley.com.
77. Möller HE, Chen XJ, Saam B, Hagspiel KD, Johnson GA, Altes TA, et al. MRI of the Lungs Using Hyperpolarized Noble Gases. *Magn Reson Med* [Internet]. 2002 [cited 2019 Jun 17];47:1029–51. Available from: www.interscience.wiley.com
78. Ding K, Cao K, Fuld MK, Du K, Christensen GE, Hoffman EA, et al. Comparison of image registration based measures of regional lung ventilation from dynamic spiral CT with Xe-CT. 2012 Jul 27 [cited 2019 Jun 6];39(8). Available from: <http://dx.doi.org/10.1118/1.4736808>
79. Vinogradskiy Y, Rusthoven CG, Schubert L, Jones B, Faught A, Castillo R, et al. Interim Analysis of a Two-Institution, Prospective Clinical Trial of 4DCT-Ventilation-based Functional Avoidance Radiation Therapy. *Int J Radiat Oncol* [Internet]. 2018 Nov 15 [cited 2019 Jun 7];102(4):1357–65. Available from: <https://www.sciencedirect.com/science/article/pii/S0360301618316390>
80. Bradley J, Graham M V., Winter K, Purdy JA, Komaki R, Roa WH, et al. Toxicity and outcome results of RTOG 9311: A phase I-II dose-escalation study using three-dimensional conformal radiotherapy in patients with inoperable non-small-

- cell lung carcinoma. *Int J Radiat Oncol Biol Phys.* 2005;
81. Socinski MA, Morris DE, Halle JS, Moore DT, Hensing TA, Limentani SA, et al. Induction and concurrent chemotherapy with high-dose thoracic conformal radiation therapy in unresectable stage IIIA and IIIB non-small-cell lung cancer: A dose-escalation phase I trial. *J Clin Oncol.* 2004;
 82. Yamamoto T, Kabus S, Lorenz C, Mitra E, Hong JC, Chung M, et al. Pulmonary ventilation imaging based on 4-dimensional computed tomography: Comparison with pulmonary function tests and SPECT ventilation images. *Int J Radiat Oncol Biol Phys.* 2014;
 83. Siva S, Callahan J, Kron T, Martin OA, MacManus MP, Ball DL, et al. A prospective observational study of Gallium-68 ventilation and perfusion PET/CT during and after radiotherapy in patients with non-small cell lung cancer. *BMC Cancer.* 2014;
 84. Mathew L, Wheatley A, Castillo R, Castillo E, Rodrigues G, Guerrero T, et al. Hyperpolarized ³He Magnetic Resonance Imaging. Comparison with Four-dimensional X-ray Computed Tomography Imaging in Lung Cancer. *Acad Radiol.* 2012;
 85. Tahir BA, Hughes PJC, Robinson SD, Marshall H, Stewart NJ, Norquay G, et al. Spatial Comparison of CT-Based Surrogates of Lung Ventilation With Hyperpolarized Helium-3 and Xenon-129 Gas MRI in Patients Undergoing Radiation Therapy. *Int J Radiat Oncol* [Internet]. 2018 Nov [cited 2019 Jun 7];102(4):1276–86. Available from: <https://linkinghub.elsevier.com/retrieve/pii/S0360301618307557>
 86. Rossi A, Attinà D, Borgonovi A, Buia F, De Luca F, Guidalotti PL, et al. Evaluation of mosaic pattern areas in HRCT with Min-IP reconstructions in patients with pulmonary hypertension: Could this evaluation replace lung perfusion scintigraphy? *Eur J Radiol.* 2012;

87. Hegi-Johnson F, Keall P, Barber J, Bui C, Kipritidis J. Evaluating the accuracy of 4D- CT ventilation imaging: First comparison with Technegas SPECT ventilation. *Med Phys* [Internet]. 2017 Aug 16 [cited 2019 Jun 7];44(8):4045–55. Available from: <https://onlinelibrary.wiley.com/doi/abs/10.1002/mp.12317>
88. Kipritidis J, Tahir BA, Cazoulat G, Hofman MS, Siva S, Callahan J, et al. The VAMPIRE challenge: A multi-institutional validation study of CT ventilation imaging. *Med Phys* [Internet]. 2019 Mar 1 [cited 2019 Jun 26];46(3):1198–217. Available from: <http://doi.wiley.com/10.1002/mp.13346>
89. Simon BA. Non-invasive imaging of regional lung function using X-ray computed tomography. *Journal of Clinical Monitoring and Computing*. 2000.
90. Kipritidis J, Hofman MS, Siva S, Callahan J, Le Roux PY, Woodruff HC, et al. Estimating lung ventilation directly from 4D CT Hounsfield unit values. *Med Phys*. 2016;
91. Reinhardt JM, Ding K, Cao K, Christensen GE, Hoffman EA, Bodas S V. Registration-based estimates of local lung tissue expansion compared to xenon CT measures of specific ventilation. *Med Image Anal*. 2008;
92. Reinhardt JM, Christensen GE, Hoffman EA, Ding K, Cao K. Registration-derived estimates of local lung expansion as surrogates for regional ventilation. In: *Lecture Notes in Computer Science (including subseries Lecture Notes in Artificial Intelligence and Lecture Notes in Bioinformatics)*. 2007.
93. Adams R, Bischof L. Seeded Region Growing. *IEEE Trans Pattern Anal Mach Intell*. 1994;
94. Zitová B, Flusser J. Image registration methods: A survey. *Image Vis Comput*. 2003;
95. Maintz JBA, Viergever MA. A survey of medical image registration. *Med Image Anal*. 1998;

96. Castillo E, Castillo R, Martinez J, Shenoy M, Guerrero T. Four-dimensional deformable image registration using trajectory modeling. *Phys Med Biol.* 2010;
97. Insight Consortium. ITK - Segmentation & Registration Toolkit. <http://www.itk.org/>. 2012.
98. Irgens F. Continuum mechanics. *Continuum Mechanics.* 2008.
99. Falk S. and Williams C., *Lung Cancer*, OUP Oxford, 2009
100. Mohan R, Bortfeld T. The potential and limitations of IMRT: A physicist's point of view. In: *Image-Guided IMRT.* 2006.

Chapter 2

2 « A Patient-Specific Heterogeneous Biomechanical Model of the Lung for Accurate Tumor Motion Estimation »

Currently, one of the main components of lung cancer treatment is radiation therapy (RT) which suffers from inaccuracies caused by the complex intrafraction respiratory motions. One potential solution towards addressing this challenge is to develop a lung biomechanical model capable of predicting the tumor's motion/deformation. Chronic obstructive pulmonary disease (COPD) commonly coexists with lung cancer and is associated with extensive heterogeneity in the lung parenchyma; however, current methods lack this key component. In this work, we have developed an accurate lung biomechanical model that accounts for COPD-induced heterogeneities in the lung structure. Four-dimensional computed tomography (4DCT) images were used to build a patient-specific finite element (FE) model, and to identify inhomogeneity inside the model. Mechanical properties of pathological volumes inside the lung, and the maximum amplitude of the pressure driving the respiratory motion are determined through an optimization algorithm that aims at maximizing the similarity between the actual and simulated tumor and lung volume images. Results obtained in this work suggest that the accuracy of the tumor motion estimation model increases considerably when incorporating the patho-physiological heterogeneity, compared to the homogeneous model counterpart.

2.1 « Introduction »

Lung cancer remains the most common type of cancer affecting men and women, both in terms of incidence and mortality (1). Concurrent chemotherapy and radiation therapy (RT) is the current standard treatment for inoperable non-small cell lung cancer (NSCLC)(1–3). Stereotactic body radiation therapy (SBRT) is a high-precision treatment technique for extracranial tumors that delivers potent doses of highly focused radiation beams during a single or a few radiation fractions (4). Recently developed advanced SBRT methods such as intensity modulated RT (IMRT) and volumetric modulated arc

therapy (VMAT), aim at increasing the tumor control probability (TCP), and lowering normal tissue complication probability (NTCP) by delivering a more accurate and highly conformal radiation dose (5,6). IMRT utilizes forward or inverse radiation treatment planning to determine and deliver the necessary dose distribution through the use of multileaf collimators (7). VMAT is a more advanced type of IMRT that decreases the delivery time by applying the dose in a single gantry arc movement and improves the dose conformity by using the full 360° range of gantry rotation (8,9). However, respiratory motion can cause inaccuracies in RT, resulting in higher probabilities of treatment complications such as irradiating normal tissue and undesirable dose distribution in the target tumor (7,10). Methods have been proposed to reduce such inaccuracies in RT, including: motion encompassing (11), breath-hold techniques (12), and gating the radiation beam with the breathing cycle (13,14). Each of these methods suffer from inherent limitations. In motion encompassing, the planning target volume is expanded to encompass the entire clinical target volume, resulting in a higher radiation dose delivery to normal tissue. Breath-hold methods are not usually well tolerated by lung cancer patients. Gated radiotherapy procedures are intrinsically associated with a conflict between the gating efficiency and gating window time, and longer radiation sessions. This problem is particularly of importance in IMRT systems where the treatment times are inevitably longer.

An alternative solution to improve the precision in radiation delivery is to synchronize the radiation beam with the tumor motion. Accordingly, strategies to account for respiratory motion that provide accurate information regarding real-time shape and location of the target tumor are in demand. Intensity-based deformable image registration (DIR) methods have been employed to estimate the deformation field of the lung and the respiratory tumor motion for dose calculation and treatment planning purposes (15–17). However, the application of DIR methods in real-time tumor tracking is limited to a few studies. Li R. et al. adapted deformable image registration (DIR) in conjunction with simultaneous x-ray imaging to estimate the lung tumor motion and deformation (18); however, the extra radiation dose imposed to the patient due to the x-ray imaging in these methods has raised some concerns (19). In addition, intensity-based DIR methods are solely based on four-dimensional computed tomography (4DCT) image data. These

methods do not take into account the physical properties or physiological mechanisms involved in breathing. Therefore, they are prone to errors associated with non-uniqueness of the resulting displacement field, and registration errors in areas with low image contrast. Handling the sliding motion of the lungs can also be challenging for motion estimation using intensity-based DIR methods (20,21).

Biomechanics-based computational modelling is another commonly used approach for respiratory tumor motion estimation. In contrast to DIR, biomechanics-based computational models encompass certain aspects of breathing dynamics, rendering this approach more robust and realistic (22–26). Patient-specific biomechanical models of the lung that use thoracic image data to extract the geometry and boundary conditions have previously been proposed (22,23,26,27). Several studies investigated the effects of model parameters including the mechanical properties (27–29), and boundary conditions (25) on modeling accuracy. Recently, hybrid hierarchical approaches have been proposed, in which finite element (FE)-based biomechanical models are used in conjunction with intensity-based DIR methods to predict deformation field of the lung in a respiratory cycle (21,30,31).

Biomechanical modeling of the lung is capable of respiratory tumor motion estimation without requiring simultaneous imaging during RT or implanting invasive fiducial markers inside the tumor. Our group recently proposed a hybrid motion model for real-time estimation of tumor location/geometry during respiration (32). The proposed method translates the chest surface motion data obtained by optical tracking markers to the tumor location/geometry, using the patient-specific biomechanical model of the lung and a predictive function. A realistic and accurate biomechanical model of the lung is, however, required in this method for real-time tracking of the tumor with a desired precision.

Tissue mechanical properties including tissue stiffness and incompressibility, are important features of a biomechanical model determining its behavior under loadings. The air volume inside the lungs varies significantly during a respiration cycle, therefore, changes in tissue incompressibility is expected. Shirzadi et al. were first to investigate the

variations of incompressibility of the lung throughout respiration (29). Their results demonstrated that accounting for variable incompressibility throughout respiration in a biomechanical model of the lung leads to higher accuracy of tumor motion estimation.

More than 65% of lung cancer patients also suffer from chronic obstructive pulmonary disease (COPD) (33,34). COPD is a heterogeneous disease, characterized by multiple phenotypes including small airways disease (SAD) and parenchymal destruction (emphysema) that cause changes in the structure and mechanical properties of the affected lung tissue (35–38). A characteristic manifestation of emphysema is the interactions that occur between the immune system and the mechanical properties of the lung parenchyma at the microstructure level. The former causes inflammatory responses resulting in tissue remodeling, and therefore alterations in the mechanical properties of the affected areas in the lung tissue under repeated breathing cycles. A biomechanical model that accounts for local changes in tissue material properties potentially results in a more realistic motion estimation. Although few studies have been conducted to measure mechanical parameters of the lung tissue (39,40) or to evaluate the effect of changes in tissue mechanical properties on the model accuracy (23,41,42), to our knowledge, a tumor motion/deformation estimation model accounting for pathology-induced local changes in mechanical properties of the lung has not been reported.

In this study, we propose a novel biomechanical model of the lung for respiratory tumor motion prediction that accounts for pathology-induced heterogeneities within the lung tissue. For this purpose, a patient-specific FE model of the lung was developed using 4DCT image data. The pathological regions pertaining to COPD phenotypes were quantified using the CT image data. Tissue sub-types pertaining to healthy and various pathological phenotypes were considered in the model. The CT image of the lung at end-exhalation (EE) was registered to the CT image of all phases of respiration (e.g. end-inhalation: EI) using the FE model by optimizing the parameters of loading and mechanical properties of the tissue sub-types.

The effect of incorporating pathology-induced heterogeneity on the model performance is investigated by comparing the accuracy of the tumor motion estimation of the

heterogeneous model with that of a homogeneous counterpart. Results of the similarity measures between the simulated and actual tumor volumes, as well as the average landmark error demonstrated that incorporating the pathology-induced tissue inhomogeneities can improve the model accuracy and reliability considerably.

2.2 « Materials and Methods »

2.2.1 Data Acquisition

This research was performed in accordance with the institutional research ethics board approval. 4DCT respiratory image sequences of 5 patients were acquired as part of the FLAIR trial (10). Patients were diagnosed with NSCLC and planned for IMRT or volumetric-modulated arc therapy (VMAT) using PINNACLE (v9.6) Radiation Therapy Planning System (Philips Medical Systems, Fitchburg, WI). Patients were scanned using a 16-slice Philips Brilliance Big Bore CT scanner (Philips Medical Systems) operating in helical mode. The scan parameters were: 120kVp and 400mAs/slice for tube potential and current, respectively. The intra-slice pixel size of the data varied from 1.0 mm \times 1.0 mm to 1.1 mm \times 1.1 mm, and the slice thickness was 3 mm for all scans.

The 4DCT images were sorted into 10 respiratory phases using the Real-time Position ManagementTM system. The phases were labeled as: 0%, 10%, 20%, etc. to 90%, with 0% denoting the EI phase and 50% denoting the EE phase. In this study, efforts were made to include patients with various tumor sizes and locations inside the lungs to explore the reliability and robustness of the biomechanical model. The average tumor size was 18.1 cm², ranging from 4.1 cm² to 61.9 cm². In addition, the extent of COPD-related phenotypes including gas trapping and airway wall destruction varied between the patients.

2.2.2 Patient-specific Biomechanical Model

To develop the patient-specific biomechanical model, the lung geometry, tissue mechanical properties, loadings, and boundary conditions are required. The heterogeneous and homogeneous models were similar in terms of the procedures involved in obtaining the model geometry, boundary conditions, and spatial pattern of the

loading. In the heterogeneous model, areas affected by either of the COPD phenotypes, the tumor, and the healthy lung parenchyma were assigned different mechanical properties. In the homogeneous model the entire lung parenchyma was modeled with one set of mechanical properties, with only the tumor assigned a separate set of properties. Further details on each model have been provided below.

2.2.2.1 Patient-specific Model Geometry

The 3D CT volume at EE (50%) phase was used to obtain the model geometry for each patient. The lungs were segmented using a region growing-based segmentation method followed by opening and closing operations for smoothing purposes. The automatic segmentation was an extension to the semi-automatic algorithm previously developed by our group (29,43). The 3D model of the lung was created from the closed lung segmentation mask using the open source 3D Slicer software package (44). The IA-FEMesh software package (MIMX, Iowa city, IA, USA) was used to generate volumetric FE mesh of the lung with 8-node hexahedral elements. The FE analysis was performed using the ABAQUS/Standard software (ABAQUS Inc., Pawtucket, RI).

2.2.2.2 Loadings and Boundary Conditions

In a respiratory cycle, the lungs start to expand from EE in response to 1) contraction of the diaphragm, and 2) contraction of external intercostal muscles that expands the chest cavity, consequently resulting in a drop in the transpulmonary pressure, P_T . At EI, the respiratory muscles (diaphragm and external intercostal) relax, causing the diaphragm to return and the ribcage to fall. This leads to an increase in the P_T , forcing the air out of the lungs. The extent of expansion, and therefore the P_T varies for different phases of respiration. In addition, P_T is not spatially uniform on the lung surface. Accordingly, in the biomechanical model, the loadings were defined in terms of the net pressure required to expand the lungs from relaxed phase (EE), to the target phase of respiration, i.e. the P_T . The P_T was applied with a linearly increasing gradient in the posterior to anterior direction. For each patient, the maximum pressure amplitude for each phase of respiration was estimated through an optimization algorithm. Details on the optimization process, the cost function, and the evaluation criteria are described in Section 2.2.3.

The drop in the P_T mainly enlarges the lungs in the medial-lateral (ML) and anterior-posterior (AP) directions whereas the diaphragm is known to cause 60-80% of the thoracic cavity enlargement (60), and hence playing an important role in the lung expansion during inspiration. In this study, the displacement of the diaphragm resulting from its contraction was estimated through a non-rigid registration algorithm. A multi-resolution free form deformation (FFD) algorithm was used to register the relaxed diaphragm at EE to the contracted diaphragm at other respiration phases. The resulting displacement field was then applied in the FE model as prescribed boundary condition at the bottom surface of the lung. Considering the fact that the diaphragm motion is a main source of the lung deformation in the superior-inferior (SI) direction, the precision of the diaphragm-driven prescribed boundary conditions is crucial. However, clinical 4DCT image data acquired for radiation therapy planning are often low contrast and include breathing-induced artifacts that affects image interpretation, especially within the areas close to the diaphragm surface as shown in Figure 2-1(45,46). Yamamoto T. et al. have investigated and classified the different types of artifacts attributed to internal motion of the organs during the 4DCT acquisition, and explained the complications such artifacts can cause in RT procedures (46).

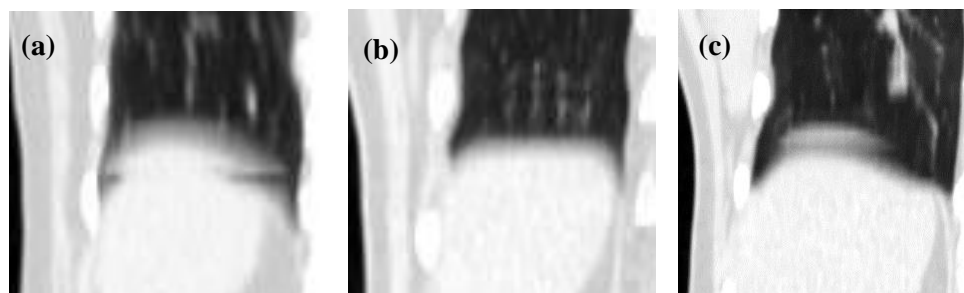


Figure 2-1. Examples of motion-induced artifacts in the dataset. The images show different types of artifacts as classified by Yamamoto et al. **(a)** Overlapping structure, **(b)** incomplete structure, and **(c)** duplicate structure.

To evaluate the robustness of the proposed biomechanical model, cases with considerable artifacts on and near the diaphragm were included in this study. Although the FFD algorithm fails to register the EE diaphragm to that of another target phases (see Section

2.3.2), it captures the relative spatial pattern of deformation. The major component of the diaphragm displacement is in the SI direction. To compensate for the partial registration due to image artifacts, the diaphragm displacement field was modified using an adaptive correction factor (K_{CF}) for the SI component of the estimated deformation field. The K_{CF} was optimized for each target phase of respiration. Details of the applied optimization framework has been provided in Section 2.2.3.

The respiratory lung motion in the chest cavity is constrained within regions of the lung apex and the lung-ribcage interface. To model such constraints and incorporate them as boundary conditions in the biomechanical model, a semi-automatic image segmentation algorithm that uses information on lungs sliding motion was developed. The algorithm inputs the 3D CT volumes at extremities of respiration (50%, 0%, and 90%) and outputs 3 label maps representing areas corresponding to fixed boundary conditions (constrained in all directions), ML-AP constrained, and SI constrained.

2.2.2.3 Mechanical Properties

To investigate the effects of incorporating pathology-induced heterogeneities on the model performance, both homogeneous and heterogeneous models were developed for each patient. The model geometry, loading configuration, and boundary conditions were similar for both models.

2.2.2.3.1 Homogeneous Biomechanical Model

As for the mechanical properties of the homogeneous model, two material types were defined: lung parenchyma, and the tumor. The tumor was modeled as a linear elastic material. Taking into account the large deformation of the lungs during respiration the lung tissue was modeled as hyperelastic, described by Yeoh strain energy density function (47):

$$U = \sum_{i=1}^3 C_{i0} (\bar{I}_1 - 3)^i + \sum_{k=1}^3 \frac{1}{D_k} (J^{el} - 1)^{2k}, \quad (1)$$

where U is the strain energy potential, I_1 , I_2 , and I_3 are strain invariants (invariants of left Cauchy-Green strain tensor), and J^{el} is the elastic volume ratio (a fraction of the total volume ratio J in constant temperature conditions). The model parameters C_{i0} ($i = 1:3$) and D_k ($k = 1:3$) determine the material's mechanical response and its variations with respect to strain. The coefficients C_{i0} ($i = 1:3$) for the lung tissue were calculated by fitting the experimental stress-strain data found in the literature (40). D_k parameters mainly describe the material incompressibility and its dependence on deformation. The tissue incompressibility modeling is described in Section 2.2.2.3.3.

2.2.2.3.2 Heterogeneous Biomechanical Model

To model the pathology-induced heterogeneities inside the lung parenchyma, the extent of each COPD phenotype was first quantified in the 4DCT images, using a well-known attenuation-based method. In this method, the image voxels in the EI scan with attenuation values lower than -950 Hounsfield Units (HU), denote emphysema (48–52). Similarly, areas in the EE image with attenuation values lower than -856 HU represent air trapping. A deformable image registration was used to register the EI scan to the EE counterpart. The registration transformation was applied to map the emphysematous voxels to the EE image. Finally, the areas affected by SAD were determined as the air trapping voxels that are not caused by emphysema as illustrated in Figure 2-2.

The diseased volumes were subsequently incorporated in the FE analysis by assigning different mechanical properties. The lung parenchyma was classified into 4 material sub-types: healthy, emphysematous, affected by SAD, and the tumor. The Yeoh hyperelastic model was used to model the mechanical properties of healthy and diseased tissues except the tumor. The elasticity coefficients (C_{10} , C_{20} , and C_{30}) for the healthy tissue were the same as that of the lung parenchyma in the homogeneous model. The Yeoh hyperelastic coefficients for each of the emphysema and SAD tissue sub-types were optimized using an algorithm described in Section 2.2.3.

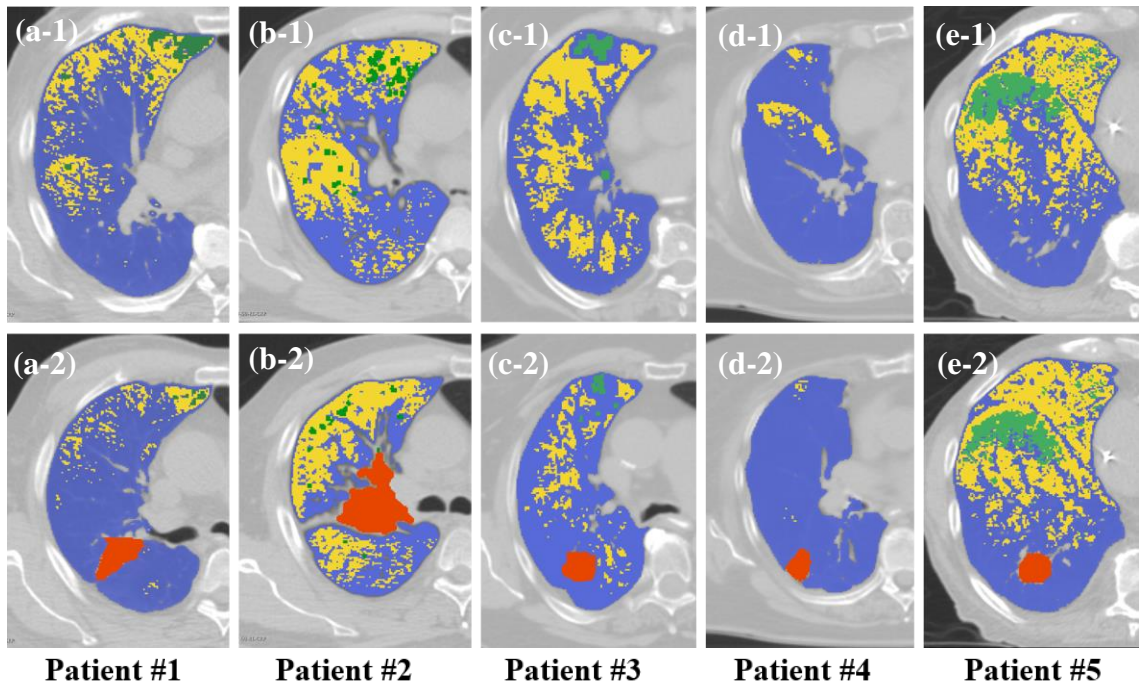


Figure 2-2. Axial view of slices from 4DCT data showing emphysema (green), SAD (yellow), and the tumor (red). Healthy lung parenchyma is represented by blue. **(a)** Patient #1, with extensive SAD, less emphysema. **(b)** Patient #2, with extensive SAD, less emphysema, very large tumor. **(c)** Patient #3, the tumor is located further from COPD-affected volumes. **(d)** Patient #4, very less SAD and no emphysema. **(e)** Patient #5, with extensive SAD and emphysema, tumor in proximity of affected areas.

2.2.2.3.3 Incompressibility Variation during Respiration

As previously described in the studies conducted by our group (29,43), lung tissue incompressibility varies throughout respiration as the air content within the tissue changes substantially between the inhalation and exhalation phases. In the previous studies the variations in incompressibility of lung tissue was modeled by optimizing Poisson's ratio for each phase of respiration. Alternatively, the Yeoh hyperelastic model applied in this study can describe the mechanical behavior of the lung at all respiration phases with one set of C_{i0} and D_k parameters. Specifically, the D_k parameters describe the changes in tissue incompressibility with respect to variations in deformation during respiration that are proportional to the air content of the lung. Therefore, optimizing the

D_k parameters in the model accounts for the variable tissue incompressibility as a result of changes in air volume of the lung during respiration.

2.2.3 Optimization Framework

A number of the biomechanical model parameters including maximum pressure amplitude, diaphragm registration correction factor and the tissue mechanical properties were optimized for each patient. The maximum pressure amplitude and the diaphragm registration correction factor are parameters that depend on the phase of respiration and should be optimized for each target phase separately. However, some of the mechanical properties are phase-independent and must hold a consistent value throughout all phases for each patient. The phase-independent mechanical properties include: the elasticity parameters (C_{i0s}) for diseased sub-types in the heterogeneous model, and the incompressibility parameters of the lung tissue for both the homogeneous and heterogeneous models. On this basis, two optimization algorithms, one for the phase-dependent and another for the phase-independent parameters were developed and used in turn for both the homogeneous and heterogeneous models.

The first optimization algorithm was implemented in MATLAB (MathWorks, USA) for computing the phase-dependent parameters; it is shown in Figure 2-3. The 4DCT scans were segmented to obtain the lung and tumor geometries at 50% (ϕ_{50}) and each target phase ($\phi_i, i \in \{0, 10, 20, 30, 40, 60, 70, 80, 90\}$). Lung geometry at ϕ_{50} was used as the reference geometry to generate FE mesh for the analysis. The iterative FE analysis was started using initial values for the transpulmonary pressure ($P_i = -1.8 \text{ cmH}_2\text{O}$) and the diaphragm registration correction factor ($K_{CF_i} = 1$) for each phase (ϕ_i). Since the mechanical properties for the heterogeneous tissue sub-types are unknown at this point, we started with the homogeneous material properties, simulating the deformation of the lungs expanding from ϕ_{50} to ϕ_i , and generating registered images, to ϕ_i . The optimization cost function was formulated to minimize the Hausdorff surface-to-surface distance (HD) between the actual (Tr_{A_j}) and simulated (Tr_{S_j}) tumor images, while maximizing the Normalized Mutual Information (NMI) within the lung in the actual (Lg_{A_j}) and simulated (Lg_{S_j}) images:

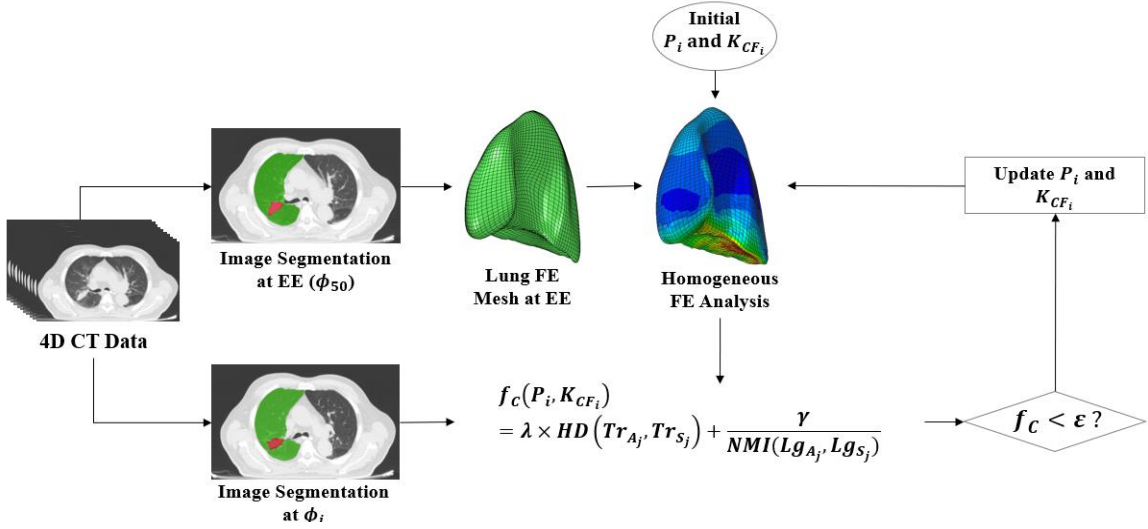


Figure 2-3. Flowchart showing the first optimization step. The 4DCT data is used to segment the lung and the tumor at phase EE (ϕ_{50}) and the target phase, for which the maximum pressure amplitude (P_i) and the diaphragm registration correction factor (K_{CF_i}) are optimized. The homogeneous finite element model is used in this step to deform the reference geometry to the target counterpart. The cost function f_c regulates the updating of the parameters to ensure the best registration.

$$f_c(P_i, K_{CF_i}) = \lambda \times HD(Tr_{A_j}, Tr_{S_j}) + \frac{\gamma}{NMI(Lg_{A_j}, Lg_{S_j})}, \quad (2)$$

where λ and γ are constants used as weight factors and were chosen to regulate the relative effect of each measure (HD and NMI) on the optimization based on their importance and the range by which they vary.

After conducting this optimization step on the homogeneous model for all phases of respiration individually, we can utilize the resulting pressure values in the second optimization step for computing the phase-independent parameters, i.e. elasticity properties and incompressibility. However, in determining the deformation, the pressure and the mechanical properties are interrelated. Accordingly, fixing the pressure values to what is obtained from the first step of the optimization when optimizing for mechanical properties in the second step may lead to complications such as falling into local minima. To account for the interrelation of pressure and mechanical properties, we must allow for

the pressure to adjust during the second optimization process. In this regard, the pressure values resulting from the first optimization are employed to form a parametric representation of the pressure using Fourier series (Eq. 3). The Fourier representation serves as a proper estimation of the pressure at each phase. This parametric representation allows for optimization of the pressure through optimizing for the Fourier coefficients c_1 and c_2 . Therefore, amplitude of the pressure can be optimized in the second optimization step as a function of time (i.e. respiration phase):

$$P_T(t, c_1, c_2) = c_1 \sum_{n=0}^3 (a_n \cos n\omega t) + c_2 \sum_{n=0}^3 (b_n \sin n\omega t), \quad (3)$$

where t is time (respiration phase), ω represents base frequency, and a_n and b_n are the relative amplitudes of different frequency components of sine and cosine functions.

The second optimization step was developed and utilized to compute the phase-independent parameters in both homogeneous and heterogeneous models. In both cases, c_1 and c_2 (used to adjust the pressure) and the incompressibility parameters (D_i) are optimized. In the heterogeneous model the hyperelasticity coefficients for different tissue material sub-types including $C_{i0_{Emphysema}}$ and $C_{i0_{SAD}}$ are also optimized. Information from all phases of respiration are incorporated in each optimization iteration to accommodate for optimization of phase-independent parameters. The cost function used for optimization is consistent between the homogeneous and heterogeneous models. In each iteration of optimization, the HD between the tumor images, and the NMI between actual and simulated lung images for all target phases are calculated and combined as shown in Eq. 4:

$$\begin{aligned} & f_C(c_1, c_2, D_i, C_{i0_k}) \quad \begin{matrix} i \in \{1:3\}, \\ k \in \{Emphysema, SAD\} \end{matrix} \\ & = \lambda \times \sqrt{\sum_j HD^2(Tr_{A_j}, Tr_{S_j})} + \frac{\gamma}{\sqrt{\sum_j NMI^2(Lg_{A_j}, Lg_{S_j})}} \quad (4) \end{aligned}$$

2.3 « Results »

The heterogeneous and homogeneous models were implemented using 4DCT data of 5 patients. The model parameters were computed through the two-step optimization algorithm. The optimized models were used to register the EE scan to other respiration phases. The proposed algorithm is evaluated, and the accuracy of the homogeneous and heterogeneous models for registration are compared.

2.3.1 Two-step Optimization Algorithm

The Fourier parametric representation of the maximum pressure amplitude obtained from the first optimization step was evaluated in the first step. The coefficient of determination (R^2) and the normalized root mean square deviation ($NRMSD$) of the Fourier estimation of pressure for each patient are given in Table 2-1. The accuracy of the Fourier fitting is reasonable for this application, because the estimated representation is used to assign initial values for the second step of optimization.

Table 2-1 Evaluation results for the Fourier representation of optimized pressure.

Patient #	R^2	$NRMSD$
1	0.9794	0.1845
2	1	0
3	0.9791	0.1233
4	0.9672	0.1312
5	0.9932	0.0621

2.3.2 Diaphragm FFD Registration Algorithm

Considering the important role of displacement boundary conditions determined by the diaphragm registration on the modelling accuracy, we assessed the functionality of the proposed method for correcting the diaphragm FFD registration. The registration correction factor (K_{CF}) is optimized for each respiration phase during the first optimization step. In some patients, the artifacts are more prominent than the others. Figure 2-4 shows an example of the substantial improvement in diaphragm registration. Figure 2-4(a) is the difference image between the source (EE phase) and target images

before registration, Figure 2-4(b) illustrates the same after registration with FFD algorithm, and Figure 2-4(c) shows the same after applying the K_{CF} to the deformation field.

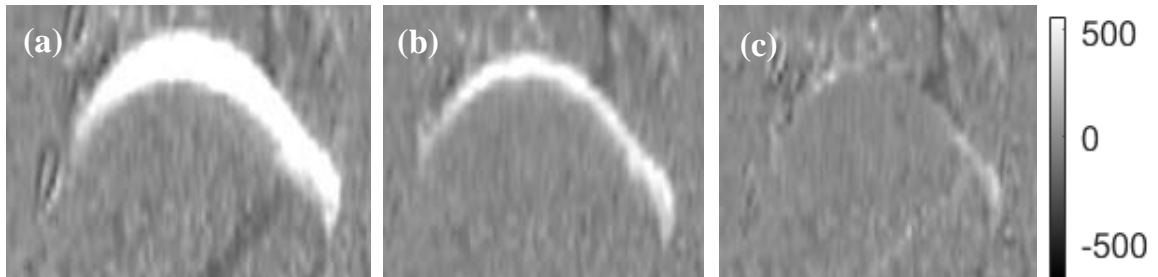


Figure 2-4. Difference image between diaphragm at EE (50%) and EI (0%), (a) before registration, (b) after registration using FFD image registration, (c) after registration using the optimized K_{CF} parameter applied to the deformation field.

2.3.3 Tumor motion/deformation estimation and Registration Accuracy

The accuracy of the image registration using the heterogeneous and homogeneous biomechanical models were evaluated using various criteria. To evaluate the accuracy of tumor registration, the tumor volumes from the actual and registered CT images were compared for each target phase of respiration using the Dice similarity coefficient, and Hausdorff surface-to-surface distance (HD). Figure 2-5 demonstrates the evaluation results of tumor registration for each patient.

In all cases, the average Dice coefficient increased, and the HD decreased when the heterogeneous model was used, which shows the positive impact of incorporating the patho-physiological changes of the lung structure in the model. The extent to which the accuracy of tumor motion/deformation estimation improved by using the heterogeneous model was different among cases. We calculated the percentage volume (%V) of COPD phenotypes (emphysema and SAD) in each case, as shown in Table 2-2. We also calculated the percentage improvement in the average measures of tumor motion/deformation accuracy (Dice and HD) when the heterogeneous model is used instead of the homogeneous model for each case. As show in Table 2-2, more tangible

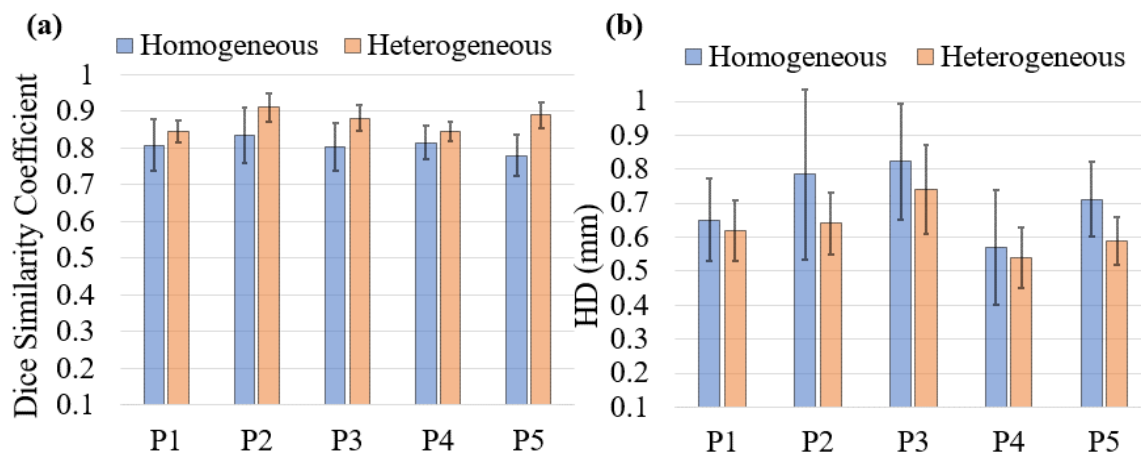


Figure 2-5. Comparing the results of tumor motion/deformation estimation between homogeneous and heterogeneous models. **(a)** Average Dice similarity coefficient and **(b)** average Hausdorff distance (HD) between actual and simulated tumors over all target phases.

improvement in Dice and HD is observed with increased COPD severity. Patients #2, #3 and #5 showed highest improvements in Dice coefficient, whereas Patients #1 and #4 did not benefit tangibly (<5% increase in Dice and <10% decrease in HD) from incorporating COPD-induced heterogeneity in mechanical properties. Even though Patient #2 has a higher COPD severity compared to Patient #3 (emphysema and SAD combined), the % increase in Dice is lower for Patient #2. This is particularly attributed to the sensitivity of Dice coefficient to the size of the compared volumes.

Table 2-2 The extent of COPD phenotypes represented in their percentage volume (%V), and the percentage improvement in measures of tumor motion/deformation estimation for each case.

	Patient #1	Patient #2	Patient #3	Patient #4	Patient #5
Emphysema (%V)	2.6	1.1	2.5	0.2	6.5
SAD (%V)	5.9	19.4	13.9	3.7	21.4
%Increase in Dice	4.4	9.0	9.9	3.8	14.1
%Decrease in HD	4.8	18.5	10.0	5.3	17.0

The larger the tumor size, the less sensitive the Dice is to variations in the compared volumes. Patient #2's tumor size is considerably larger than the Patient #3's (4.2 cm^3 vs 61.9 cm^3), and therefore the %increase in Dice smaller. The % decrease in HD is largest for Patient #2 with the highest COPD severity (emphysema and SAD combined), and is smallest for Patients #1 and #4 for with lowest COPD-affected %V.

The accuracy of the tumor motion estimation during respiration was evaluated by comparing the displacement of the center of mass (CoM) of tumor in 4DCT scans with that obtained after registration using the homogeneous and heterogeneous FE models (Figure 2-6). The magnitude of tumor CoM motion during respiration is plotted separately for each case. The AP and ML components of tumors' CoM motion were relatively small (compared to the SI component) and showed similar results for homogeneous and heterogeneous models. As shown in Figure 2-6 both homogeneous and heterogeneous models follow the magnitude of tumor's CoM displacement, however, heterogeneous model shows superior performance.

To assess the functionality of the proposed biomechanics-based method for lung image registration, we calculated landmarks registration error (LRE), as a standard measure of registration error (23,53) for 3 of the patients. LRE was defined as mean Euclidean distance between 30-40 pairs of landmarks throughout the lung, identified using bifurcation points in the source (EE, 50%) and the target images. Because manual landmarks identification is a time-consuming task, we used Patients #2, #3, and #5 as proof of concept. Table 2-3 shows the LRE before and after registration using the homogeneous and heterogeneous models for each patient.

Comparing the LRE before and after the registration with either of the homogeneous or heterogeneous models shows the high accuracy of the biomechanical model-based registration proposed in this work.

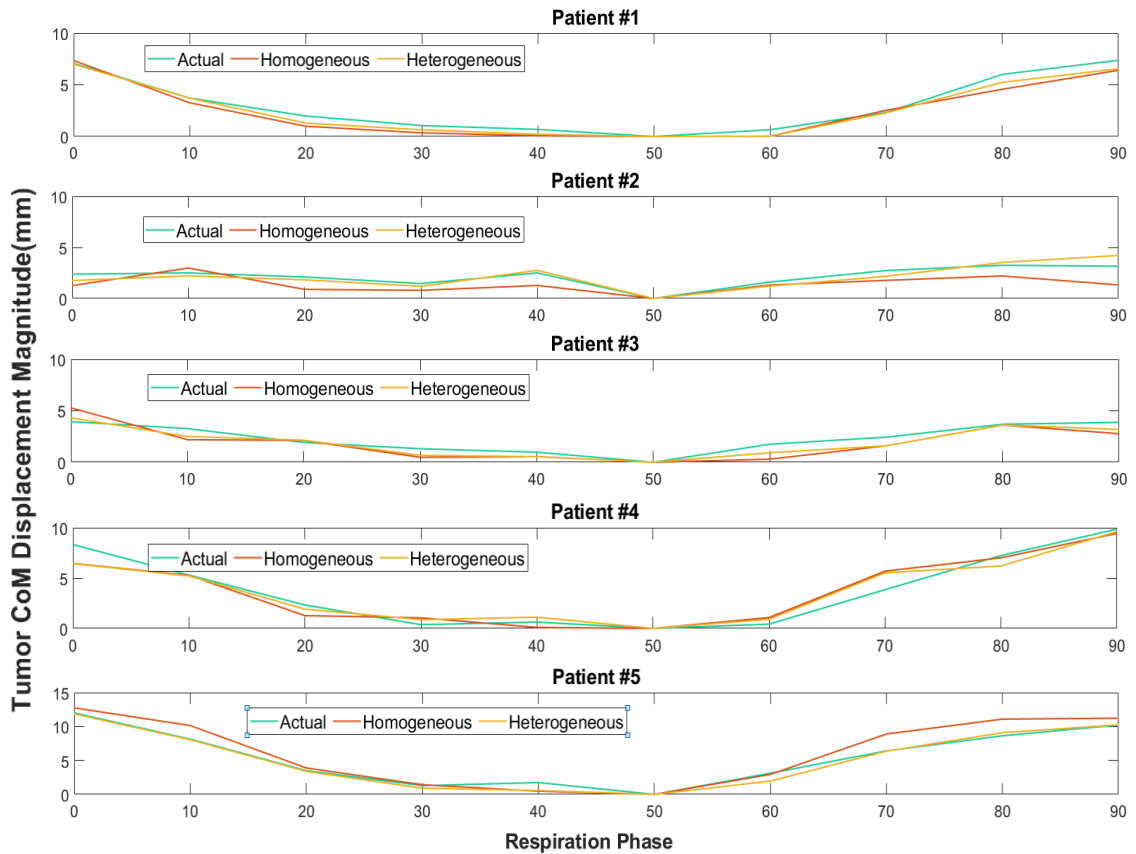


Figure 2-6. Actual tumor CoM motion magnitude and the simulated tumor CoM motion magnitude using homogeneous and heterogeneous models.

Table 2-3 Average LRE for all patients before and after registration with homogeneous and heterogeneous models

Patient #	LRE _{before} (mm)	After Registration	
		LRE _{Homogeneous} (mm)	LRE _{Heterogeneous} (mm)
2	7.67 ± 3.32	2.77 ± 0.93	1.85 ± 0.91
3	6.9 ± 4.28	2.55 ± 1.06	2.23 ± 1.10
5	6.77 ± 4.12	2.51 ± 0.88	1.52 ± 0.90

2.4 «Discussion»

In this work a patient-specific biomechanical model-based image registration algorithm was proposed for lung cancer patients that mimics the breathing physiology and incorporates the pathophysiology of lung in patients with COPD. Specifically, changes in the structure of lung parenchyma as a result of different COPD phenotypes were considered in the biomechanical model. The results demonstrated that changes in the mechanical properties of the lung parenchyma due to COPD have considerable effects on the accuracy of biomechanics-based image registration algorithm. Particularly, the heterogeneous FE model resulted in higher accuracies for tumor motion/deformation estimation compared to its homogeneous counterpart in all patients, regardless of the variations in size and/or location of the tumor. In addition to the increase in average accuracy, the error bars are considerably smaller when the heterogeneous model is used for registration (Figure 2-5). Our method registers the CT image acquired at the EE phase to other phases of respiration by deforming the EE geometry. As one would expect, the lowest registration accuracies are observed when the required deformation is the largest, which is when the target phase for registration is the furthest respiration phase from EE (the source phase), i.e. the peak-inhale phases. Therefore, the reductions observed in the error bars along with the increase in the average of the accuracy measures when the heterogeneous model is used implies increased accuracy of the model, especially for estimation of large deformation. Considering that lungs undergo large deformation during respiration, this observation highlights the impact of using optimized hyperelastic mechanical properties for healthy and pathological tissue sub-types in the FE model.

The estimation of tumor displacement using either of the models closely followed the actual magnitude of tumor's CoM displacement, and its components in all directions. This characteristic of the model is very important in the radiation therapy application because the model is capable of estimating the location of the tumor during all phases of respiration, as well as its shape. This is essential for developing intrafraction and interfraction tumor motion compensation systems.

The proposed image registration technique can also be used for lung image registration in addition to tumor motion prediction. The proposed lung image registration shows similar

accuracy (as represented by LRE) to the current intensity-based DIR algorithms (54,55) and biomechanics-based image registration methods proposed elsewhere (53). For example, Han L. et al. proposed a hybrid DIR for lung peak CT pairs that combines a biomechanical of the lungs with a BSpline-based DIR (56). They showed that the resulting motion field describes the underlying physiology more realistically, and the accuracy of registration is improved compared to the intensity-based DIR algorithm (56). They reported an average target registration accuracy of 1.37 ± 0.89 mm for registering peak-inspiration CT pairs with 2.5 mm slice thickness and in-plane resolutions ranging from $0.97 \text{ mm} \times 0.97 \text{ mm}$ to $1.16 \text{ mm} \times 1.16 \text{ mm}$.

Respiration motion-induced artifacts cause inaccuracies in current thoracic image registration methods (57). The quality of the low-dose clinical CT scans including the RT treatment planning CTs are commonly limited by these artifacts. In this work, the physiology-inspired biomechanical model performance is not affected by the motion artifacts present in the dataset, suggesting the capability of the model to be used to process clinical CT data.

The optimization algorithm maximizes the registration accuracy by finding the proper mechanical properties of the emphysematous and SAD-affected tissue, located based on the CT intensity values (HU). This method can potentially be used to provide in-vivo estimates of tissue mechanical properties of different regions of the lung characterized by different CT intensities. The estimated mechanical properties possibly provide supplementary information for tissue characterization in diagnostic and prognostic applications.

One limitation of the current study is that in all investigated cases, the tumor is in the right lung. Modeling the motion of the tumors located in the left lung can be more challenging due to complexities caused by the interactions with the heart mechanics. Our group has developed and investigated a number of FE models for the heart (58,59). Future research directions may include integrating the heart and the lung FE models to obtain realistic biomechanics-based image registration for the left lung.

«References»

1. Ferlay J, Soerjomataram I, Dikshit R, All E. Cancer incidence and mortality worldwide: Sources, methods and major patterns in GLOBOCAN 2012. *Int J Cancer*. 2015;
2. Albain KS, Swann RS, Rusch VW, Turrisi AT, Shepherd FA, Smith C, et al. Radiotherapy plus chemotherapy with or without surgical resection for stage III non-small-cell lung cancer: a phase III randomised controlled trial. *Lancet*. 2009;
3. Furuse K, Fukuoka M, Kawahara M, Nishikawa H, Takada Y, Kudoh S, et al. Phase III study of concurrent versus sequential thoracic radiotherapy in combination with mitomycin, vindesine, and cisplatin in unresectable stage III non-small-cell lung cancer. *J Clin Oncol*. 1999;
4. Timmerman R, Paulus R, Galvin J, Michalski J, Straube W, Bradley J, et al. Stereotactic body radiation therapy for inoperable early stage lung cancer. *JAMA - J Am Med Assoc*. 2010;
5. Chun SG, Hu C, Choy H, Komaki RU, Timmerman RD, Schild SE, et al. Impact of intensity-modulated radiation therapy technique for locally advanced non-small-cell lung cancer: A secondary analysis of the NRG oncology RTOG 0617 randomized clinical trial. *J Clin Oncol*. 2017;
6. Bzdusek K, Friberger H, Eriksson K, Hrdemark B, Robinson D, Kaus M. Development and evaluation of an efficient approach to volumetric arc therapy planning. *Med Phys*. 2009;
7. Keall PJ, Mageras GS, Balter JM, Emery RS, Forster KM, Jiang SB, et al. The management of respiratory motion in radiation oncology report of AAPM Task Group 76. *Medical Physics*. 2006.
8. Palma D, Vollans E, James K, Nakano S, Moiseenko V, Shaffer R, et al. Volumetric Modulated Arc Therapy for Delivery of Prostate Radiotherapy: Comparison With Intensity-Modulated Radiotherapy and Three-Dimensional

- Conformal Radiotherapy. *Int J Radiat Oncol Biol Phys.* 2008;
9. Otto K. Volumetric modulated arc therapy: IMRT in a single gantry arc. *Med Phys.* 2008;
 10. Hoover DA, Capaldi DPI, Sheikh K, Palma DA, Rodrigues GB, Dar AR, et al. Functional lung avoidance for individualized radiotherapy (FLAIR): Study protocol for a randomized, double-blind clinical trial. *BMC Cancer.* 2014;
 11. Glide-Hurst CK, Chetty IJ. Improving radiotherapy planning, delivery accuracy, and normal tissue sparing using cutting edge technologies. *Journal of Thoracic Disease.* 2014.
 12. Boda-Heggemann J, Knopf AC, Simeonova-Chergou A, Wertz H, Stieler F, Jahnke A, et al. Deep Inspiration Breath Hold - Based Radiation Therapy: A Clinical Review. *International Journal of Radiation Oncology Biology Physics.* 2016.
 13. Keall PJ, Kini VR, Vedam SS, Mohan R. Potential radiotherapy improvements with respiratory gating. *Australas Phys Eng Sci Med.* 2002;
 14. Hara R, Itami J, Kondo T, Aruga T, Abe Y, Ito M, et al. Stereotactic single high dose irradiation of lung tumors under respiratory gating. *Radiother Oncol.* 2002;
 15. Wierzbicki M, Mathew L, Swaminath A. A method for optimizing planning target volume margins for patients receiving lung stereotactic body radiotherapy. *Phys Med Biol.* 2018;
 16. Riblett MJ, Christensen GE, Weiss E, Hugo GD. Data-driven respiratory motion compensation for four-dimensional cone-beam computed tomography (4D-CBCT) using groupwise deformable registration. *Med Phys.* 2018;
 17. Wang H, Dong L, O'Daniel J, Mohan R, Garden AS, Kian Ang K, et al. Validation of an accelerated "demons" algorithm for deformable image registration in radiation therapy. *Phys Med Biol.* 2005;

18. li R, Jia X, Lewis J, gu X, Folkerts M, Men C, et al. WE-C-204B-05: Real-Time Volumetric Image Reconstruction and 3D Tumor Localization Based on a Single X-Ray Projection Image during Lung Cancer Radiotherapy. In: Medical Physics. 2010.
19. Nakamura M, Ishihara Y, Matsuo Y, Iizuka Y, Ueki N, Iramina H, et al. Quantification of the kV X-ray imaging dose during real-time tumor tracking and from three- and four-dimensional cone-beam computed tomography in lung cancer patients using a Monte Carlo simulation. J Radiat Res. 2018;
20. Vandemeulebroucke J, Bernard O, Rit S, Kybic J, Clarysse P, Sarrut D. Automated segmentation of a motion mask to preserve sliding motion in deformable registration of thoracic CT. Med Phys. 2012;
21. Rietzel E, Chen GTY. Deformable registration of 4D computed tomography data. Med Phys. 2006;
22. Han L, Dong H, McClelland JR, Han L, Hawkes DJ, Barratt DC. A hybrid patient-specific biomechanical model based image registration method for the motion estimation of lungs. Med Image Anal. 2017;
23. Werner R, Ehrhardt J, Schmidt R, Handels H. Patient-specific finite element modeling of respiratory lung motion using 4D CT image data. Med Phys. 2009;
24. Fuerst B, Mansi T, Zhang J, Khurd P, Declerck J, Boettger T, et al. A personalized biomechanical model for respiratory motion prediction. Med Image Comput Comput Assist Interv. 2012;
25. Al-Mayah A, Moseley J, Velec M, Brock KK. Sliding characteristic and material compressibility of human lung: Parametric study and verification. Med Phys. 2009;
26. Fuerst B, Mansi T, Carnis F, Sälzle M, Zhang J, Declerck J, et al. Patient-specific biomechanical model for the prediction of lung motion from 4-D CT images. IEEE Trans Med Imaging. 2015;

27. Al-Mayah A, Moseley J, Velec M, Hunter S, Brock K. Deformable image registration of heterogeneous human lung incorporating the bronchial tree. *Med Phys*. 2010;
28. Al-Mayah A, Moseley J, Velec M, Brock K. Effect of friction and material compressibility on deformable modeling of human lung. In: *Lecture Notes in Computer Science (including subseries Lecture Notes in Artificial Intelligence and Lecture Notes in Bioinformatics)*. 2008.
29. Shirzadi Z, Sadeghi-Naini A, Samani A. Toward in vivo lung's tissue incompressibility characterization for tumor motion modeling in radiation therapy. *Med Phys*. 2013;40(5):051902.
30. Samavati N, Velec M, Brock K. A hybrid biomechanical intensity based deformable image registration of lung 4DCT. *Phys Med Biol*. 2015;
31. Li M, Castillo E, Zheng XL, Luo HY, Castillo R, Wu Y, et al. Modeling lung deformation: A combined deformable image registration method with spatially varying Young's modulus estimates. *Med Phys*. 2013;
32. Gaede S, Lee T-Y, Samani A, Karami E. A machine learning approach for biomechanics-based tracking of lung tumor during external beam radiation therapy. In: *Medical Imaging 2018: Image-Guided Procedures, Robotic Interventions, and Modeling*. 2018.
33. Ytterstad E, Moe PC, Hjalmsen A. COPD in primary lung cancer patients: Prevalence and mortality. *Int J COPD*. 2016;
34. Spyrtos D, Papadaki E, Lampaki S, Kontakiotis T. Chronic obstructive pulmonary disease in patients with lung cancer: prevalence, impact and management challenges. *Lung Cancer (Auckland, NZ)* [Internet]. 2017;8:101—107. Available from: <http://europepmc.org/articles/PMC5558876>
35. Ceresa M, Olivares AL, Suelves SF, Noailly J, Ballester MAG. Multi-scale immunological and biomechanical model of emphysema progression. In:

- Proceedings of the Annual International Conference of the IEEE Engineering in Medicine and Biology Society, EMBS. 2017.
36. Ceresa M, Olivares AL, Noailly J, Ballester MAG. Coupled immunological and biomechanical model of emphysema progression. *Front Physiol.* 2018;
 37. MEAD J, LINDGREN I, GAENSLER EA. The mechanical properties of the lungs in emphysema. *J Clin Invest.* 1955 Jul;34(7, Part 1):1005–16.
 38. Liu T, Wang Y, Ma J, Li D, Fan Y. Effects of changing small airway mechanics and inspiratory flow waveforms on pulmonary ventilation: A modeling study. In: *IFMBE Proceedings.* 2015.
 39. Shirzadi Z, Sadeghi-Naini A, Samani A. Toward in vivo lungs tissue incompressibility characterization for tumor motion modeling in radiation therapy. *Med Phys.* 2013;
 40. Zeng YJ, Yager D, Fung YC. Measurement of the Mechanical Properties of the Human Lung Tissue. *J Biomech Eng.* 1987;
 41. Villard PF, Beuve M, Shariat B, Baudet V, Jaillet F. Simulation of lung behaviour with finite elements : Influence of bio-mechanical parameters. In: *Proceedings - Third International Conference on Medical Information Visualisation - BioMedical Visualisation, MediVis 2005.* 2005. p. 9–14.
 42. Sadeghi Naini A, Patel R V., Samani A. Measurement of lung hyperelastic properties using inverse finite element approach. *IEEE Trans Biomed Eng.* 2011;
 43. Karami E, Gaede S, Lee T-Y, Samani A. A biomechanical approach for in vivo lung tumor motion prediction during external beam radiation therapy. In: *Medical Imaging 2015: Image-Guided Procedures, Robotic Interventions, and Modeling.* 2015. p. 94151.
 44. Fedorov A, Beichel R, Kalpathy-Cramer J, Finet J, Fillion-Robin JC, Pujol S, et al. 3D Slicer as an image computing platform for the Quantitative Imaging Network.

Magn Reson Imaging. 2012;

45. Yamamoto T, Langner U, Loo BW, Shen J, Keall PJ. Retrospective Analysis of Artifacts in Four-Dimensional CT Images of 50 Abdominal and Thoracic Radiotherapy Patients. *Int J Radiat Oncol Biol Phys*. 2008;
46. Han D, Bayouth J, Bhatia S, Sonka M, Wu X. Characterization and identification of spatial artifacts during 4D-CT imaging. *Med Phys*. 2011;
47. Yeoh OH. Some Forms of the Strain Energy Function for Rubber. *Rubber Chem Technol*. 1993;
48. Galbán CJ, Han MK, Boes JL, Chughtai KA, Meyer CR, Johnson TD, et al. Computed tomography-based biomarker provides unique signature for diagnosis of COPD phenotypes and disease progression. *Nat Med*. 2012;
49. Schroeder JD, McKenzie AS, Zach JA, Wilson CG, Curran-Everett D, Stinson DS, et al. Relationships between airflow obstruction and quantitative CT measurements of emphysema, air trapping, and airways in subjects with and without chronic obstructive pulmonary disease. *Am J Roentgenol*. 2013;
50. Mets OM, Buckens CFM, Zanen P, Isgum I, Van Ginneken B, Prokop M, et al. Identification of chronic obstructive pulmonary disease in lung cancer screening computed tomographic scans. *JAMA - J Am Med Assoc*. 2011;
51. Kim SS, Seo JB, Lee HY, Nevrekar D V., Forssen A V., Crapo JD, et al. Chronic Obstructive Pulmonary Disease: Lobe-based Visual Assessment of Volumetric CT by Using Standard Images—Comparison with Quantitative CT and Pulmonary Function Test in the COPDGene Study. *Radiology*. 2013;
52. Matsuoka S, Kurihara Y, Yagihashi K, Hoshino M, Watanabe N, Nakajima Y. Quantitative assessment of air trapping in chronic obstructive pulmonary disease using inspiratory and expiratory volumetric MDCT. *Am J Roentgenol*. 2008;
53. Han L, Dong H, McClelland JR, Han L, Hawkes DJ, Barratt DC. A hybrid patient-

specific biomechanical model based image registration method for the motion estimation of lungs. *Med Image Anal* [Internet]. 2017 Jul 1 [cited 2019 Jun 18];39:87–100. Available from: <https://www.sciencedirect.com/science/article/pii/S1361841517300555>

54. Guy CL, Weiss E, Christensen GE, Jan N, Hugo GD. CALIPER: A deformable image registration algorithm for large geometric changes during radiotherapy for locally advanced non-small cell lung cancer. *Med Phys*. 2018;
55. Kipritidis J, Tahir BA, Cazoulat G, Hofman MS, Siva S, Callahan J, et al. The VAMPIRE challenge: A multi-institutional validation study of CT ventilation imaging. *Med Phys* [Internet]. 2019 Mar 1 [cited 2019 Jun 26];46(3):1198–217. Available from: <http://doi.wiley.com/10.1002/mp.13346>
56. Han L, Dong H, McClelland JR, Han L, Hawkes DJ, Barratt DC. A hybrid patient-specific biomechanical model based image registration method for the motion estimation of lungs. *Med Image Anal*. 2017;
57. Li M, Castillo SJ, Castillo R, Castillo E, Guerrero T, Xiao L, et al. Automated identification and reduction of artifacts in cine four-dimensional computed tomography (4DCT) images using respiratory motion model. *Int J Comput Assist Radiol Surg*. 2017;
58. Haddad SMH, Drangova M, White JA, Samani A. Towards myocardial contraction force image reconstruction for heart disease assessment and intervention planning. In: *Medical Imaging 2015: Biomedical Applications in Molecular, Structural, and Functional Imaging*. 2015.
59. Dempsey S, Samani A. Determining in-silico left ventricular contraction force of myocardial infarct tissue using a composite material model. In 2018.
60. Noh DK, Lee JJ, You, JH. Diaphragm breathing movement measurement using ultrasound and radiographic imaging: a concurrent validity. *Bio-medical Materials and Engineering*, 24(1), 947-952. 2014.

Chapter 3

3 « 4DCT Ventilation Imaging Using Biomechanical Model-based Deformable Registration »

3.1 « Introduction »

Assessment of the lungs regional function represented by either or a combination of perfusion, diffusion, and ventilation has proven useful in many applications including lung cancer radiation therapy (1) and diagnosis of pulmonary abnormalities such as asthma and chronic obstructive pulmonary disease (COPD) phenotypes (2). Current radiation therapy treatment planning methods assume a homogeneous distribution of lung function and hence a homogeneous treatment response characterized by radiation dose distribution. However, many lung cancer patients have co-existing pulmonary dysfunctions that give rise to pulmonary function heterogeneity (3,4). Functional avoidance treatment planning that preferentially spares the functional lung tissue from radiation dose, has been tested in clinical trials, and has shown to 1) help reduce the incidence and the severity of radiation-induced lung injuries (e.g. radiation pneumonitis and pulmonary fibrosis) (5–8), and 2) enable target dose escalation for more effective treatments (9,10). In addition, monitoring changes in the lungs' regional function during the course of radiation therapy can be used for evaluating treatment response (11). Regional function information has also shown to be useful in applications other than radiation oncology. For example information pertaining to regional distribution and severity of pulmonary diseases such as asthma and COPD phenotypes can be used to develop new therapies and improve existing therapeutic methods (12–14).

Information on regional variations of the lung function can be found non-invasively by various imaging methods. Functional images can be directly generated using positron emission tomography (PET) (15) and single photon emission computed tomography (SPECT) (16). Hyperpolarized ^3He magnetic resonance (MR) imaging has been used for imaging ventilation (2,17), ^{129}Xe MR imaging can be used to obtain information on ventilation, perfusion, or gas exchange (18), and Xenon-enhanced computed tomography (CT) can provide a direct assessment of pulmonary ventilation(19). Four dimensional CT

(4DCT)-based ventilation imaging (CTVI) has recently emerged as a cost-effective and accessible alternative to the abovementioned modalities, with potentially higher spatial resolution compared to nuclear medicine ventilation imaging. CTVI is especially attractive in radiation therapy applications because it can be achieved using treatment planning 4DCT images acquired as part of the routine care in most centers (20). Clinical trials on CTVI-based functional avoidance planning are on-going, with the goal of reducing radiation toxicities (10,21). CTVI has also been used to improve the prediction of radiation pneumonitis and clinical toxicity. For example, Vinogradskiy et al. found a potential reduction in radiation induced toxicities (grade 2+ and 3+ pneumonitis) when CTVI-based functional avoidance planning was used instead of conventional anatomical planning (8). Moreover, dose-response assessment studies have been conducted by evaluating changes in the lung ventilation (as mapped by CTVI) between radiation therapy fractions (22,23) and after radiation therapy (11,24–26).

Different methods have been proposed for CTVI, most of which consist of a “deformable image registration (DIR)” between the peak respiration CT pairs, and a “ventilation metric” (27,28). The accuracy of the DIR method used is a major determining factor in the CTVI accuracy, and hence its clinical benefits (29). Almost all previously proposed CTVI methods are founded on intensity-based DIR algorithms (27,28). Despite advances made in DIR methods, they are based solely on 4DCT image data, and are sensitive to motion artifacts that are frequently encountered in treatment planning 4DCT scans (30). There exist a few commercial DIR methods including Velocity (Varian Medical Systems, Palo Alto, CA, USA) and RayStation (RaySearch Laboratories, Stockholm, Sweden), some open DIR software packages such as Plastimatch (see www.plastimatch.org, last accessed on August, 2019) and Elastix (see <http://elastix.isi.uu.nl/>, last accessed on August 2019), and different in-house methods developed by research labs (27). Intensity-based DIR algorithms do not take into account the physical properties or physiological mechanisms involved in breathing, hence are prone to errors associated with non-uniqueness of the resulting displacement field and registration errors in areas with low image gradients. In addition, handling the sliding motion of the lungs can be challenging for motion estimation using intensity-based DIR methods (31,32).

Biomechanical models have been widely used alone or in combination with intensity-based methods as alternative to DIR approaches (33,34). In contrast to intensity-based DIR, biomechanics-based computational models encompass certain physiological aspects of breathing dynamics rendering this approach more robust and realistic (35–38). Patient-specific lung biomechanical models that use the thoracic image data to extract the lung's geometry and boundary conditions have been previously proposed (34,39,40). Several studies investigated the effects of model parameters including the mechanical properties (39,41,42), and boundary conditions (38) on modeling accuracy. Recently, hybrid hierarchical approaches have been proposed, in which finite element (FE)-based biomechanical models are used in conjunction with intensity-based DIR methods to predict deformation fields of the lung in a respiratory cycle, and to register lung CT image pairs (43,44). For example, Han L. et al. proposed a hybrid biomechanical model-based DIR for lung peak CT pairs, and showed that the resulting motion field describes the underlying physiology more realistically while the accuracy of registration was improved compared to the intensity-based DIR algorithm (43). In this study, we are proposing an accurate biomechanics-based DIR algorithm in conjunction with a sophisticated lung air segmentation algorithm for CTVI. To our knowledge, we are the first group to utilize biomechanical models in a CTVI application.

With respect to a ventilation metric, the current CTVI methods are generally classified as either Hounsfield unit-based (DIR-HU) or Jacobian-based (DIR-Jac) methods, with a few studies reporting a combination of the two (27). The DIR-HU methods use changes in voxels intensity between the end-inhale and end-exhale breathing phases to calculate ventilation. The assumption for calculating ventilation based on DIR-HU is that the lung CT voxels intensity (CT numbers) comprise a linear combination of the CT number of water and that of air, both assumed to be constant (0 HU and -1000 HU, respectively) and therefore the fraction of air within each voxel can be described by a simple linear function (45). Uncertainties resulting from image noise, beam hardening, scanner calibration, and acquisition and reconstruction artifact, can render the assumption of constant CT numbers for tissue and air unreliable (46,47). Using a fixed linear relationship for all patients may lead to inaccurate estimation of the air volume, and hence the ventilation. Therefore, we are proposing the incorporation of an accurate air

volume calculation method that finds patient's scan-specific values for air and tissue intensities based on an advanced thresholding algorithm (48,49).

In addition, the DIR-HU methods do not take into consideration the respiratory changes in the lung volume. On the other hand, the DIR-Jac methods calculate ventilation based on the determinant of Jacobian of the transformation obtained from DIR of the lung CT at the end-inhalation phase to the end-exhalation phase image (50). This approach assumes that local partial derivatives of the deformation field are related to the volume changes of the corresponding voxel. It does not consider changes in the voxels' intensity that can be indicative of changes in the fractional air volume. A CTVI that accounts for both changes in voxels' intensity and regional expansion can provide more realistic information on ventilation.

We are proposing a CTVI technique that combines an accurate biomechanical model-based DIR, with an advanced patient-specific air volume estimation algorithm. In this CTVI technique, we also correct for regional volume expansion based on information obtained from the lung biomechanical model. We evaluate the clinical utility of the proposed CTVI technique by qualitatively and quantitatively comparing the ventilation images with hyperpolarized ^3He MRI of the same patients, used in a clinical trial for functional avoidance planning (3).

3.2 « Materials and Methods »

An overview of the proposed CTVI algorithm is shown in Figure 3-1. Treatment planning 4DCT scans of three patients (see Section 3.2.1.1 for details on data acquisition) are used in this CTVI study. Using a lung biomechanical model, we deformably register the end-exhale (EE) lung CT image to the end-inhale (EI) image. The biomechanical model-based DIR involves reconstruction of the deformed EE image. After the registration step, each voxel in the EI image corresponds to a voxel in the deformed EE image. These two images are fed into an air segmentation algorithm where the distribution of air within each image is found using an advanced thresholding method that incorporates the partial volume effect. The air distribution in the deformed EE image is then corrected with respect to the regional volume expansion information, obtained from the volume change

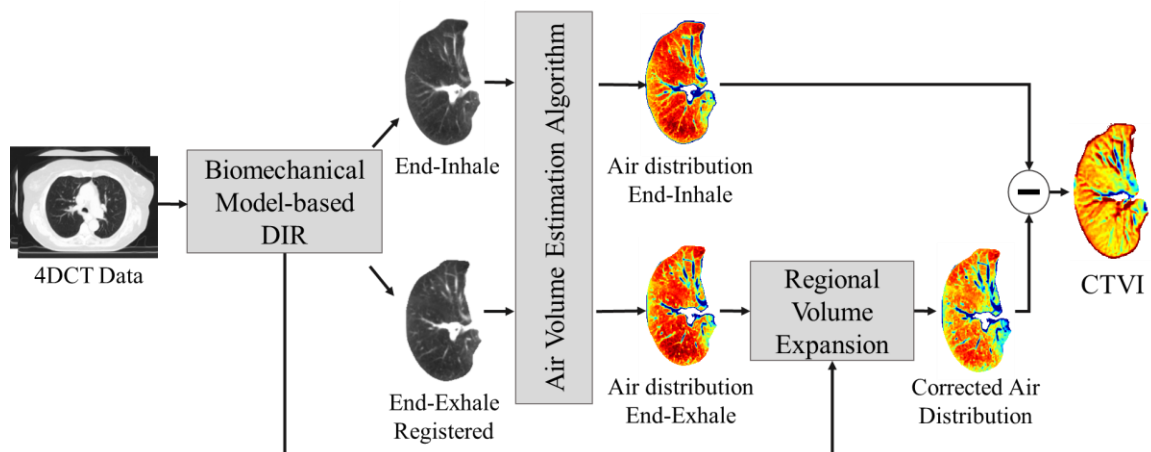


Figure 3-1. The proposed CTVI workflow. The peak-inspiration CT scans are registered using the biomechanics-based DIR. The air segmentation algorithm finds the partial volume of air in each scan after registration. The regional volume expansion is corrected for before the CTVI is calculated as the difference between air volumes in end-inhale and end-exhale voxels.

of corresponding finite elements calculated using finite-element (FE) analysis. The CTVI is then calculated as the difference between the amount of air in the EI voxels and the corrected amount of air in the corresponding EE voxels. In the following sections, each of the abovementioned steps are described in detail.

3.2.1 Data Acquisition

This research was performed in accordance with the institutional research ethics board approval. Three patients from the FLAIR trial were included in this study (3). Patients were diagnosed with non-small-cell lung cancer. Treatment planning 4DCT image sequences, ^3He and ^1H MR, and 3DCT scans of the patients were used in this study.

3.2.1.1 Treatment Planning 4DCT

A 16-slice Philips Brilliance Big Bore CT scanner (Philips Medical Systems) operating in helical mode was used with scan parameters: 120kVp and 400mAs/slice for tube potential and current, respectively. The intra-slice pixel size of the data varied from 0.98 mm \times 0.98 mm to 1.11 mm \times 1.11 mm among patients, and the slice thickness was 3

mm for all scans. The 4DCT images were sorted into 10 respiratory phases using the Real-time Position Management™ system.

3.2.1.2 MR Image Data Acquisition

MR imaging was performed using a whole body 3.0 T MR750 system (GE Health Care, Milwaukee, WI) using a gradient amplitude of 1.94 G/cm and a single channel, rigid elliptical transmit/receive chest coil (Rapid Biomedical GmbH, Wuerzburg, Germany). ³He gas was prepared using a polarizer system (HeliSpin, Polarean, Durham, NC, USA) where polarization levels of approximately 40% were achieved. Hyperpolarized ³He was diluted with medical-grade N₂ gas. Subjects were instructed to inhale the ³He/N₂ gas from functional residual capacity (FRC), from a 1L Tedlar® bag (Jensen Inert Products, FL, USA), and images were acquired during a 16-second breath hold. Coronal (anatomical) ¹H MRI was performed using the whole-body radiofrequency coil and ¹H fast-spoiled, gradient-recalled echo sequence using a partial echo (16 s total data acquisition, repetition time [TR] =4.7 ms, echo time [TE] =1.2 ms, flip angle =30°, field of view =40 cm, bandwidth =24.4 kHz, matrix =128 × 80, 15-17 slices, 15 mm slice thickness). ³He MRI static ventilation images were acquired using a fast gradient echo method using a partial echo (14 s total data acquisition, TR/TE/flip angle =4.3 ms/1.4 ms/7°, field of view =40 cm, bandwidth =48.8 kHz, matrix =128 × 80, 15- 17 slices, 15 mm slice thickness). More details on MRI acquisition are provided in (3).

3.2.1.3 3DCT Scan

Thoracic multi-detector CT images were acquired with the same breath-hold volume and maneuver used for MRI. Patients were scanned in the supine position during inspiration breath-hold from FRC after inhaling 1L of N₂ gas, using a multi-detector, 64-slice Lightspeed VCT scanner (General Electric Health Care, Milwaukee, WI) (64 mm × 0.625 mm collimation, 120 kVp, 100 effective mA, tube rotation time = 500 ms, pitch = 1.0). A spiral acquisition was used and images were reconstructed using a standard convolution kernel to 1.25 mm slice thickness (3).

3.2.2 Biomechanical Model-based DIR

The first step of the proposed CTVI is the deformable registration of the peak-respiration CT image pairs. We developed a patient-specific biomechanical model of the lung to simulate the lung motion and deformation. Reconstruction of the moving image was carried out using an FE-based algorithm that finds the deformation field on voxel-level based on nodal displacements of the FE model.

3.2.2.1 Patient-specific Biomechanical Model of the Lung

A biomechanical model was developed for each patient using data of their 4DCT image sequence. In the following, major components of the biomechanical model are described.

The geometry of the lung at the relaxed state, i.e. at the EE phase, was used to generate the reference geometry. For this purpose, an automated segmentation algorithm was developed based on a Fast-Marching algorithm. The segmentation was validated using the radiation treatment planning contours provided by the radiation oncologist. The lung FE meshes with 8-node hexahedral elements (Figure 3-2) were generated using the IA-FEMesh software package (Musculoskeletal Imaging, Modeling, and EXperimentation: MIMX, the University of Iowa, Iowa city, IA, USA) from the 3D lung model obtained from segmentation at the EE phase.

The lung expansion from the reference geometry (at EE) to EI is attributed to 1) a drop in the transpulmonary pressure (originally caused by an expansion in the chest cavity), and 2) the diaphragm contraction. Accordingly, to simulate the lung motion/deformation during respiration in a physiologically-realistic manner, we model these two mechanisms. To model the transpulmonary pressure, we are applying a negative pressure gradient on the surface of the mesh, with its amplitude described by:

$$P(y) = P_1 + P_2 \times y, \quad (1)$$

where y is the normalized anterior-posterior (AP) location of each surface element's center of mass ($0 \leq y \leq 1$). The parameters P_2 and P_1 are the linear gradient's slope and the minimum pressure at the posterior-most location on the lung surface, respectively.

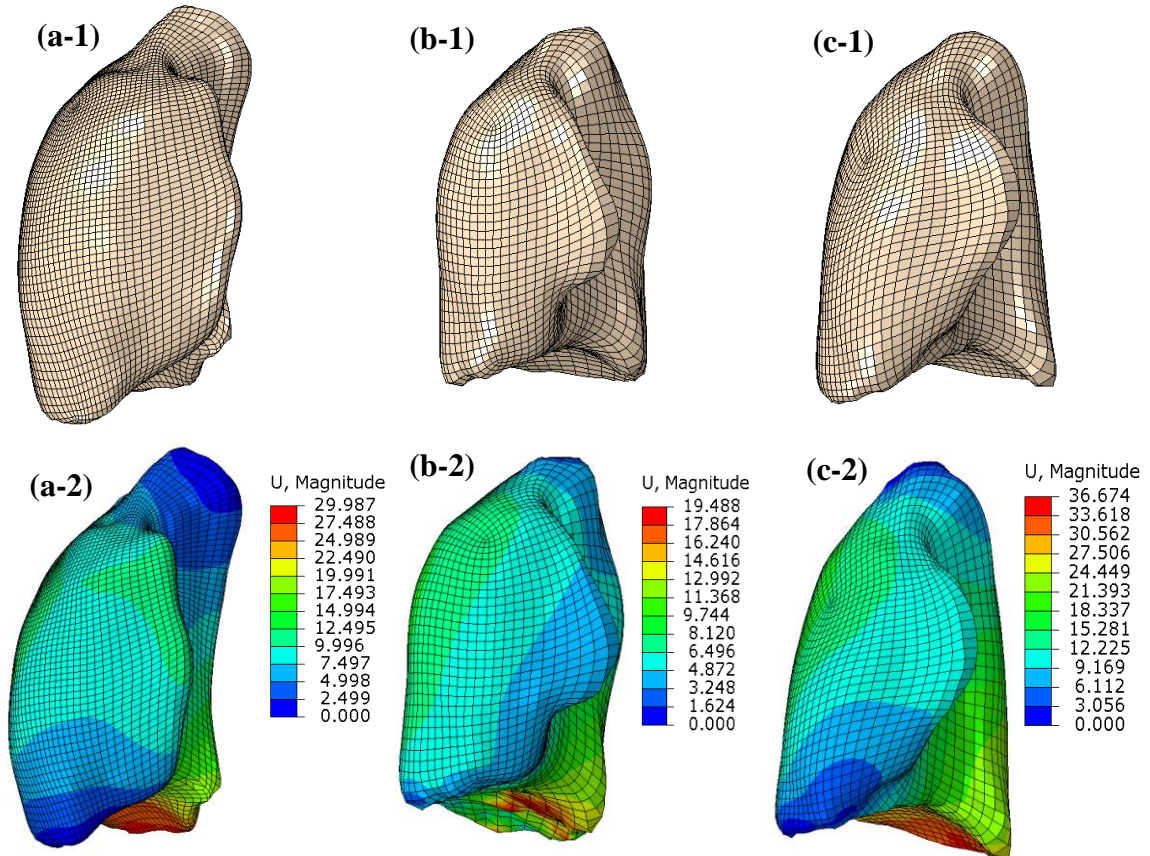


Figure 3-2. Models geometry. The top row figures (a-1, b-1, and c-1) show the lung finite element meshes for the three patients at the end-exhale phase. The bottom row figures (a-2, b-2, and c-2) show the deformed geometries of the same cases after FE analysis. The mesh elements are color-coded according to the magnitude of displacements in mm.

The assumption of having increasing pressure amplitude in the anterior direction is made to simulate patient's breathing condition in supine position when the CT is acquired. Because accurate values for P_1 and P_2 are unknown for each patient (unless measured invasively), they are found through an inverse-problem formulation which aims at maximizing the modelling accuracy (the inverse problem is explained at the end of this section). To model the effect of the diaphragm contraction on the expansion of the lung, we extracted the deformation of the diaphragm-lung interface using a free-form deformable image registration algorithm. The displacement field at the diaphragm-lung interface is then applied to the bottom surface of the FE mesh as prescribed displacement

boundary conditions (BCs) to model the lung expansion caused by the diaphragm activity. The quality of the treatment planning 4DCT is usually impaired by motion artifacts, especially around the diaphragm surface. To make sure our model is robust to changes in the image quality, we used our previously described method to correct for the underestimated diaphragm displacement field caused by motion artifacts (explained in Chapter 2). Briefly, a correction factor, $\kappa_{CF}(y)$, was multiplied by the superior-inferior component of the displacement vectors obtained from free-form registration. $\kappa_{CF}(y)$ depends on the AP coordinate (y) of the node where the displacement is applied, and it increases quadratically in the posterior direction. The minimum value of κ_{CF} is 1, and its maximum value is optimized using the inverse-problem formulation described later in this section.

The degree of freedom of the lung motion is limited in some surface areas (e.g. near the apex and in some areas of lung-ribs interfaces). We use a semi-automatic segmentation algorithm that extracts such surface areas that have very limited motion and constrain their degrees of freedom from the 4DCT image information for each patient (for more information, see Section 2.2.2.2). Fixed BCs were applied to the FE nodal points of those areas.

As for the mechanical properties, taking into account the large deformation of the lungs during respiration and based on the results published in previous studies on lung parenchyma mechanical testing and material properties modeling (42,51,52), the lung tissue was modeled as hyperelastic, described by Yeoh strain energy density function (53). Where applicable, we segmented the tumor from the CT image at the EE phase, and identified the location of the tumor in the lung mesh. We modeled the tumor as linear elastic material.

To estimate the patient-specific parameters of the lung biomechanical model that are not directly measured, i.e. the parameters defining the pressure (P_1 and P_2) and κ_{CF} , an inverse-problem formulation was developed. This optimization step aims at maximizing the normalized mutual information (NMI) between the deformed image after the FE analysis and the target image (segmented lung at the EI phase), as well as minimizing the

distance between the simulated and actual lung surfaces. The same lung segmentation algorithm used for EE CT image was employed to segment the lung from the CT image at the EI phase. Details on the cost function, the initial values, and the convergence criteria are provided in Section 2.2.3. The optimized parameters are used to obtain the final displacement field for the FE mesh nodes. The optimization framework was developed in MATLAB (MathWorks, USA), and ABAQUS/Standard 6.14 (Dassault Systèmes Simulia Corp., Providence, RI, USA) was used as the FE solver.

3.2.2.2 Image Reconstruction

To calculate NMI during optimization and to reconstruct the deformed moving image (deformed EE image) after final FE analysis, we need to calculate the deformation field at the voxel-level from the displacement field defined at the FE mesh nodes. There exist interpolation techniques such as spline-based methods (thin plate spline, cubic spline, etc.) that can interpolate values at any point (voxels) from known function values at the control points (FE nodal points) (54–56). However, these methods can generate unrealistic and/or unphysical displacement fields (57). As an alternative approach, we utilized the FE shape functions defined for 8-node hexahedral elements to find the displacement of any voxel inside a given element from the displacements at the nodes of the element. The shape functions are defined as Lagrange interpolation in the element's natural coordinates. This implies that to find the displacement of each voxel within an element from the nodal displacements, the location of the voxel in the corresponding iso-parametric representation of the encompassing element is required. Although the transformation from the iso-parametric representation to the physical coordinates is known, the inverse mapping that is required to find the voxel's natural coordinates is not trivial. We used a novel method designed and implemented by our group that finds the mapping from physical space to iso-parametric (natural) coordinates through an inverse-problem formulation.

3.2.2.3 Evaluation of the Biomechanical Model-based DIR

The high accuracy of the biomechanical model for lung and tumor motion/deformation estimation was previously reported in Chapter 2 (see Section 2.3). To further evaluate the

performance of the proposed biomechanical model-based DIR algorithm for the patients included in this study, we identified approximately 40 landmark pairs at the bifurcation points on the EE and EI images. These landmarks were used to calculate the landmarks registration error (LRE). We also measured the Hausdorff surface-to-surface distance between the reconstructed and target lung surfaces.

We compared the performance of our biomechanics-based registration with intensity-based DIR. We used an off-the-shelf free form deformable registration algorithm to register the EE scan to the EI scan.

3.2.3 Air Segmentation Algorithm

In the proposed CTVI algorithm, the ventilation metric is defined as the change in the air volume at each voxel between EI and EE. After the registration step where the correspondence between the voxels in the EE and EI images is found, the amount of air in each voxel at both phases is required. For this purpose, we used a slightly modified version of an advanced thresholding algorithm previously developed in our lab (48). The accuracy of the air volume estimation is highly dependent on the values denoting air and tissue intensities. Therefore, instead of using fixed values of -1000 HU and 0 HU for air and tissue intensities, this algorithm finds patient-specific values to reduce the uncertainties associated with variable CT scanner parameters or image artifacts. Firstly, two threshold values are initialized based on the combined histogram of EI and EE lung images (Figure 3-3) and are used to classify the voxels in the segmented lung images into 3 groups: 1) entirely air voxels, 2) voxels containing air and soft tissue, and 3) entirely tissue voxels (Figure 3-3(a)). The threshold values were then optimized based on mass conservation law and soft tissue (e.g. alveoli wall tissue) incompressibility assumption. More details on the threshold initialization and optimization can be found in (48). The air volume in voxels in class #1 is the same as the voxel volume and is zero in class #3 voxels. For voxels in the class #2, the partial volume of air (*PVA*) in each voxel is calculated as:

$$PVA = \frac{I_{tis} - I_{vox}}{I_{tis} - I_{air}}, \quad (2)$$

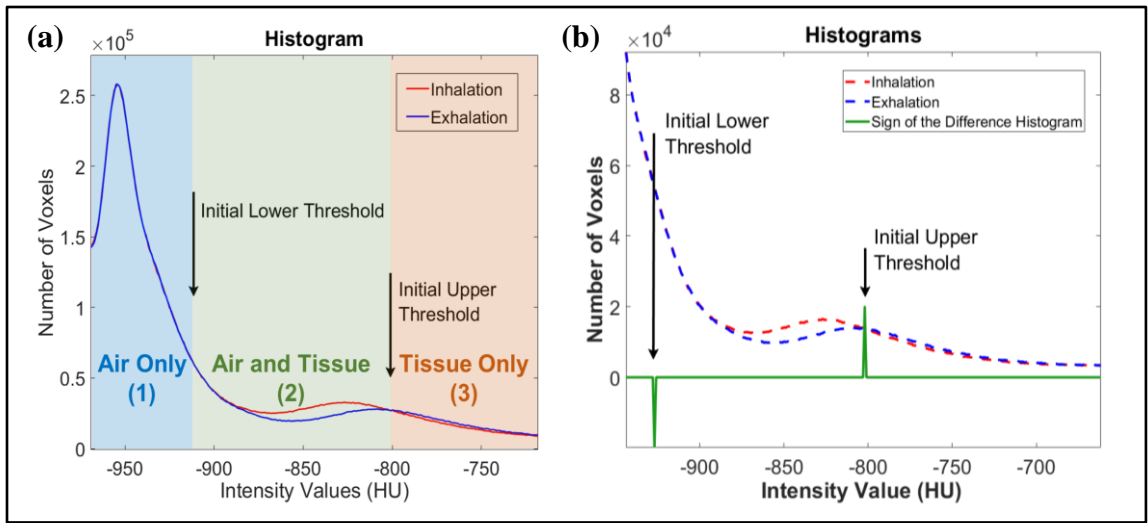


Figure 3-3. Finding initial thresholds for air segmentation. **(a)** The combined histogram of end-inhale and end-exhale histograms. The two initial thresholds divide the histogram to 3 regions, air only voxels, air combined with tissue voxels, and tissue only voxels. **(b)** The initial thresholds are found as points where the end-inhale and end-exhale histograms cross.

where I_{air} and I_{tis} are the average intensity of the voxels in class #1 and #3, respectively. Multiplying PVA with the voxel volume yields the air volume inside the voxel.

We generate the air distribution maps for the segmented lung image at the EI phase, and the deformed EE image after registration using the air segmentation algorithm (Figure 3-1). The high accuracy of the air segmentation algorithm has been demonstrated using both in-vivo and ex-vivo studies (48).

3.2.4 Correcting for Regional Volume Expansion

The air ventilation in the lungs is driven by two mechanisms, the regional volume expansion and the consequent increase in the amount of air. To obtain a physiologically relevant surrogate of ventilation using CT images, it is important to include the effect of both mechanisms. In the proposed CTVI algorithm, for the purpose of registration and to enable calculation of the change in the air volume, we reconstruct the deformed EE image with voxels corresponding to that of the EI image. Because the lung volume at the EI phase is larger, the deformed EE image is expanded to match that of the EI. Therefore,

to obtain a more accurate estimation of the air volume at the EE phase, the amount of air found from the deformed EE image at each voxel using the air segmentation algorithm must be corrected by the ratio by which the volume was regionally expanded to match the EI image. We obtain the regional expansion ratio from the change in the volume of the mesh elements after analysis. As described in Section 3.2.2.2, we can locate the voxels inside the FE mesh by inversely mapping physical coordinates to the iso-parametric space. When the corresponding mesh element is found for a voxel, the regional expansion at that voxel is defined by:

$$\alpha_{vox} = \frac{Vol_{E,def}}{Vol_{E,orig}}, \quad (3)$$

where the α_{vox} is the volume expansion ratio for the voxel vox , $Vol_{E,def}$ is the volume of the mesh element E after the FE analysis, and the $Vol_{E,orig}$ is the original volume of the mesh element E .

3.2.5 Generating the CTVI

Having the corrected air distribution map at the EE phase, and the corresponding air distribution map at the EI phase, we can obtain the CTVI from the difference in the air volume distribution. We also generated refined ventilation maps by lowpass filtering (Gaussian, $\sigma = 1$) and/or binning ($3 \times 3 \times 3$, full binning) the air distribution maps (both at EI and EE), to rectify the uncertainties caused by the small registration errors.

3.2.6 Comparison of the CTVI with Hyperpolarized Gas MRI

We used the ^1H and ^3He MR images available in the FLAIR dataset to compare our proposed CTVI with the MR ventilation. As described in Section 3.2.1, the breathing maneuver during image acquisition is different for treatment planning 4DCT and ^3He MRI. The MR images were acquired during breath-hold at FRC + 1L, while the 4DCT scans were acquired at free breathing condition. To reduce the impact of the differences in the breathing maneuver and hence facilitate the comparison between the CTVI generated at the EI phase of 4DCT and the MRI, we used the breath-hold 3DCT (performed at the same volume as the ^3He MR) to co-register the CTVI to MR images.

An off-the-shelf free-form deformable registration was used in Insight Toolkit (ITK; <https://itk.org>).

To compare the CTVI with the ^3He MRI quantitatively, we considered two categories of well-ventilated ($> 25^{\text{th}}$ percentile) and poorly ventilated ($0^{\text{th}} - 25^{\text{th}}$ percentile) (58). We calculated the Dice similarity coefficient between the co-registered ^3He MRI and CTVI for each of the poorly and well-ventilated regions.

3.3 « Results »

3.3.1 Biomechanical Model-based DIR Accuracy

The accuracy of the proposed biomechanical model for lung and tumor motion/deformation has been previously validated (see Section 2.3). The FE-based reconstruction algorithm was evaluated by comparing the absolute difference image between the segmented lung images at EE and EI before, and after registration. The deformed EE images were reconstructed using the FE-based method described in Section 3.2.2.2. Figure 3-4 illustrates the accuracy of the registration qualitatively, showing the EE image, EI image, reconstructed EE image, and difference images before and after registration for an arbitrary axial slice for one of the cases. We qualitatively compared the difference image after registration using our biomechanical model-based method and an off-the-shelf intensity-based DIR algorithm. Our biomechanical model-based DIR shows considerably higher performance.

The deformed EE image was also reconstructed using thin plate spline (TPS) to compare its performance with that of the FE-based reconstruction. Beside the superior performance of the FE-based reconstruction over TPS closer to the lung peripheries where the TPS extrapolation generated unrealistic and non-physical deformation fields, the results were almost identical elsewhere. This highlights the importance of using the mechanics-based methods if a more accurate and finer displacement field at the voxel-level from the FE mesh nodal displacements are desired. For quantitative assessment of the accuracy of the DIR method, LRE was calculated for each subject before and after registration using ~40 pairs of landmarks identified at bifurcation points (Table 3-1).

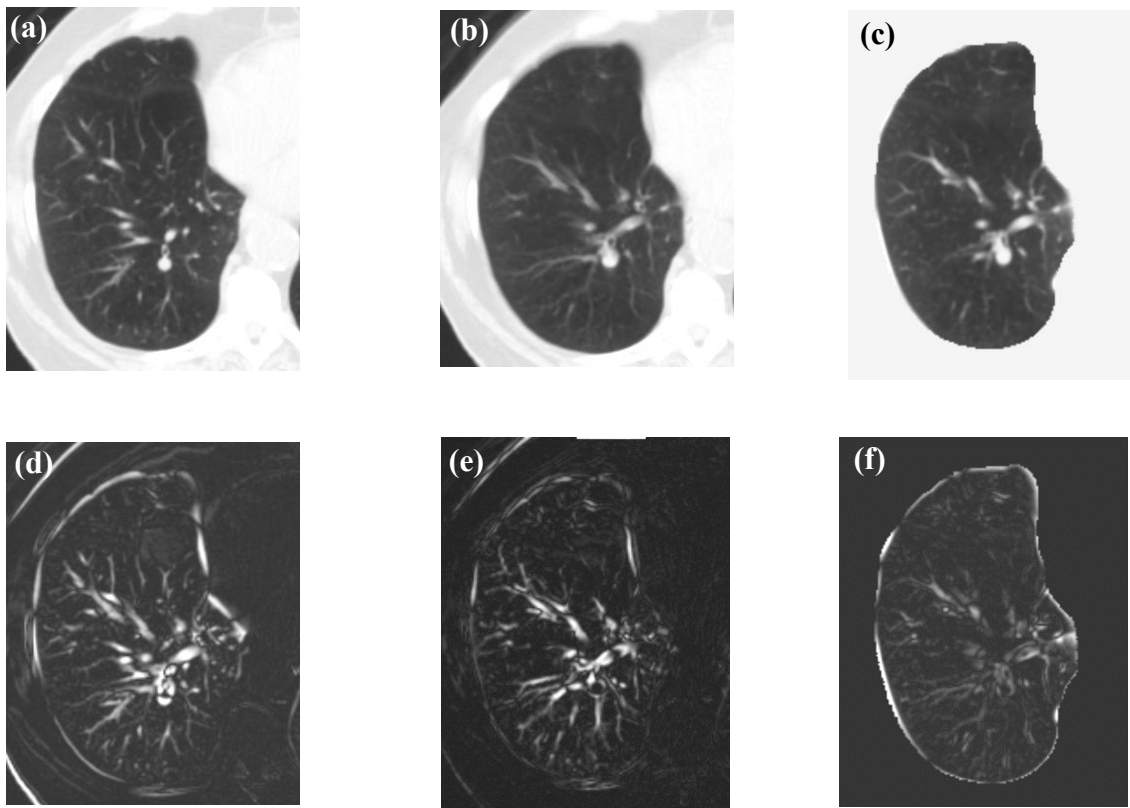


Figure 3-4. An example of the registration. **(a)** Moving image (EI), **(b)** target image (EE), **(c)** Resampled image (deformed EI image, to match EE), **(d)** difference image before registration, **(e)** difference image after registration using intensity-based DIR, and **(f)** the difference image after registration using biomechanical model-based DIR.

Table 3-1 Target registration error between EE and EI scans using ~40 landmarks, before and after FE-based registration.

Patient #	Before Registration (mm)	After Registration (mm)
1	8.30 ± 4.80	1.97 ± 0.58
2	7.01 ± 4.50	2.35 ± 0.75
3	8.81 ± 5.07	2.44 ± 1.05

3.3.2 CTVI and Qualitative Comparison with ^3He MRI

The proposed CTVI algorithm was used to generate ventilation images for the 3 subjects. Figure 3-5 shows the ^3He MRI overlaid on the proton MR (blue) and the corresponding CTVI overlaid on CT (heatmap). The coronal slices were chosen arbitrarily. As explained in Section 3.2.6, the MR scans are co-registered to the 4DCT and the figure shows the closest CTVI coronal slices to the MR slices after co-registration. The ^3He MR images show the distribution of inhaled ^3He gas in the lung and the CTVIs show distribution of air exchanged from EI to EE (i.e. ventilation). As shown in the Figure 3-5, the ^3He MRI agrees well with the corresponding CTVI slices for all cases, while some discrepancies exist between them. The extent to which the ^3He MR agrees with the CTVI appears to be

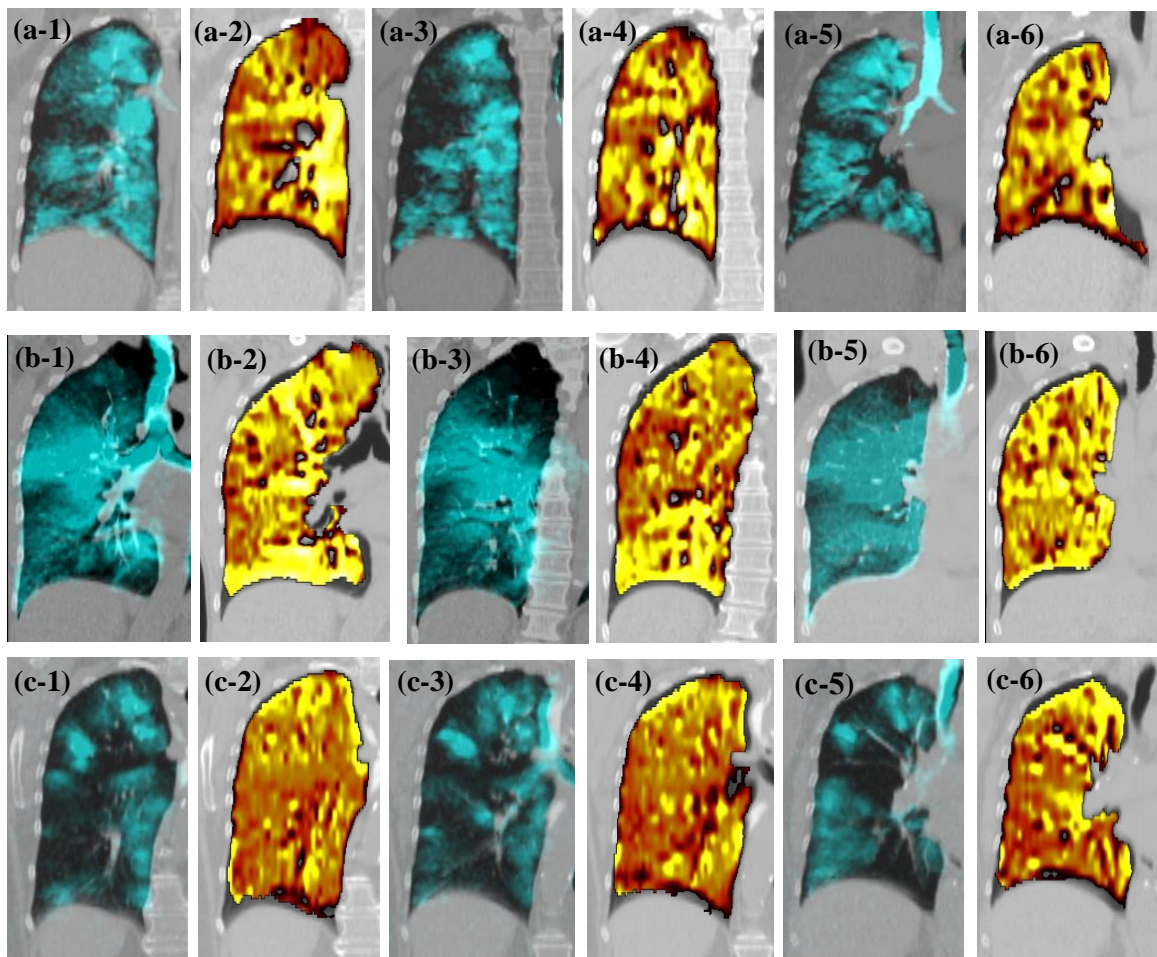


Figure 3-5. Comparison of the ^3He MR and CTVI, both overlaid on CT. Each row compares 3 coronal slices of one patient, (a) patient #1, (b) patient #2, and (c) patient #3.

different for each patient. For example, in patient #1 the agreement between the two modalities appear to be higher than that in patient #2. In addition, in all patients, the discrepancies mostly occurred in points closer to the inferior regions closer to the diaphragm, and in some cases at the top right. The disagreement between hyper polarized MR and CTVI in these lower regions has been shown to be attributed to differences in the breathing maneuver exercised when the images are acquired (58). The co-registration between the MR and 4DCT is conducted using an off-the-shelf intensity-based DIR, and therefore introduces some uncertainties to the ^3He MR-CTVI comparison. The MR-4DCT is responsible to reduce the impact of the difference in the breathing maneuver

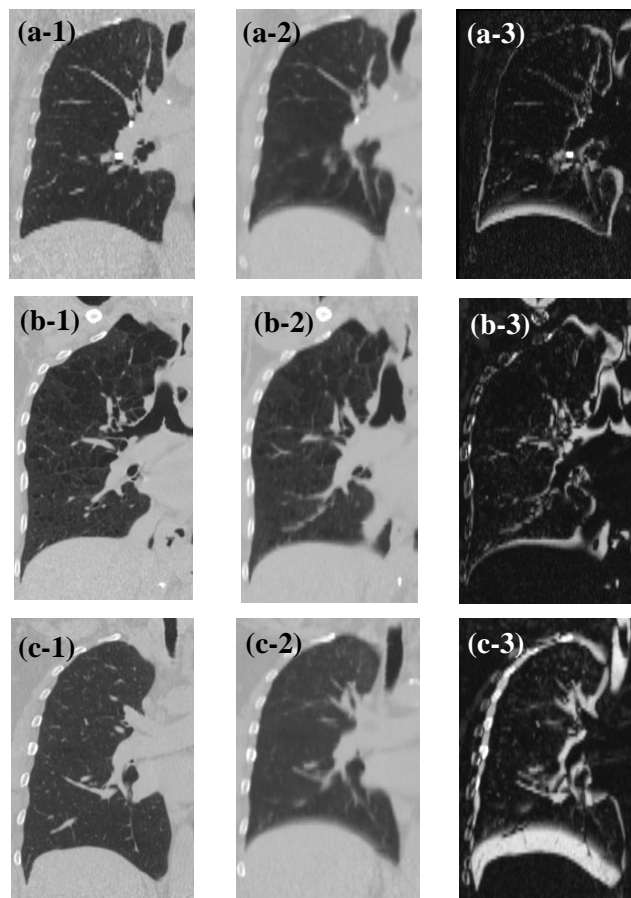


Figure 3-6. Comparing the breathing maneuver. Rows (a), (b), and (c) correspond to patients #1, #2, and #3, respectively. The first column shows a slice of the 3DCT, taken at the same inspiration volume as MR, second column shows the corresponding slice on 4DCT, acquired at tidal volume, and the third column is the absolute difference image of the two.

between the two modalities. Figure 3-6 shows the difference image between the 4DCT and the 3DCT (obtained at the same inspiration volume as MR). We can see some expansion at the top of the lung while the difference is the most predominant at and close to the diaphragm. Comparing the difference images of the patients, we can see that patient #3 shows the highest difference between the 4DCT inspiration volume and 3DCT (or MR) inspiration volume.

3.3.3 Quantitative Comparison with ^3He MRI

The Dice similarity coefficients between the ^3He MR and CTVI for each of the well- and poorly ventilated regions were calculated, as shown in Figure 3-7. Patient #1 shows the best agreement between the two modalities in both well-ventilated and poorly ventilated regions, while patient #3 shows the lowest agreement. The lower agreement for patient #3 compared to the other two cases can be attributed to the highest difference in the inspiration volumes of 4DCT and ^3He MR.

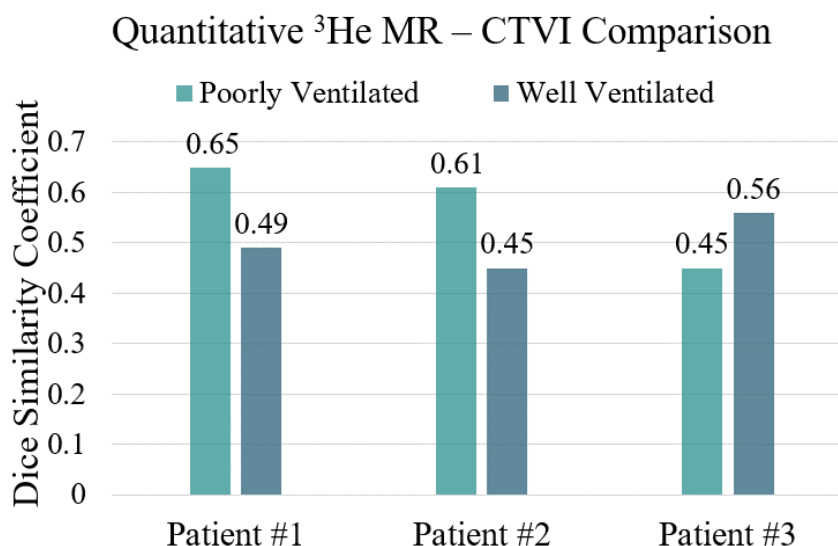


Figure 3-7. The Dice similarity coefficient between ^3He MR and CTVI for poorly ventilated and well-ventilated regions for the three patients.

3.3.4 Discussion and Conclusions

Lung ventilation imaging is of growing interest in the biomedical community for its potential to improve radiation therapy treatment planning, and hence the effectiveness

and safety of radiation therapy for lung cancer patients. Due to the widespread use of 4DCT for lung cancer therapy, incorporation of CTVI to radiation therapy treatment planning has become feasible. In this study, we proposed a novel CTVI technique that combines an accurate biomechanical model-based DIR with an advanced air segmentation algorithm. We validated the CTVI images generated using our proposed technique by comparing them with their hyperpolarized gas distribution map counterparts obtained using ^3He MR imaging, both qualitatively and quantitatively.

Firstly, we demonstrated good spatial agreement between the CTVI and ^3He MR by comparing the images qualitatively. We observed some disagreements between the two, which can be attributed to the difference in the breathing maneuver that has been shown to largely impact the generated CTVI (58). In addition, it is noteworthy that ^3He MR and CTVI are representatives of different surrogates of ventilation; ^3He MR shows the distribution of 1L of hyperpolarized gas in the lungs that is inhaled from functional residual capacity (and held for 15 seconds) while CTVI maps the change in the local volume of air during tidal breathing. Considering that the 4DCT images and the MR images were taken approximately a week apart, the discrepancies are not expected to be related to disease progression.

Unlike the CTVI algorithms that rely on intensity-based DIR, our algorithm was not sensitive to 4DCT image artifacts that happen near or on the diaphragm surface. This is because of the robustness of the biomechanical model-based DIR to the 4DCT artifacts, as explained in 2.3.2.

This study is a proof of concept, performed on a small number of patients. The results of the study are promising and suggest that a larger scale study is required to further validate the outcome of this study. Furthermore, comparison of our CTVI algorithm against other available CTVI methods is an important step for validation. Until recently, there has not been a common validation tool for different CTVI techniques. Kipritidis et al. (27) recently published the results of a multi-institutional study for validation of CTVI methods (VAMPIRE study) using different reference modalities that are clinically accepted for ventilation imaging. Various CTVI methods from seven research groups

were included in this study, most of which used intensity-based DIR for registration of peak-respiration CT scans. The ventilation metrics included DIR-Jac, DIR-HU, and two hybrid ones. The results of this study demonstrated that the extent of agreement (represented by measures of correlation or overlap) between different ventilation imaging modalities are not only dependent on the CTVI technique used, but also highly on the reference modality and the imaging subject (27). In this study, a biomechanics-based DIR that used the maximum principle stress as the ventilation metric showed highest correlation with nuclear medicine modalities (Galligas PET and DTPA-SPECT). The Dice similarity coefficients were reported as: median $Dice_{low} = 0.52$, range $Dice_{low} = 0.36-0.67$, for low ventilation regions, and median $Dice_{high} = 0.45$, range $Dice_{high} = 0.28-0.62$ (27). Although these values cannot be directly compared to the results of our study (different reference modality, different subjects and sample size, etc.), they demonstrate that the accuracy of our CTVI algorithm is similar to some of the best current CTVI algorithms and encourages future studies using our proposed CTVI technique. Finally, these findings highlight the promise of biomechanical models in DIR applications and their importance in advancing CTVI methods.

«References»

1. Ireland RH, Tahir BA, Wild JM, Lee CE, Hatton MQ. Functional Image-guided Radiotherapy Planning for Normal Lung Avoidance. Clin Oncol [Internet]. 2016 Nov [cited 2019 Jun 7];28(11):695–707. Available from: <https://linkinghub.elsevier.com/retrieve/pii/S0936655516302369>
2. Fain SB, Korosec FR, Holmes JH, O'halloran R, Sorkness RL, Grist TM. Functional Lung Imaging Using Hyperpolarized Gas MRI. J Magn Reson Imaging [Internet]. 2007 [cited 2019 Jun 6];25:910–23. Available from: www.interscience.wiley.com
3. Hoover DA, Capaldi DPI, Sheikh K, Palma DA, Rodrigues GB, Dar AR, et al. Functional lung avoidance for individualized radiotherapy (FLAIR): Study protocol for a randomized, double-blind clinical trial. BMC Cancer. 2014;
4. Marks LB, Spencer DP, Sherouse GW, Bentel G, Clough R, Vann K, et al. The

- role of three dimensional functional lung imaging in radiation treatment planning: The functional dose-volume histogram. *Int J Radiat Oncol* [Internet]. 1995 Aug [cited 2019 Jun 7];33(1):65–75. Available from: <https://linkinghub.elsevier.com/retrieve/pii/036030169500091C>
5. Yamamoto T, Kabus S, Bal M, Keall P, Benedict S, Daly M. The first patient treatment of computed tomography ventilation functional image-guided radiotherapy for lung cancer. *Radiother Oncol*. 2016;
 6. Yamamoto T, Kabus S, Von Berg J, Lorenz C, Keall PJ. Impact of four-dimensional computed tomography pulmonary ventilation imaging-based functional avoidance for lung cancer radiotherapy. *Int J Radiat Oncol Biol Phys*. 2011;
 7. Faught AM, Miyasaka Y, Kadoya N, Castillo R, Castillo E, Vinogradskiy Y, et al. Evaluating the Toxicity Reduction With Computed Tomographic Ventilation Functional Avoidance Radiation Therapy. *Int J Radiat Oncol Biol Phys*. 2017;
 8. Vinogradskiy Y, Castillo R, Castillo E, Tucker SL, Liao Z, Guerrero T, et al. Use of 4-dimensional computed tomography-based ventilation imaging to correlate lung dose and function with clinical outcomes. *Int J Radiat Oncol Biol Phys*. 2013;
 9. Huang Q, Jabbour SK, Xiao Z, Yue N, Wang X, Cao H, et al. Dosimetric feasibility of 4DCT-ventilation imaging guided proton therapy for locally advanced non-small-cell lung cancer. *Radiat Oncol* [Internet]. 2018 Dec 25 [cited 2019 Jun 7];13(1):78. Available from: <https://ro-journal.biomedcentral.com/articles/10.1186/s13014-018-1018-x>
 10. Bradley J, Graham M V., Winter K, Purdy JA, Komaki R, Roa WH, et al. Toxicity and outcome results of RTOG 9311: A phase I-II dose-escalation study using three-dimensional conformal radiotherapy in patients with inoperable non-small-cell lung carcinoma. *Int J Radiat Oncol Biol Phys*. 2005;
 11. Ding K, Bayouth JE, Buatti JM, Christensen GE, Reinhardt JM. 4DCT-based

measurement of changes in pulmonary function following a course of radiation therapy. *Med Phys* [Internet]. 2010 Feb 24 [cited 2019 Jun 7];37(3):1261–72. Available from: <http://doi.wiley.com/10.1118/1.3312210>

12. Fain S, Schiebler ML, McCormack DG, Parraga G. Imaging of lung function using hyperpolarized helium-3 magnetic resonance imaging: Review of current and emerging translational methods and applications. *Journal of Magnetic Resonance Imaging*. 2010.
13. Kaireit TF, Gutberlet M, Voskrebenezv A, Freise J, Welte T, Hohlfeld JM, et al. Comparison of quantitative regional ventilation-weighted fourier decomposition MRI with dynamic fluorinated gas washout MRI and lung function testing in COPD patients. *J Magn Reson Imaging* [Internet]. 2018 Jun 1 [cited 2019 Jun 7];47(6):1534–41. Available from: <http://doi.wiley.com/10.1002/jmri.25902>
14. Kirby M, Svenningsen S, Kanhere N, Owrangi A, Wheatley A, Coxson HO, et al. Pulmonary ventilation visualized using hyperpolarized helium-3 and xenon-129 magnetic resonance imaging: differences in COPD and relationship to emphysema. *J Appl Physiol*. 2013;
15. Harris RS, Schuster DP. Visualizing lung function with positron emission tomography. *J Appl Physiol*. 2007;
16. Petersson J, Sánchez-Crespo A, Larsson SA, Mure M. Physiological imaging of the lung: single-photon-emission computed tomography (SPECT). *J Appl Physiol*. 2007;
17. Van Beek EJR, Wild JM, Kauczor HU, Schreiber W, Mugler JP, De Lange EE. Functional MRI of the lung using hyperpolarized 3-helium gas. *Journal of Magnetic Resonance Imaging*. 2004.
18. Mugler JP, Altes TA. Hyperpolarized ¹²⁹Xe MRI of the human lung. *Journal of Magnetic Resonance Imaging*. 2013.
19. Ding K, Cao K, Fuld MK, Du K, Christensen GE, Hoffman EA, et al. Comparison

- of image registration based measures of regional lung ventilation from dynamic spiral CT with Xe-CT. 2012 Jul 27 [cited 2019 Jun 6];39(8). Available from: <http://dx.doi.org/10.1118/1.4736808>]
20. Simpson DR, Lawson JD, Nath SK, Rose BS, Mundt AJ, Mell LK. Utilization of Advanced Imaging Technologies for Target Delineation in Radiation Oncology. *J Am Coll Radiol*. 2009;
 21. Socinski MA, Morris DE, Halle JS, Moore DT, Hensing TA, Limentani SA, et al. Induction and concurrent chemotherapy with high-dose thoracic conformal radiation therapy in unresectable stage IIIA and IIIB non-small-cell lung cancer: A dose-escalation phase I trial. *J Clin Oncol*. 2004;
 22. Vinogradskiy Y, Castillo R, Castillo E, Chandler A, Martel M, Guerrero T. TU-A-BRC-11: Use of Weekly 4DCT-Based Ventilation Maps to Quantify Changes in Lung Function for Patients Undergoing Radiation Therapy. In: *Medical Physics*. 2011.
 23. Vinogradskiy Y, Faught A, Castillo R, Castillo E, Guerrero T, Miften M, et al. Using 4DCT-ventilation to characterize lung function changes for pediatric patients getting thoracic radiotherapy. *J Appl Clin Med Phys* [Internet]. 2018 Sep 1 [cited 2019 Jun 7];19(5):407–12. Available from: <http://doi.wiley.com/10.1002/acm2.12397>
 24. Patton TJ, Gerard SE, Shao W, Christensen GE, Reinhardt JM, Bayouth JE. Quantifying ventilation change due to radiation therapy using 4DCT Jacobian calculations. *Med Phys* [Internet]. 2018 Oct [cited 2019 Jun 7];45(10):4483–92. Available from: <https://doi.org/10.1002/mp.13105>]
 25. Yamamoto T, Kabus S, Bal M, Bzdusek K, Keall PJ, Wright C, et al. Changes in Regional Ventilation During Treatment and Dosimetric Advantages of CT Ventilation Image Guided Radiation Therapy for Locally Advanced Lung Cancer. *Int J Radiat Oncol Biol Phys*. 2018;

26. Kipritidis J, Hugo G, Weiss E, Williamson J, Keall PJ. Measuring interfraction and intrafraction lung function changes during radiation therapy using four-dimensional cone beam CT ventilation imaging. *Med Phys*. 2015;
27. Kipritidis J, Tahir BA, Cazoulat G, Hofman MS, Siva S, Callahan J, et al. The VAMPIRE challenge: A multi-institutional validation study of CT ventilation imaging. *Med Phys* [Internet]. 2019 Mar 1 [cited 2019 Jun 26];46(3):1198–217. Available from: <http://doi.wiley.com/10.1002/mp.13346>
28. Hegi-Johnson F, de Ruyscher D, Keall P, Hendriks L, Vinogradskiy Y, Yamamoto T, et al. Imaging of regional ventilation: Is CT ventilation imaging the answer? A systematic review of the validation data. *Radiother Oncol* [Internet]. 2019 Aug 1 [cited 2019 Jun 12];137:175–85. Available from: <https://www.sciencedirect.com/science/article/pii/S0167814019301148?via%3Dihub>
29. Yamamoto T, Kabus S, Klinder T, von Berg J, Lorenz C, Loo BW, et al. Four-dimensional computed tomography pulmonary ventilation images vary with deformable image registration algorithms and metrics. *Med Phys* [Internet]. 2011 Feb 16 [cited 2019 Jun 7];38(3):1348–58. Available from: <http://doi.wiley.com/10.1118/1.3547719>
30. Yamamoto T, Langner U, Loo BW, Shen J, Keall PJ. Retrospective Analysis of Artifacts in Four-Dimensional CT Images of 50 Abdominal and Thoracic Radiotherapy Patients. *Int J Radiat Oncol Biol Phys*. 2008;
31. Vandemeulebroucke J, Bernard O, Rit S, Kybic J, Clarysse P, Sarrut D. Automated segmentation of a motion mask to preserve sliding motion in deformable registration of thoracic CT. *Med Phys*. 2012;
32. Rietzel E, Chen GTY. Deformable registration of 4D computed tomography data. *Med Phys*. 2006;
33. Han L, Dong H, McClelland JR, Han L, Hawkes DJ, Barratt DC. A hybrid patient-

specific biomechanical model based image registration method for the motion estimation of lungs. *Med Image Anal* [Internet]. 2017 Jul 1 [cited 2019 Jun 18];39:87–100. Available from: <https://www.sciencedirect.com/science/article/pii/S1361841517300555>

34. Fuerst B, Mansi T, Carnis F, Sälzle M, Zhang J, Declerck J, et al. Patient-specific biomechanical model for the prediction of lung motion from 4-D CT images. *IEEE Trans Med Imaging*. 2015;
35. Han L, Dong H, McClelland JR, Han L, Hawkes DJ, Barratt DC. A hybrid patient-specific biomechanical model based image registration method for the motion estimation of lungs. *Med Image Anal*. 2017;
36. Werner R, Ehrhardt J, Schmidt R, Handels H. Patient-specific finite element modeling of respiratory lung motion using 4D CT image data. *Med Phys*. 2009;
37. Fuerst B, Mansi T, Zhang J, Khurd P, Declerck J, Boettger T, et al. A personalized biomechanical model for respiratory motion prediction. *Med Image Comput Comput Assist Interv*. 2012;
38. Al-Mayah A, Moseley J, Velec M, Brock KK. Sliding characteristic and material compressibility of human lung: Parametric study and verification. *Med Phys*. 2009;
39. Al-Mayah A, Moseley J, Velec M, Hunter S, Brock K. Deformable image registration of heterogeneous human lung incorporating the bronchial tree. *Med Phys*. 2010;
40. Al-Mayah A, Moseley J, Velec M, Brock K. Toward efficient biomechanical-based deformable image registration of lungs for image-guided radiotherapy. *Phys Med Biol*. 2011;
41. Al-Mayah A, Moseley J, Velec M, Brock K. Effect of friction and material compressibility on deformable modeling of human lung. In: *Lecture Notes in Computer Science (including subseries Lecture Notes in Artificial Intelligence and*

Lecture Notes in Bioinformatics). 2008.

42. Shirzadi Z, Sadeghi-Naini A, Samani A. Toward in vivo lung's tissue incompressibility characterization for tumor motion modeling in radiation therapy. *Med Phys*. 2013;40(5):051902.
43. Han L, Dong H, McClelland JR, Han L, Hawkes DJ, Barratt DC. A hybrid patient-specific biomechanical model based image registration method for the motion estimation of lungs. *Med Image Anal*. 2017;
44. Samavati N, Velec M, Brock K. A hybrid biomechanical intensity based deformable image registration of lung 4DCT. *Phys Med Biol*. 2015;
45. Simon BA. Non-invasive imaging of regional lung function using X-ray computed tomography. *Journal of Clinical Monitoring and Computing*. 2000.
46. Choi S, Hoffman EA, Wenzel SE, Castro M, Lin C-L. Improved CT-based estimate of pulmonary gas trapping accounting for scanner and lung-volume variations in a multicenter asthmatic study. *J Appl Physiol* [Internet]. 2014 Sep 15 [cited 2019 Jun 6];117(6):593–603. Available from: <http://www.ncbi.nlm.nih.gov/pubmed/25103972>
47. Castillo R, Castillo E, Martinez J, Guerrero T. TU-B-204B-04: Ventilation from Four Dimensional Computed Tomography: Density versus Jacobian Methods. In: *Medical Physics*. 2010.
48. Moghadas-Dastjerdi H, Ahmadzadeh M, Samani A. Towards computer based lung disease diagnosis using accurate lung air segmentation of CT images in exhalation and inhalation phases. *Expert Syst Appl*. 2017;
49. Naini AS, Lee TY, Patel R V., Samani A. Estimation of lung's air volume and its variations throughout respiratory CT image sequences. *IEEE Trans Biomed Eng*. 2011;
50. Reinhardt JM, Ding K, Cao K, Christensen GE, Hoffman EA, Bodas S V.

Registration-based estimates of local lung tissue expansion compared to xenon CT measures of specific ventilation. *Med Image Anal.* 2008;12(6):752–63.

51. Sadeghi Naini A, Patel R V., Samani A. Measurement of lung hyperelastic properties using inverse finite element approach. *IEEE Trans Biomed Eng.* 2011;
52. Zeng YJ, Yager D, Fung YC. Measurement of the Mechanical Properties of the Human Lung Tissue. *J Biomech Eng.* 1987;
53. Yeoh OH. Some Forms of the Strain Energy Function for Rubber. *Rubber Chem Technol.* 1993;
54. Kvasov BI. Cubic Spline Interpolation. In: *Methods of Shape-Preserving Spline Approximation.* 2010.
55. Thévenaz P, Blu T, Unser M. Interpolation revisited. *IEEE Trans Med Imaging.* 2000;
56. Bookstein FL. Principal Warps: Thin-Plate Splines and the Decomposition of Deformations. *IEEE Trans Pattern Anal Mach Intell.* 1989;
57. Schreibmann E, Pantalone P, Waller A, Fox T. A measure to evaluate deformable registration fields in clinical settings. *J Appl Clin Med Phys.* 2012;
58. Tahir BA, Marshall H, Hughes PJC, Brightling CE, Collier G, Ireland RH, et al. Comparison of CT ventilation imaging and hyperpolarised gas MRI: effects of breathing manoeuvre. *Phys Med Biol* [Internet]. 2019 Mar 7 [cited 2019 Jun 7];64(5):055013. Available from: <http://stacks.iop.org/0031-9155/64/i=5/a=055013?key=crossref.c8bdad7ad8bb5ff8426576808c53baf5>

Chapter 4

4 « Conclusion and Future Work »

In this thesis, we described the development of an accurate lung biomechanical model and its applications towards improving radiation therapy for lung cancer treatment. Two major applications of the model are tackled, including tumor motion/deformation compensation and CT based ventilation imaging. These applications were presented in Chapters 2 and 3 of this thesis. A summary and concluding remarks for each chapter are given below as closure.

4.1 Chapter 2

In Chapter 2, we described the development of a heterogeneous lung biomechanical model for motion and deformation estimation of the lung and the tumor. The accuracy of the proposed lung biomechanical model for tumor tracking was validated using measures of similarity and distance. In this study, we investigated the effect of incorporating the heterogeneities in the lung mechanics caused by COPD phenotypes on the tumor motion and deformation estimation accuracy. While the lung tissue homogeneity assumption for lung mechanics demonstrated fairly good performance for cases with less COPD severity, the heterogeneous tissue modeling alternative proved necessary to achieve high tumor motion/deformation estimation accuracies for cases that suffered from moderate to severe COPD. Another factor that influenced the accuracy gain achieved through utilizing the heterogeneous lung model is the proximity of pathological tissue to the tumor. The closer the pathological tissue to the tumor the higher the impact of utilizing the heterogeneous lung model. The results of the heterogeneous model for all cases showed promise of this biomechanical model for incorporation into radiation therapy applications, including but not limited to the biomechanics-based real time tumor tracking workflow designed by our group and explained in Section 1.3.5.

The impact of incorporating COPD-induced heterogeneity on tumor motion and deformation accuracy was shown to be dependent on the extent and distribution of COPD phenotypes. Considering the higher computation time and cost of developing a

heterogeneous model compared to a homogeneous one for a patient, this observation encourages a study that aims at predicting whether a patient is likely to benefit from a heterogeneous tissue model, or a homogeneous tissue model would provide sufficiently high accuracy, based on pertinent information from 4DCT.

We acknowledge a number of limitations of this study. The number of patients included in this study was small. A larger scale study has to be carried out to further validate the observations of this study and more importantly to enable statistical analysis on the results (e.g. whether or not the improvement resulting from incorporating the tissue heterogeneous mechanical properties are statistically significant). To incorporate this model into a biomechanics-based real time tracking system, the FE analysis needs to be accelerated. This can be achieved through parallel processing using GPU architecture or by employing reduced FE model strategies to speed up the computation model processing. The training of a predictive model that facilitates tumor tracking using the information from chest surface motion data requires representation of the loading and boundary conditions in a compact form as explained in (1).

4.2 Chapter 3

In Chapter 3, we described the application of the heterogeneous lung biomechanical model in combination with an advanced air segmentation algorithm in generating 4DCT-based ventilation maps. Since 4DCT has become part of the standard of care for lung cancer treatment in many centers, the proposed ventilation imaging algorithm has potential clinical applications for treatment planning. The potential higher resolution of CTVI compared to other ventilation imaging modalities can have clinical impacts for patients who are scheduled for intensity modulated radiation therapies and/or radiation therapy with ablative doses (SBRT) (2). The accuracy of the 4DCT ventilation maps were evaluated by comparison with ^3He MR scans taken from the same patients. Results of qualitative and quantitative comparison of the ^3He MR with our proposed CTVI technique are promising and warrant further investigation into improving its performance before carrying out a larger scale study.

We hereby acknowledge a number of the study limitations. Firstly, the small number of patients limits the statistical power of the study. A larger scale study that includes patients with different cancer stages, tumor locations/sizes, and comorbidity severities is required to further validate the findings of this study. In addition, SPECT is one of the reference modalities that is widely used for ventilation and it is important to compare our proposed CTVI and the acquired ^3He MR against the SPECT scans of the same patients (3–8). The choice of the CTVI algorithm has also been shown to impact the results of comparison with the reference modalities (9–12). Therefore, different CTVI algorithms should be used and compared against each other and the reference modalities (such as He MR or SPECT) to determine which CTVI method offers better physiological correspondence with SPECT or He MR scans.

Ventilation is only one surrogate for lung function. In functional avoidance planning applications, it is important to also consider other representations of lung function, including perfusion and diffusion (4,13–18). Ventilation to perfusion ratio in particular is an important representation of lung function that can be used to improve functional avoidance planning (13,19). Therefore, for functional avoidance therapies it is important to complement the information obtainable from ventilation imaging (e.g. from CTVI) with maps of distribution of perfusion and/or diffusion to have a more accurate and realistic assessment of lung regional function.

«References»

1. Karami E. A biomechanical approach for real-time tracking of lung tumors during External Beam Radiation Therapy (EBRT). Electron Thesis Diss Repos [Internet]. 2017;(August). Available from: <https://ir.lib.uwo.ca/etd/4816>
2. Mathew L, Wheatley A, Castillo R, Castillo E, Rodrigues G, Guerrero T, et al. Hyperpolarized ^3He Magnetic Resonance Imaging. Comparison with Four-dimensional X-ray Computed Tomography Imaging in Lung Cancer. *Acad Radiol*. 2012;
3. Christian JA, Partridge M, Nioutsikou E, Cook G, McNair HA, Cronin B, et al.

- The incorporation of SPECT functional lung imaging into inverse radiotherapy planning for non-small cell lung cancer. *Radiother Oncol*. 2005;
4. Lee HJ, Zeng J, Vesselle HJ, Patel SA, Rengan R, Bowen SR. Correlation of Functional Lung Heterogeneity and Dosimetry to Radiation Pneumonitis using Perfusion SPECT/CT and FDG PET/CT Imaging. *Int J Radiat Oncol* [Internet]. 2018 Nov 15 [cited 2019 Jun 12];102(4):1255–64. Available from: <https://www.sciencedirect.com/science/article/pii/S0360301618309039>
 5. Kida S, Bal M, Kabus S, Negahdar M, Shan X, Loo BW, et al. CT ventilation functional image-based IMRT treatment plans are comparable to SPECT ventilation functional image-based plans. *Radiother Oncol*. 2016;
 6. McGuire SM, Zhou S, Marks LB, Dewhurst M, Yin F-F, Das SK. A methodology for using SPECT to reduce intensity-modulated radiation therapy (IMRT) dose to functioning lung. *Int J Radiat Oncol* [Internet]. 2006 Dec [cited 2019 Jun 7];66(5):1543–52. Available from: <https://linkinghub.elsevier.com/retrieve/pii/S036030160602757X>
 7. Hegi-Johnson F, Keall P, Barber J, Bui C, Kipritidis J. Evaluating the accuracy of 4D-CT ventilation imaging: First comparison with Technegas SPECT ventilation. *Med Phys* [Internet]. 2017 [cited 2019 Jun 17];44(8). Available from: <https://doi.org/10.1002/mp.12317>
 8. Lavrenkov K, Christian JA, Partridge M, Niotsikou E, Cook G, Parker M, et al. A potential to reduce pulmonary toxicity: The use of perfusion SPECT with IMRT for functional lung avoidance in radiotherapy of non-small cell lung cancer. *Radiother Oncol*. 2007;83(2):156–62.
 9. Kipritidis J, Tahir BA, Cazoulat G, Hofman MS, Siva S, Callahan J, et al. The VAMPIRE challenge: A multi-institutional validation study of CT ventilation imaging. *Med Phys* [Internet]. 2019 Mar 1 [cited 2019 Jun 26];46(3):1198–217. Available from: <http://doi.wiley.com/10.1002/mp.13346>

10. Castillo R, Castillo E, Martinez J, Guerrero T. Ventilation from four-dimensional computed tomography: density versus Jacobian methods. *Phys Med Biol* [Internet]. 2010 Aug 21 [cited 2019 Jun 6];55(16):4661–85. Available from: <http://stacks.iop.org/0031-9155/55/i=16/a=004?key=crossref.a42cb07e582f5f419f90d3e92ff0b0c4>
11. Hegi-Johnson F, de Ruyscher D, Keall P, Hendriks L, Vinogradskiy Y, Yamamoto T, et al. Imaging of regional ventilation: Is CT ventilation imaging the answer? A systematic review of the validation data. *Radiother Oncol* [Internet]. 2019 Aug 1 [cited 2019 Jun 12];137:175–85. Available from: <https://www.sciencedirect.com/science/article/pii/S0167814019301148?via%3Dihub>
12. Yamamoto T, Kabus S, Klinder T, von Berg J, Lorenz C, Loo BW, et al. Four-dimensional computed tomography pulmonary ventilation images vary with deformable image registration algorithms and metrics. *Med Phys* [Internet]. 2011 Feb 16 [cited 2019 Jun 7];38(3):1348–58. Available from: <http://doi.wiley.com/10.1118/1.3547719>
13. Vinogradskiy Y, Koo PJ, Castillo R, Castillo E, Guerrero T, Gaspar LE, et al. Comparison of 4-Dimensional Computed Tomography Ventilation With Nuclear Medicine Ventilation-Perfusion Imaging: A Clinical Validation Study. *Int J Radiat Oncol* [Internet]. 2014 May 1 [cited 2019 Jun 7];89(1):199–205. Available from: <https://www.sciencedirect.com/science/article/pii/S0360301614000674?via%3Dihub>
14. Hoffman EA. Computed Tomography Studies of Lung Ventilation and Perfusion. *Proc Am Thorac Soc* [Internet]. 2005 Dec 1 [cited 2019 Jun 7];2(6):492–8. Available from: <http://pats.atsjournals.org/cgi/doi/10.1513/pats.200509-099DS>
15. Jobst BJ, Triphan SMF, Sedlacek O, Anjorin A, Kauczor HU, Biederer J, et al. Functional Lung MRI in Chronic Obstructive Pulmonary Disease: Comparison of T1 Mapping, Oxygen-Enhanced T1 Mapping and Dynamic Contrast Enhanced

- Perfusion. 2015 [cited 2019 Jun 6]; Available from: www.bmbf.de/en
16. Fain SB, Korosec FR, Holmes JH, O'halloran R, Sorkness RL, Grist TM. Functional Lung Imaging Using Hyperpolarized Gas MRI. *J Magn Reson Imaging* [Internet]. 2007 [cited 2019 Jun 6];25:910–23. Available from: www.interscience.
 17. Parraga G, Ouriadov A, Evans A, McKay S, Lam WW, Fenster A, et al. Hyperpolarized ^3He Ventilation Defects and Apparent Diffusion Coefficients in Chronic Obstructive Pulmonary Disease. *Invest Radiol* [Internet]. 2007 Jun [cited 2019 Jun 7];42(6):384–91. Available from: <https://insights.ovid.com/crossref?an=00004424-200706000-00008>
 18. Ouriadov A, Farag A, Kirby M, McCormack DG, Parraga G, Santyr GE. Pulmonary Hyperpolarized ^{129}Xe Morphometry for Mapping Xenon Gas Concentrations and Alveolar Oxygen Partial Pressure: Proof-of-Concept Demonstration in Healthy and COPD Subjects. *Magn Reson Med* [Internet]. 2015 [cited 2019 Jun 6];74:1726–32. Available from: <https://onlinelibrary.wiley.com/doi/pdf/10.1002/mrm.25550>
 19. Hoffman EA, Reinhardt JM, Sonka M, Simon BA, Guo J, Saba O, et al. Characterization of the interstitial lung diseases via density-based and texture-based analysis of computed tomography images of lung structure and function1. *Acad Radiol* [Internet]. 2003 Oct 1 [cited 2019 Jun 6];10(10):1104–18. Available from: <https://www.sciencedirect.com/science/article/pii/S1076633203003301>

Curriculum Vitae

Name: Parya Jafari

Post-secondary Education and Degrees: Sharif University of Technology
Tehran, Iran
2013-2017 B.Sc. (Electrical Engineering)

The University of Western Ontario
London, Ontario, Canada
2017-2019 M.Sc. (Biomedical Engineering)

Honors and Awards: Western Graduate Research Scholarship
Western University, London, ON, Canada
2017-2019

Fellowship of National Elite Foundation of Iran
Tehran, Iran
2013-2017

Exceptional Talents Scholarship of Iran
Tehran, Iran
2013-2017

Related Work Experience Teaching Assistant
The University of Western Ontario, London, ON, Canada
2017-2019

Undergraduate Research Assistant
Sharif University of Technology
2016-2017

Teaching Assistant
Sharif University of Technology, Tehran, Iran
2013-2017

Intern
Nikan Hospital, Tehran, Iran
Summer 2016

Publications:

Jafari, P., Hoover, D.A., Yaremko, B.P., Parraga, G., Samani, A., Sadeghi-Naini, A., (2019) “Incorporating Pathology-Induced Heterogeneities in a Patient-Specific Biomechanical Model of the Lung for Accurate Tumor Motion Estimation”. 2019 Annual International Conference of the IEEE Engineering in Medicine and Biology Society. IEEE, 2019 [Epub ahead of print].

Jafari, P., Yaremko, B.P., Parraga, G., Hoover, D.A., Sadeghi-Naini, A., Samani, A., (2019) “4DCT Ventilation Map Construction Using Biomechanics-based Image Registration and Enhanced Air Segmentation”. 2019 Annual International Conference of the IEEE Engineering in Medicine and Biology Society. IEEE, 2019 [Epub ahead of print].

Jafari, P., Geraili, A., Hassani, M.S., Araghi, B.H., Mohammadi, M.H., Ghafari, A.M., Tamrin, S.H., Modarres, H.P., Kolahchi, A.R., Ahadian, S. and Sanati-Nezhad, A., 2018. Controlling Differentiation of Stem Cells for Developing Personalized Organ-on-Chip Platforms. *Advanced healthcare materials*, 7(2).

Rezaei Kolahchi, A., et al., *Micromachines*. 7(9), 162, (2016).

Mohammadi, M. H., et al. *Advanced Healthcare Materials*. 5(19), 2459-2480, (2016)

Oral Presentations:

Jafari, P., Hoover, D.A., Yaremko, B.P., Parraga, G., Samani, A., Sadeghi-Naini, A., (2019) “Incorporating Pathology-Induced Heterogeneities in a Patient-Specific Biomechanical Model of the Lung for Accurate Tumor Motion Estimation”. In 41st Engineering in Medicine and Biology Conference, Berlin, Germany. July 2019.

Jafari, P., Yaremko, B.P., Parraga, G., Hoover, D.A., Sadeghi-Naini, A., Samani, A., (2019) “4DCT Ventilation Map Construction Using Biomechanics-based Image Registration and Enhanced Air Segmentation”. In 41st Engineering in Medicine and Biology Conference (EMBC), Berlin, Germany. July 2019.

Jafari, P., Hoover, D.A., Sadeghi-Naini, A., Samani, A., “Improved Tumor Motion Estimation by Incorporating Patho-physiology in Biomechanical Model of the Lung”. In 17th Annual Imaging Network Ontario Symposium (ImNO), London, ON. March 2019.

Poster Presentations:

Jafari, P., Hoover DA., Yaremko BP., Parraga G., Sadeghi-Naini A., Samani A., “Ventilation Image Calculation from 4DCT using Patient-Specific Biomechanical Model of the Lung”, In London Health Research Day (LHRD), London, ON. May 2019.

Jafari, P., Sadeghi-Naini A., Samani A., “Towards More Realistic Patient-Specific Lung Biomechanical Model for Lung Tumor Motion Compensation”, In 13th Annual London Imaging Discovery Day, London, ON. June 2018.